Characterization of the magnetic field of a 0.95 T permanent dipole magnet and measurement of proton beam deflection in this field within tissue-equivalent material

Master Thesis
for the acquisition of the academic degree
Master of Science (M. Sc.)

submitted by

Sebastian Thomas Gantz
born on August 16th 1990
in Dresden, Germany

Institut für Kern- und Teilchenphysik
Technische Universität Dresden
&
OncoRay - National Center for Radiation Research in Oncology
2017

submitted on March 16th 2017

Primary Reviewer:	Prof. Dr. Arno Straessner
Secondary Reviewer:	Prof. Dr. Wolfgang Enghardt
Supervisor:	Dr.-Ing. Aswin L. Hoffmann

Abstract

Purpose/Objective:

There is growing interest to explore the concept of MR-integrated proton therapy (MRiPT). However, no experimental proof-of-principle has been established so far. The aim of this work was to develop an 'in-magnet' measurement setup that facilitates to investigate the dosimetric feasibility and develop a commissioning procedure for future MRiPT devices to build a realistic proton pencil beam model in the presence of a magnetic field.

Material/Methods:

A C-shaped 0.95 T permanent neodymium ($Nd_2Fe_{14}B$) dipole magnet was used. Its magnetic field was characterized using Hall probe measurements. A procedure was established to perform routine quality assurance (QA) to guarantee for reproducibility of the magnetic field strength. Moreover, a 3D vector field representation for this magnet was calculated using finite-element modelling COMSOL-Multiphysics®.

For irradiation experiments, proton beams of 80 – 225 MeV were collimated using brass apertures having circular voids of either 5 or 10 mm diameter. The beam entered the magnet's air gap (40 mm) between its two horizontal poles perpendicularly to the main field component. Proton beam trajectories, 2D dose distributions and depth-dose curves in the presence of the magnetic field were measured with Gafchromic EBT3 film, being placed between two slabs of PMMA inside the air gap. Reference trajectories were measured without magnetic field. Additionally, in transmission experiments without phantom material, the deflection of the central beam spot perpendicular to the magnetic field 26 cm behind the magnet was measured with a scintillation detector (Lynx, IBA Dosimetry).

Results:

Magnetometry results validated the 3D magnetic flux density distribution as calculated by finite-element modelling. The simulation tended to underestimate the measured field strength in the plateau area by about 2 % (mean difference 20 mT). In repeated QA measurements, field strength changes remained below a threshold of 3 mT. For all proton energies, the lateral beam deflection due to the magnetic field increased with depth in the phantom. Lateral displacement of the Bragg peak position increased with initial energy, from 1.1 ($\pm$ 0.4) mm to 10.6 ($\pm$ 0.6) mm, for 80 and 180 MeV, respectively. In the transmission measurements, lateral deflection ranged from 56 ($\pm$ 0.5) to 30 ($\pm$ 0.5) mm for beam energies between 80 and 225 MeV and were in excellent agreement with theoretical predictions.

Conclusion:

A realistic 'in magnet' measurement setup for first MRiPT proof-of-principle experiments has been realized. Measurements of the magnetic field and proton beam trajectory proofed to be feasible and facilitate the development of commissioning and QA procedures for MRiPT. The data obtained is instrumental for building and validating beam models for MRiPT. Ongoing experiments focus on the impact of realistic treatment fields as well as the effect of inhomogeneous media on the dose distribution. As a next step, introducing an MR scanner into the proton beamline is planned.

Contents

Glossary

MRI	Magnetic resonance imaging
MRiPT	MR integrated proton therapy
QA	quality assurance
FEM	finite element modelling
BP	Bragg peak
netOD	net optical density
MC	Monte-Carlo
BEV	beams eye view
SNR	signal to noise ratio
PDD	percentage depth dose curve
ROI	region of interest
PMMA	Polymethylmethacrylate
MU	Monitor Units
UPTD	University Proton Therapy Dresden
CSDA	continuous slowing down approximation

List of Figures

List of Tables

1 Introduction

In 2014 about 15000 patients worldwide, suffering from a tumor disease, have been treated with particle therapy, the majority (86 %) of which were treated with protons [1]. The decisive edge of particle therapy over classical radiotherapy using photons is the depth-dose distribution [2]. While for photons, deposited dose falls exponentially with depth, for particle therapy, the dose maximum lies directly before the end-of-range, and is called the Bragg peak (see Figure 1.1). The particles range is hereby a function of initial energy.

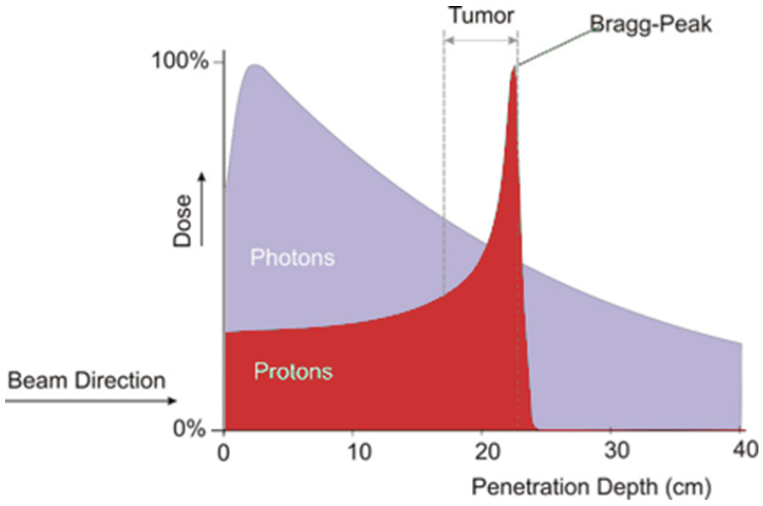

Figure 1.1: Relative depth dose distribution of protons and photons.

Proton therapy thus allows for a high dose conformity and organs-at-risk distally from the Bragg peak are spared from radiation. However, the sharp distal dose fall-off also makes proton therapy much more sensitive to both inter- and intra-fractional anatomical changes along the beam path, caused by e.g. positioning uncertainties, weight loss of the patient or tumor shrinkage during therapy, cavity filling, tissue swelling or organ movement. To account for these range uncertainties, margins of up to 15 mm have to be introduced, to avoid potential reductions in tumor control [3]. Reducing range uncertainties is therefore critical to exploit the full dosimetric benefits of proton therapy over classical radiotherapy and widen the therapeutic window for particle therapy. Next to *in-vivo* range verification methods currently developed [4, 5], image guidance is the concept with the highest potential to reduces margins in proton therapy [6].

Magnetic resonance imaging (MRI) offers unequalled soft-tissue contrast, fast real-time imaging, freedom from radiation dose and even the potential of motion tracking. It is therefore, that the integration of MRI and proton therapy (MRiPT) is believed to greatly enhance the treatment outcome in proton therapy in the future [7–10]. Until today, however, only in-silico studies for MRiPT have been performed. This work aims to present a first experimental step towards the development of an

MRiPT system. In the upcoming paragraphs, requirements for such a system will be investigated and the first step, performed here, will be presented.

Requirements for a hybrid MRiPT system The road towards a fully developed MRiPT system feasible of clinical application is long. A number of challenges present themselves for investigation. Firstly, protons being charged particles will be deflected by the strong magnetic fields of an MRI scanner. This deflection needs to be quantified and later accounted for in treatment planning. Secondly, MR imaging under the magnetic field influence of the proton beamline and beam itself has to be studied. Thirdly, treatment planning based on MR information still requires development. Fourthly, all kinds of interactions between the two systems such as radiation hardness of the MRI, image degradation during irradiation as well as dosimetry in the presence of the magnetic field and potential beam interactions with the MR radio-frequency have to be carefully investigated.

First step and outline of this work The aim of this work is to present a first experimental proof-of-concept for MRiPT, concentrating on the first of the above mentioned challenges: measuring proton beam deflection caused by a static magnetic field within tissue-equivalent material. Due to the lack of an existing MRiPT prototype, this was realised by using a permanent 1 T dipole magnet.
The following research hypotheses shall be investigated within this work. First, is the magnetic field of the used permanent magnet predicable by calculations and second, can those be verified by measurements? Third, is it possible to build an MRiPT-like prototype experimental setup capable of measuring and quantifying proton pencil beam deflections? To answer these hypotheses, this work is split into two parts, first characterizing the magnetic field of the dipole magnet (Part I) and second developing an experimental setup with which first irradiation experiments measuring proton beam deflections can be performed (Part II).

2 Theoretical Foundation

This chapter aims to provide a short overview to the physical principles underlying the topics covered within this thesis. Starting by introducing proton therapy as a concept in radiation oncology and turning to various methods used throughout this work, such as Hall-probe measurements, finite element modelling and film dosimetry.

2.1 Proton therapy

As an alternative to classical photon based radiation therapy, patient irradiation using protons was first proposed in 1946 by physicist Robert R. Wilson and first attempts at patient irradiation soon followed within the 1950s. The decisive advantage of proton therapy over conventional photon radiotherapy lies in the finite range of ion beams penetrating tissue and the Bragg peak phenomenon. Thereby a better sparing of healthy normal tissue from radiation can be achieved, thus reducing normal tissue complication while keeping the same tumor control as in photon therapy, or vice-versa.

2.1.1 Physical principles

Unless specified otherwise, this section orientates on the explanations given in [11].
Fast protons interact with matter through which they are traversing by three distinct processes: stopping, scattering and nuclear interactions. The first two processes occur by collisions with mainly atomic electrons and nuclei, respectively. They proceed via the electromagnetic interaction between the charge of the protons and the charge of atomic electrons or nuclei. Both these processes are well understood and comprehensive theories of stopping and scattering exist. In contrast, the third form of interaction, nuclear interactions, are more complex to describe. As they occur relatively rarely, describing them with simple approximations is sufficient within the field of radiation therapy.
Before taking a closer look at these processes, a number of basic quantities should be introduced.

Physical dose As the proton is slowed down, the energy $\mathrm{d}E$ absorbed per unit mass $\mathrm{d}m$ of the target material is defined as the physical absorbed dose D:

$$D = \frac{\mathrm{d}E}{\mathrm{d}m}. \tag{2.1}$$

The commonly used unit of dose is Gray (Gy), derived from the SI unit $[D] = 1\,\mathrm{J/kg} = 1\,\mathrm{Gy}$.

Fluence and stopping power Consider a proton beam traversing a medium, slowing down and eventually stopping. For each given depth x, the number of protons $\mathrm{d}N$ traversing an infinitesimal area element $\mathrm{d}A$ of a plane normal to the beam direction is defined by the fluence Φ:

$$\Phi \equiv \frac{\mathrm{d}N}{\mathrm{d}A}. \tag{2.2}$$

For an individual proton, the rate at which it loses kinetic energy is defined as the stopping power S:

$$S \equiv -\frac{\mathrm{d}E}{\mathrm{d}x}. \tag{2.3}$$

As S strongly depends on the stopping material, it is convenient to define the mass stopping power S_ρ as stopping power S corrected for the local density ρ of the stopping medium.

$$S_\rho \equiv \frac{S}{\rho} = -\frac{1}{\rho}\frac{\mathrm{d}E}{\mathrm{d}x}. \tag{2.4}$$

The thus defined stopping power consists mainly of an ionizing S_{col} and a radiative fraction S_{rad} and S_{nuc} [12]. The latter is neglected for the following considerations, as nuclear interactions contribute a very small fraction to the total stopping power. The radiative contribution is inversely proportional to the square of the mass of the proton. It is therefore orders of magnitude smaller as for electrons. Thus, protons loose their energy primarily through collision processes [12].
Suppose $\mathrm{d}N$ protons pass through an infinitesimal box of area $\mathrm{d}A$ and thickness $\mathrm{d}x$, the product of mass stopping power and fluence then writes as

$$\Phi\frac{S}{\rho} = \frac{(-\mathrm{d}E/\mathrm{d}x) \times \mathrm{d}x \times \mathrm{d}N}{\rho \times \mathrm{d}x \times \mathrm{d}A} = -\frac{\mathrm{d}N \times \mathrm{d}E}{\mathrm{d}m}. \tag{2.5}$$

Thus, the product describes the total energy loss of the proton beam per unit mass. This product, fluence times mass stopping power, is therefore closely related to the physical dose D. However, it is not necessarily the same. The energy lost by a proton beam exceeds the energy absorbed locally by a medium, as a fraction of the beam's energy is transferred to neutral secondaries (photons and neutrons) or high energetic secondary electrons (δ-rays).

Linear energy transfer - LET To consider the effect of local and non-local dose deposition described above, the property LET_Δ is defined as the ratio of the mean energy loss $\mathrm{d}E$ per path length $\mathrm{d}x$ [13]:

$$\mathrm{LET}_\Delta = \left(-\frac{\mathrm{d}E}{\mathrm{d}x}\right)_\Delta. \tag{2.6}$$

The LET is therefore the electronic collision stopping power, excluding all secondaries with a kinetic energy larger than the energy cut-off Δ. This implicates $\mathrm{LET}_\infty = S_{\mathrm{col}}$.
Having defined the main properties we now turn back to the three interaction processes stopping, scattering and nuclear interactions.

Stopping We already found that protons slow down in matter, mainly by myriad collisions with atomic electrons. The collision stopping power for protons can be described by the Bethe-Bloch equation [14]:

$$S_{\mathrm{col}} = -\left(\frac{\mathrm{d}E}{\mathrm{d}x}\right)_{\mathrm{col}} = \frac{e^4}{4\pi\epsilon_0^2 m_e c^2} \cdot n_e \cdot \frac{1}{\beta^2}\left[\ln\left(\frac{T_{\max}}{I}\right) - \beta^2\right], \tag{2.7}$$

where $\beta \equiv v/c$ of the proton, I is the mean excitation energy of the target material, $n_e = \frac{Z\rho}{Au}$ is the electron density of the target material and

$$T_{\max} = \frac{2m_e c^2 \beta^2}{1-\beta^2}$$

is the maximum kinetic energy transfer in a single collision with a free electron. Thus, n_e and I are the material-dependent parameters in equation (2.7).
The main depth-dependence in the Bethe-Bloch equation is the $\frac{1}{\beta^2}$ term, indicating that protons lose more energy in a collision the longer they interact with the electron. The rate of energy loss therefore increases as the protons slow down, giving rise to the Bragg peak near the end-of-range, see relative dose (blue) in Figure 2.1.

Scattering The interaction of a proton with the coulomb field of an atomic nucleus leads to the proton being deflected from its initial direction. The mean deflection in a single collision is very small. Scattering is described by Molière's multiple coulomb scattering (MCS) theory which predicts the spatial distribution to be nearly Gaussian and the scattering angle to depend mainly on the target materials atomic number Z.

Nuclear Interactions A primary proton may scatter both elastically and non-elastically off a material nucleus. Elastic scattering has been described above. Infrequently, protons will also interact non-elastically with a nucleus and knock out one or more constituents. These secondaries tend to have much lower energies and larger angles then the primary proton [11]. Therefore the effect of nuclear interactions is merely a reduction in primary proton fluence, which may occur at any proton energy and therefore depth and is the primary source of fluence loss before the end-of-range. This can be seen in Figure 2.1 where, for a 150 MeV proton beam, about 20 % of initial protons are absorbed by nuclear interactions.

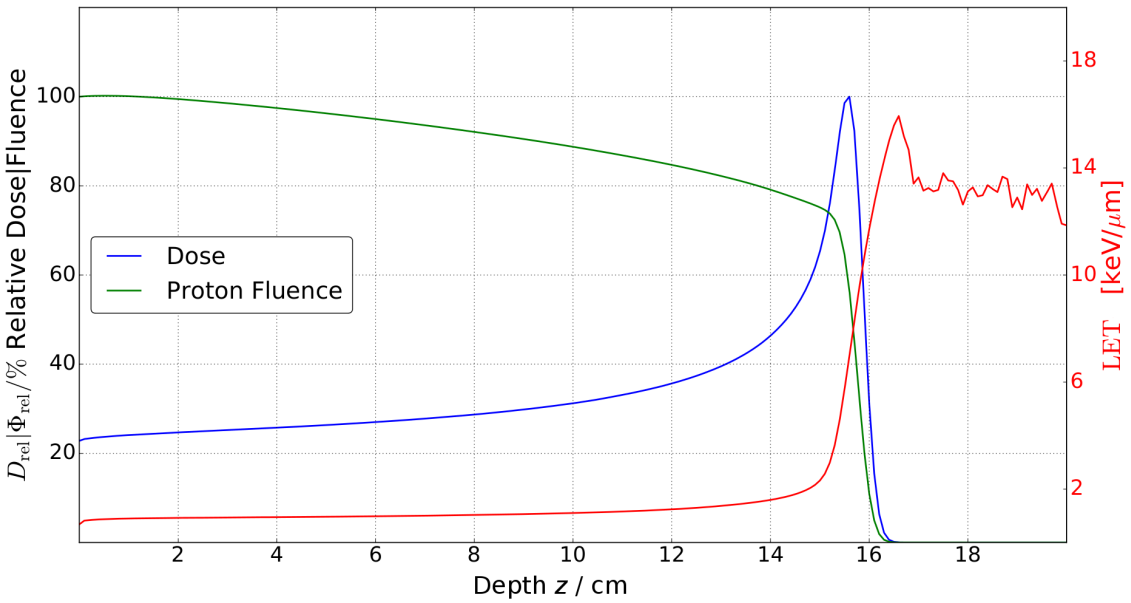

Figure 2.1: Relative fluence, relative dose and LET as a function of penetration depth for a 150 MeV proton beam. Reprinted from [15].

The Bragg peak, range and range-energy relation The combination of the three interactions (stopping, scattering and nuclear interactions) determines the shape of the typical depth-dose curve, featuring the Bragg peak at the end-of-range (see Figure 2.1). The range R_0, also called mean

projected range of a proton beam, is defined by the depth at which half of the initial protons have stopped, i.e. at which the fluence drops to 50 %.
However, in measurements this quantity is often hard to obtain, as mainly dose is measured. Therefore the range R_0 is correspondingly defined as

$$R_0 = R_{80} \tag{2.8}$$

where R_{80} is the depth at the distal 80 % point of the peak.
For a proton beam stopping in a homogeneous material the range R_0 is determined by the protons initial energy E_0. It is therefore convenient to define a range-energy relation by fitting a power law to experimental data:

$$R_0 = \alpha E_0^p \tag{2.9}$$

where both α and p are fit parameters depending on the target material [16]. To compare the range in different materials to water, the water-equivalent ratio (WER) can be defined as [17]

$$\mathrm{WER}_{\mathrm{mat}} = \frac{R_{80,\mathrm{water}}}{R_{80,\mathrm{mat}}}. \tag{2.10}$$

Note, that WER in general is a function of initial proton energy. However, for materials which can be fitted with the range-energy relation to the same p value like water, WER becomes energy-independent. As an example, measured WER values for Polymethylmethacrylate (PMMA) over the range of 100 MeV to 225 MeV remain constant at 1.158 [18].

2.2 Important aspects of MR image scanners

As mentioned in chapter 1.2, the first step towards MRiPT is to investigate the proton beam deflection caused by the magnetic field of an MR scanner. Within this thesis, no MR imaging was performed. Therefore, this section aims to provide the absolute physical basics of magnetic resonance imaging only, focussing on the involved magnetic fields, which are necessary for the imaging modality to work.
In a clinical MRI scanner, three electromagnetic fields are involved in the imaging process. First, a static magnetic field B_0 with a typical field strength of 0.2 T to 3 T, which aligns nuclear spins with the field, due to the Zeeman-effect. Most applications of MR imaging focus on proton spins, which have the spin quantum number $I = 1/2$. In a static magnetic field, their magnetic moment splits into two energetically different states, parallel and anti-parallel orientation with the field. The energy separation ΔE reads as follows

$$\Delta E = \hbar\omega_0 = \gamma\hbar B_0 \tag{2.11}$$

where $\hbar$ is the reduced Planck's constant, $\gamma/2\pi = 42.6\,\frac{\mathrm{MHz}}{\mathrm{T}}$ is the gyromagnetic ratio for proton spins and ω_0 is the Larmor frequency. To change state between the two energy levels, the proton spin has to either absorb or emit a photon with the exact Larmor frequency. Thus, the second electromagnetic field in an MR scanner is a radiofrequency (RF) signal, inducing such transitions.
The MR image signal is the response to these RF pulses. However, a third field is needed to enable spatial encoding. Gradient fields are thus applied to locally change the Larmor frequency and thereby only excite protons at a defined position. Typical field gradients are in the range of 30 - 45 mT/m [19].
For the purpose of investigating proton beam deflection, the static B_0 field of an MR scanner is of main importance.

2.3 Measurement and application methods

This section provides an overview of the principles of the different measurement methods used throughout this work. Finite element modelling will be introduced as a computational method to acquire magnetic field information. Magnetometry methods, in particular Hall probe measurements, which will be used in part I and two different dosimetry tools, radiochromic films and scintillation detectors, used throughout part II, are described in the following.

2.3.1 Finite element modelling

Finite element modelling (FEM) is a numerical approach to solving differential equations. Finding an analytical solution to a set of partial differential equations (PDE) is in many cases difficult or impossible. Therefore, the numerical approach subdivides the whole problem into smaller parts, so called finite elements. The solution requires three steps. First, an accurate representation of the complete geometry of the problem has to be defined. Second, material properties, influencing the PDE's to be solved have to be defined for each part of the geometry together with material and global boundary conditions. Third, the geometry is divided into a number of finite elements, such that the PDE can be locally solved between those element points by approximative basis functions.
This is done by reformulating the initial problem in a so called weak formulation, by convolution of the PDE with a weight function, often called test function. The function to be determined by the PDE is then defined as a sum over basis functions which are non zero only over one element node and all its neighbours. Within this element the basis functions are approximated as linear or polynomial [20].
This weak formulation of the PDE can thereby be transferred into a matrix representation, i.e. a system of equations, which is solved by variation of the weight functions. A variety of solvers is available for this purpose.
Taking the concept of FEM to a permanent magnet assembly, the necessary equations are given in the following. First the magnetic flux density $\vec{B}$ can be expressed as

$$\vec{B} = \vec{B}_r + \mu_0 \mu_r(H) \vec{H} \tag{2.12}$$

where $\mu_0 = 4\pi \times 10^{-7} \frac{\mathrm{H}}{\mathrm{m}}$ is the magnetic constant, $\mu_r(H)$ the relative permeability and $\vec{H}$ the magnetic field intensity. Furthermore, the magnetic vector potential $\vec{A}$ is defined by

$$\vec{B} = \vec{\nabla} \times \vec{A}. \tag{2.13}$$

With this choice of definition, Gauss's law for magnetism is already covered, as $\mathrm{div}(\vec{B}) = \mathrm{div}(\mathrm{rot}\vec{A}) = 0$. Taking the curl over equation (2.12) and using (2.13) we find in analogy to [21]

$$\vec{\nabla} \times \frac{1}{\mu_r \mu_0} \left(\vec{\nabla} \times \vec{A} \right) - \frac{1}{\mu_r \mu_0} \vec{\nabla} \times \vec{B}_r = \vec{\nabla} \times \vec{H} = 0 \tag{2.14}$$

where $\vec{\nabla} \times \vec{H} = 0$ is Ampere's law for a current free situation. Thus, equation (2.14) defines the PDE to be solved, $\vec{A}$ is the unknown, and $\vec{B}_r$ and μ_r are input parameters. Further, material boundary conditions are defined such that the difference of the potential $\vec{A}$ at the boundary is $\vec{A}_1 - \vec{A}_2 = 0$ [22]. Global boundary conditions should be defined as $\vec{n} \times \vec{A} = 0$ for a simulation box large enough such that the flux density is expected to be negligible small at the rims of the box.

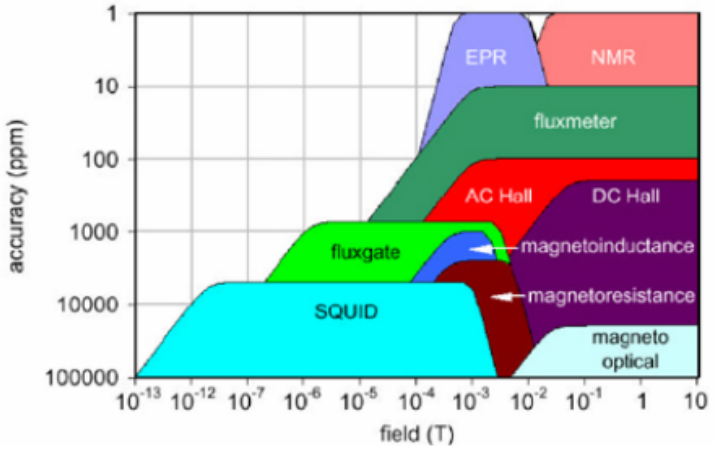

Figure 2.2: Panoply of magnetic measurement technologies, ordered by their respective measurement range and accuracy. Reprinted from [24].

The potential solution for $\vec{A}$ is then defined in terms of the interpolatory functions of the defined mesh used and the nodal values of potential. Thus,

$$\vec{A} = \sum_{k=i}^{m} \lambda_k \vec{A}_k \tag{2.15}$$

where λ_k are the weight functions and $\vec{A}_k$ is the potential at the k-th node.
The actual solution of the PDE is dependent on the used solver, the curl(curl) operator equation (2.14) is defined as a matrix D, resulting in a matrix equation $D \cdot A' = 0$ where A' is a vector of A_k [21, 23].

2.3.2 Magnetometry - Choice of measurement method

A panoply of methods exist for the acquisition of magnetic field information, see Figure 2.2. The different available techniques should be investigated focussing on their applicability for magnetic field mapping of a permanent magnet. Required measurement range and accuracy can give a hint towards the most suitable technique to be used. As the permanent magnet used within this work has a maximum flux density of approximately 1 T, three techniques will be briefly introduced, focussing on their respective benefits and drawbacks for field mapping: Hall probes, fluxmeters and nuclear magnetic resonance (NMR).

Fluxmeter A fluxmeter is a direct application of Faraday's law of induction. The sensor is a coil, in which a voltage is induced if it is moved within a magnetic field. The integral over the voltage is then a measure of the flux change. Fluxmeters thus measure flux and their mapping is a slice sampling of the field over the coils inner area rather then a point sampling. Thus, for dedicated inhomogeneous flux density mapping, a very small coil would be needed. Further, thermal expansion of the coil and voltage drift require dedicated compensation. Noise in both coil movement and voltage reading is critical due to the integration procedure.

Nuclear magnetic resonance Nuclear magnetic resonance is the gold standard for magnetic field measurement [24]. The measurement principle is the energy separation of the two fundamental states

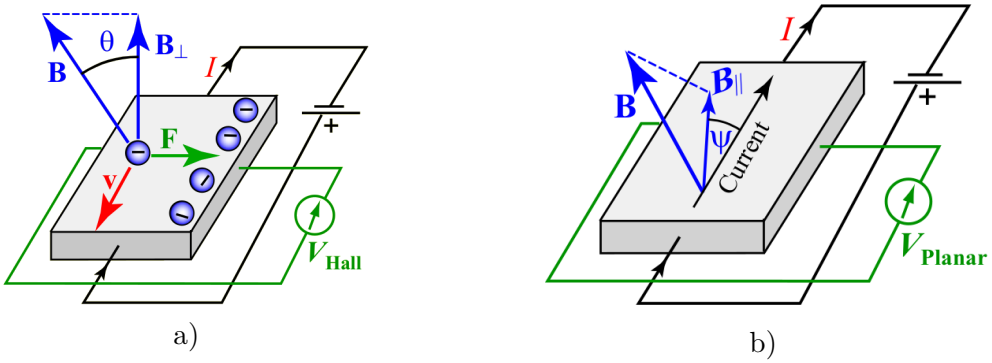

Figure 2.3: Physical principle of the Hall effect (a) and the Planar Hall effect (b). Reprinted from [25].

of the proton spin in an external magnetic field, see section 2.2, which linearly depends on the magnetic field strength (equation (2.11)). NMR Teslameters thus measure the norm of the magnetic field, are extremely accurate (up to 1 ppm accuracy) and do not suffer from drift or temperature dependence. However, there are substantial limitations for NMR. Field measurement are only possible in very uniform fields, as in inhomogeneous fields, a distribution of Larmor frequencies would be measured. Thus no gradient fields can be mapped. NMR can only be applied for DC or slow AC fields and measuring low fields requires the use of larger samples, as the resonance diminishes with lower energy separation.

Hall probe The physical principle of Hall probe measurements will be explained in detail in section 2.3.3. Hall probe devices are easy to build and use. They are compact, exhibit low noise and are highly reproducible. Field components are measured separately, as the device is only sensitive to magnetic fields normal to the probe' plane. The sensitivity of a device is variable over a large range of field strength, thus being well suited for inhomogeneous field mapping. However, a number of limitations need to be kept in mind. Hall probe devices suffer from non-zero offset due to probe material imperfections, temperature sensitivity, angular dependence of field reading and the planar Hall effect.

In conclusion, NMR is ineligible for inhomogeneous field mapping, and fluxmeters do not offer point-to-point mapping capability, as well as being limited to a few mT typically [25]. In contrast, the use of a Hall probe for field mapping of the complete field distribution of a permanent magnet of 1 T field is justified by its well-suited properties: precise spatial measurements performable in 3D, almost linear field response and operation range over multiple orders of magnitude, while still offering acceptable accuracy. Limitation effects have to be considered in planning and setup.

2.3.3 The Hall effect

Hall probe devices use the Hall effect, which is the result of the Lorentz force $\vec{F}$ on charge (q) carriers moving with velocity ($\vec{v}$) in the presence of a magnetic field ($\vec{B}$)

$$\vec{F} = q\vec{v} \times \vec{B}. \tag{2.16}$$

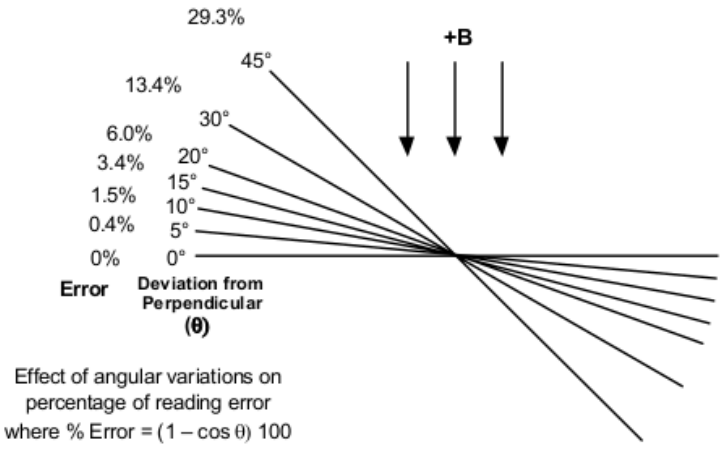

Figure 2.4: Angular dependency of Hall probe magnetic field measurement. Figure reprinted from [26].

The force results is an accumulation of charge carriers, leading to a steady state voltage V_{Hall} perpendicular to the current I and magnetic field (see Figure 2.3a), i.e. in the direction of $\vec{F}$. The resulting voltage difference is linearly proportional to the applied current I and the field component $B_\perp$ normal to the probes plane

$$V_{\text{Hall}} \propto I \cdot B_\perp. \tag{2.17}$$

The measured voltage V_{Hall} is transferred into field reading using a linear calibration curve $B(V_{\text{Hall}})$. As the actual curve is not completely linear over multiple orders of magnitude, linear calibrations are always valid for a specified field range only. Furthermore, the calibration curve's slope is a weak function of temperature, requiring measurements to be performed at constant temperature, close to the temperature used for calibration.

As mentioned in the previous section, the Hall effect voltage also suffers from a low non-zero offset, due to material imperfections, which is one reason for the need of a zero-point calibration. Another reason is the earth's magnetic field, which in some low field-applications could lead to perturbations.

Two further limitations which should be considered here, are the angular dependency of the field measurement using a Hall probe and the planar Hall effect. The Hall voltage is dependent on the field component perpendicular to the probe's plane, thus a single field component is measured. This enables a separate measurement of the vector components of $\vec{B}$, while careful orientation and matching to the intrinsic coordinate system of the field is important. Figure 2.4 illustrates the field reading error caused by misalignment of the probe relative to a desired orientation.

For the field mapping of 3D fields, the planar Hall effect has to be taken into account (see Figure 2.3b). It produces a voltage signal V_{planar} if the field has a component $B_\parallel$ in the plane defined by the current flow and voltage contacts

$$V_{\text{planar}} \propto I \cdot B_\parallel^2 \cdot \sin(2\Psi) \tag{2.18}$$

where Ψ is the angle between the current I and the in-plane component $B_\parallel$. The planar Hall effect can be minimized by a suitable choice of geometry, such that $\sin(2\Psi) = 0$ [25]. This can be accomplished by choosing one axis of the measurement coordinate system to coincide with the main field component of the magnetic field and the other two such that the expected minor field components are also parallel to the remaining two coordinate axes.

2.4 Proton beam dosimetry

2.4.1 Radiochromic film dosimetry

Radiochromic films have first been investigated in 1984 by David Lewis searching for a processless film capable of producing high resolution images of electron beams [27]. Diacethylenes were found to undergo a solid-state polymerization triggered by incidient radiation. Over the years different radiochromic films have been produced, with the majority using the effect of film self-darkening upon incident radiation. The most recent development in the field was introdcuded in 2012. EBT3 films are the successor of the former EBT2 films, both produced by Ashland Inc. (Covington, Kentucky, USA). The EBT3 film consist of a 28 µm thin active layer of LiPCDA (lithium salt of pentacosa-10,12-diynoic acid) which is mounted between two 120 µm thick layers of a transparent polyester substrate. LiPDCA monomers are arranged in ordered microcrystals, which are dispersed in the active layer. Upon incident radiation a polymerization process is triggered forming a linear long-chained polymer (polyPCDA). Its concentration increases with dose. The polymer's backbone absorbs visible light, thus leading to the film getting increasingly darker with higher polymer concentration and thus absorbed dose [28]. The film darkening is a two-step process with a first fast polymerization phase and a slow post-irradiation darkening, which is the reason why film evaluation should not be done any earlier then 24 h after irradiation [29].
The increase in optical density (OD) is therefore a measure of the dose and can be determined by scanning the film using a color flatbed scanner. Depending on the dose range, either the red or green color channel offers the highest dose sensitivity. The red color channel should be used for dose ranges between 0.1 and 10 Gy, while the green channel gives best results between 10 and 40 Gy [30]. While scanning, care has to be taken to the film's orientation due to the hair-like structure and preferential alignment of the polymers along the short edge of the films, leading to a scanner-orientation dependency. The manufacturer recommends scanning of all films in landscape orientation. From the scanned images, red pixel intensity values I_i can be converted to net optical density (netOD) by

$$\mathrm{netOD}_i = \log_{10} \frac{I_0}{I_i} \tag{2.19}$$

where I_0 is the intensity of an unexposed film. Using netOD for dose calibration has the benefit of accounting for potential film darkening over time, as only the increase in density is used, rather then the absolute value.
Using a calibration, netOD is further translated into dose, by fitting a three parameter (k_1, k_2 and k_3) polynomial equation onto calibration data:

$$D_i = k_1(\mathrm{netOD}_i) + k_2(\mathrm{netOD}_i)^{k_3}. \tag{2.20}$$

Investigations have shown an energy-independence of proton calibration for energies above 20 MeV [31], which allows for using a single calibration curve for different proton beam energies. However, for lower energies, as the LET increases at the end of range, a so called film-quenching effect is known to underestimate dose on the film as a function of LET. In depth-dose measurements using films, this effect is visible in the vicinity of the Bragg peak, where dose is underestimated compared to ionization chamber measurements or simulations [29].
However, quantifying this effect as function of LET is difficult, as the acquisition of LET distributions in experimental settings is often impossible. Thus, the effect is widely described empirical as a

function of dose showing underestimation in the vicinity of the Bragg peak for residual energies below 10 MeV. Underestimations reported in the Bragg peak vary from experiment to experiment, but are in the range of 10 % to 25% [32, 33](EBT films) [34, 35](EBT2 films) relative to ionization chambers and up to 50 % [29, 31](EBT3 films) to simulations. However, range uncertainties due to this effect are reported to be below 0.5 mm [32] thus indicating that EBT3 films are nevertheless suitable for depth-dose measurements.

2.4.2 Lynx detector

The Lynx detector (IBA Dosimetry GmbH, Schwarzenbruck, Germany) is a high resolution gadolinium-based scintillating detector, which is optimized for quality assurance measurements in clinical radiotherapy use, especially for the pencil beam scanning technique. The detector allows for real-time relative dosimetry on a 2D surface, featuring an active area of 30×30 cm^2, with an effective resolution of 0.5 mm [36]. Upon traversing the scintillating screen protons lose energy via ionization. This energy is converted into visible light, reflected by a mirror and collected by a CCD camera. The use of a mirror allows to place the CCD camera outside of the proton beam, sparing it from radiation which would decrease its lifetime.

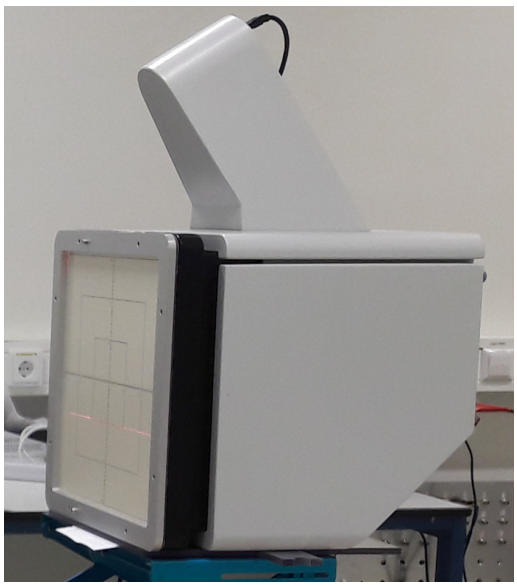

Figure 2.5: Picture of the Lynx detector.

Part I

Magnetometry of a C-shaped 0.95 T permanent dipole magnet

This part of the thesis provides a characterization of the magnetic field of the permanent magnet, shown in Fig. 2.6, which will later be used for in-magnet irradiation experiments. Precise information about the 3D magnetic flux density is required as input parameter for Monte-Carlo (MC) based particle transport simulations, aiming to study the effect of the magnetic field on the dose distribution of a proton beam. To enable a full simulation of the proton beam transport, all field components of both the main and the fringe fields of the magnet have to be assessed. FEM calculations, as described in chapter 3.2, can yield such a complete description of the field information, but have to be validated against measurements. Therefore, the characterization of the magnetic field is done in a two step process: first, simulation results are acquired using the FEM software COMSOL Multiphysics (COMSOL AB, Stockholm Sweden). Second, the three magnetic field components are measured on a 3D grid using a Hall probe based automated magnetometry setup dedicated for this purpose.

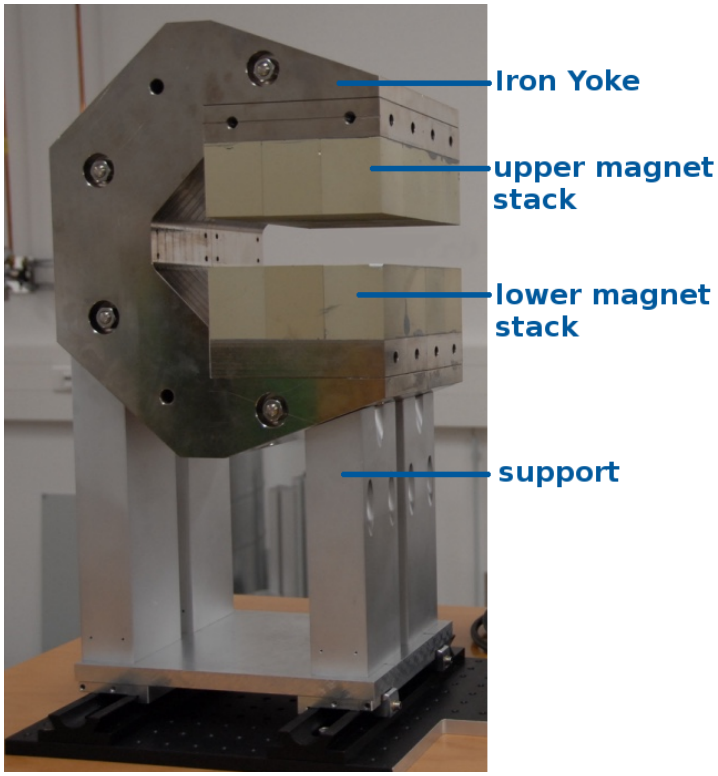

Figure 2.6: Permanent $Nd_2Fe_{14}B$ magnet used throughout this work.

3 Material and Methods

3.1 Geometry of the magnet assembly

The magnet is build in a classical C-shaped dipole setup consisting of two magnet stacks. Each stack consists of 12 blocks of Neodymium-Iron-Boron ($Nd_2Fe_{14}B$) material, namely VACODYM 764 TP, coated with a 10 µm thin layer of anticorrosive VACCOAT 10047 (VACUUMSCHMELZE GmbH & Co. KG, Hanau). Each of the blocks measures $50 \times 50 \times 59$ mm^3, being stacked in a 3×4 array, resulting in a 150×200 mm^2 magnet area. The vertical gap between the two stacks, in the following called the magnet's air gap, measures 39.5 ± 0.1 mm. The magnet stacks are glued to the C-shaped iron yoke. For precise measures of the yoke, see Figure 3.1.

Throughout this chapter, an Cartesian coordinate system will be used with the origin being at the

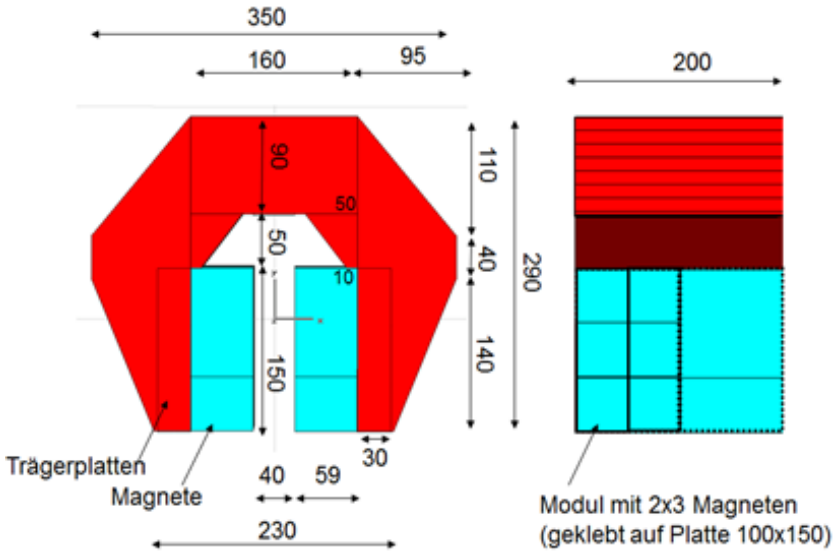

Figure 3.1: Sketch of the magnet assembly dimensions. All scales are in mm.

magnet's isocenter, i.e. the center of the air gap between the magnet stacks. The axes are chosen such that the z-axis points along the direction of the magnetic field lines. x is chosen parallel to the longer edge of the magnet and y parallel to the short edge, see Figure 3.5. The system (x,y,z) forms a right-handed coordinate system which is parallel to the motor axis directions, depicted in Figure 3.5.

3.2 Finite element modelling of the magnetic field

To characterize the magnetic field of the magnet assembly, finite element modelling (FEM) calculations are used as a standard computation tool especially for applications requiring field data at each point in space such as particle transport simulations. The first step to obtain the magnetic field information from FEM calculations is the implementation of the magnet's geometrical dimensions. As the magnet has been used for different studies before, this 3D-CAD (computed-aided design)-like implementation

has already been performed in the software COMSOL Multiphysics [37] as presented in Figure 3.2. This implementation was further optimized as follows. For the computation of the magnetic field, material properties for the yoke and magnet blocks had to be defined. Here, two properties are essential: first, the remanent field strength $B_r = 1.37\,\mathrm{T}$ of the VACODYM 764 TP material, which is described by the manufacturer [38, p.14], and second, the hysteresis curve $B(H)$ for the iron yoke, which was taken from the COMSOL material library using the predefined material 'Soft Iron (without losses)'. The magnet assembly is centrally placed in a simulation box of $0.6 \times 0.6 \times 0.6$ m^3, that is assigned with the material property 'Air'. Note that, as $B = \mu H$, only one parameter from the material properties of 'Air' is essential for the magnetic flux density calculation: the relative magnetic permeability, which was set to $\mu/\mu_0 = 1.0$, where $\mu_0 = 4\pi \times 10^{-7}$ H/m [39].

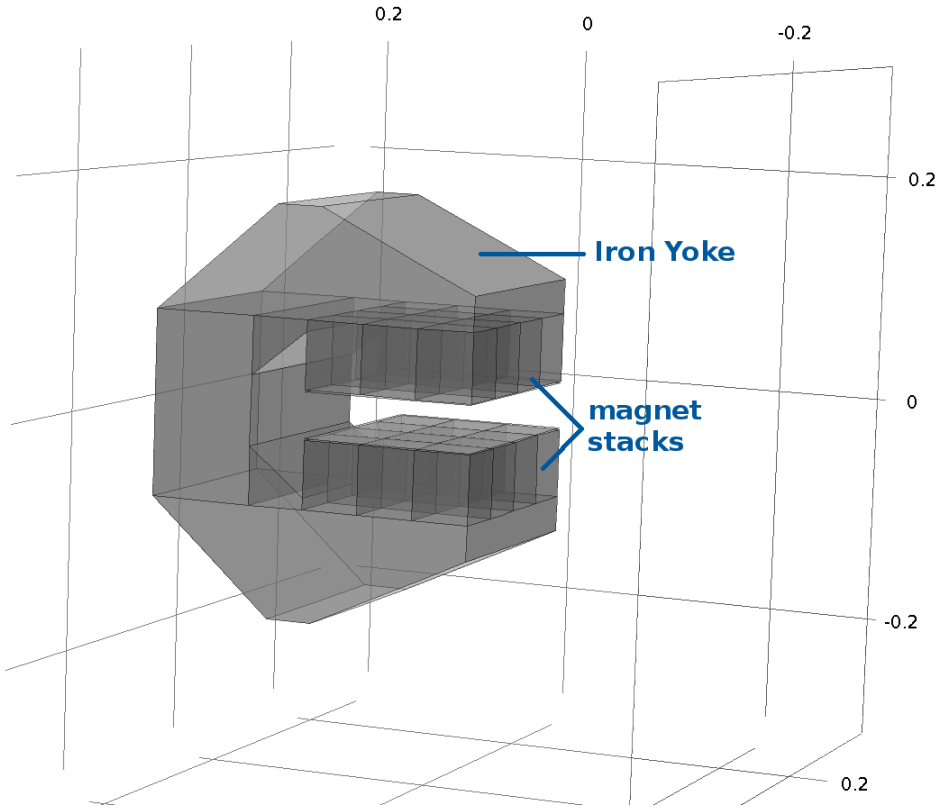

Figure 3.2: 3D model of the geometry of the magnet within COMSOL Multiphysics. Scales in m.

For the numerical calculation of the magnetic flux density distribution, a 3D spatial grid was defined starting from a free tetrahedral structure with the smallest predefined meshsize available ('extreme fine') within the magnet blocks, yoke and the air gap between the magnets, and the second finest meshsize ('extra fine') for the remaining area, i.e. the air surrounding the magnet. Starting from these predefined meshes, maximum and minimum element size have been further reduced in both meshing options, to assure precise representation of the field, focussing on the areas of expected high field and/or gradient. A non-symmetric linear stationary FGMRES (Flexible Generalized Minimal Residual method)[23, 40] solver is used to calculate the magnetic vector potential, from which the magnetic flux density is gained (see chapter 2.3.1). The solver requires more computational resources then a classical GMRES solver but has shown faster convergence for electromagnetic studies [41]. All parameters for the meshing and solver are given in Table 3.1.

meshsize	magnet and air gap	environment
Maximum element size / m	0.01	0.02
Minimum element size / m	1.0×10^{-4}	1.0×10^{-4}
Maximum element growth rate	1.3	1.35
Curvature factor	0.2	0.3
Resolution of narrow regions	1	0.85
FGMRES solver	degrees of freedom	4,924,302
	calculation time / s	3474

Table 3.1: COMSOL parameters used for meshing and solver configuration.

3.3 Development of an automated magnetometry system

This section describes the process of the development leading to the automated magnetometry setup which has been used to measure the magnetic field of the magnet. The designed setup is mobile and can be set up on a relatively small area. However due to the weight of the magnet of over 100kg, a crane is needed for transportation or rotation of the magnet. Furthermore, the measurement room has to be equipped with a climate control due to temperature dependence of the magnetometry device, as will be described in the following subsection. After initial development and testing, the whole setup was first built up at the HZDR, ELBE lab and later moved to the UPTD facility, in preparation for the irradiation measurements, which will be the focus in part II of this thesis.

3.3.1 Choice of magnetometer - transverse Hall probe

The choice of Hall probe measurements was done following a set of requirements for the specific task. Firstly, the system had to be able to measure all three field components of the magnetic flux distribution separately on a 3 dimensional spatial grid with a point-to-point distance in the range of a few mm. Secondly, the narrow (about 4 cm) air gap of the magnet limits both the size and shape of the probe. A further crucial point is the measurements range and sensitivity of the probe. Thus, upper and lower boundaries for the absolute field strength to be measurable are given by the magnet blocks remanent field strength of 1.37 T and the 0.5 mT = 5 G magnetic safety margin, often referred to as the 5 Gauss limit for DC fields. Thirdly, the accuracy of field measurements are demanded to be better then 1% of the reading.
Considering all of these specifications, a transverse Hall-probe with an rigid 4 inch brass-stem was chosen, see Figure 3.4. Previous experiments have shown that using a rigid stem probe rather than a flexible one significantly reduces probe vibrations during field scanning [42]. The MMTB-6J04-VG Hall probe (Lake Shore Cryotronics, Westerville, USA) is used together with a Model 421 Lake Shore Gaussmeter to convert the induced Hall voltage into field reading.
There are three measurement ranges (HST - 2, see Figure 3.4) defined for the Gaussmeter in combination with the used probe, having their respective maxima at 3 T, 0.3 T and 0.03 T with a resolution of 1/3000 of the range maximum, that means 1 mT, 0.1 mT and 0.01 mT, respectively.
As specified in Figure 3.4 Hall probe readings are temperature dependent, which requires all mea-

surements to be done at constant room temperature close to the calibration temperature of 25.0 °, see Figure 3.4. To assure this, all performed field scans were carried out under climate control while temperature was monitored at $T = 23.0 \pm 0.5\,°$. Using a Zero Gauss Chamber, zero point calibration of the probe was done before each set of measurements. The manufacturer guarantees an absolute calibration of the Hall probe for each of the measurement ranges to an accuracy better $\pm 0.5\,\%$ of field reading [26].

As absolute spatial measurements were required, the precise position of the probes active area needed

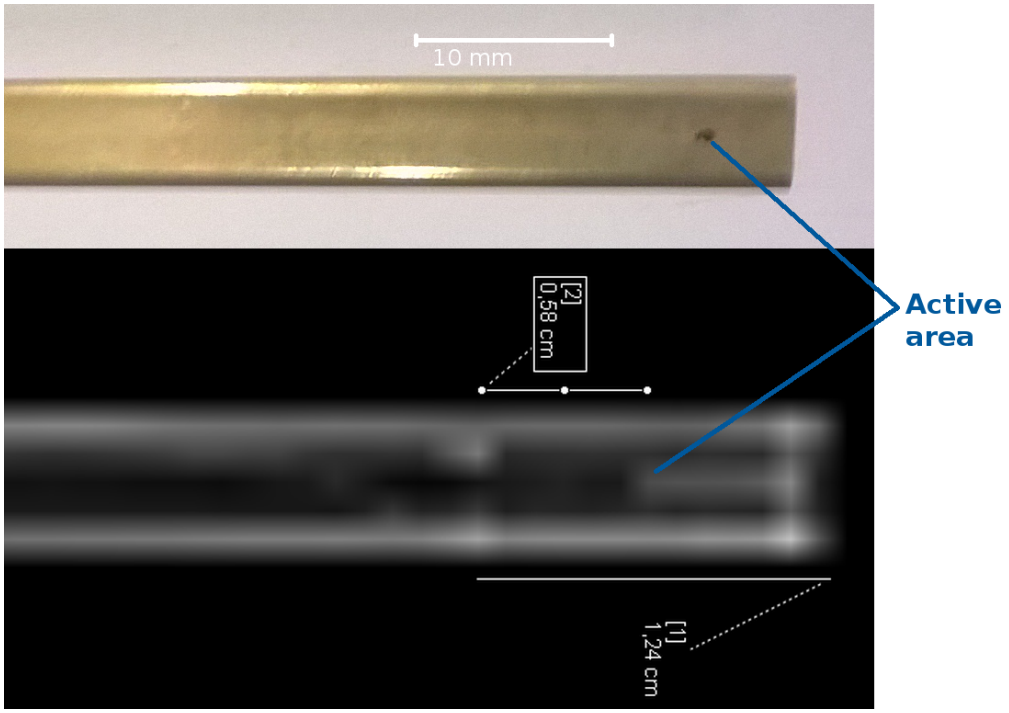

Figure 3.3: The centre of the Hall probes active area was marked as a black dot on the brass coating (top) after performing an X-ray scan (bottom). Pictures are not to scale.

to be determined more accurately than given by the manufacturer (see Figure 3.4). Therefore an X-ray image (120 kVp) of the Hall probe was aquired and the active area's centre was marked accordingly (see Figure 3.3).

The Gaussmeter was connected to a laptop via a self-build RS-232 serial connector following the description in the Gaussmeter manual [26], thereby adapting to the needed communication to fully control the Gaussmeter by a LabVIEW based program, as reported in chapter 3.3.3.

3.3.2 Linear positioners & Motor control unit

To be able to scan the magnetic flux density distribution of the whole magnet, a 3D automated positioner was built for the Hall probe using a set of precision linear stages (OWIS, Staufen im Breisgau, Germany). Different sizes were used for each dimension, choosing an optimum between maximum possible scan area and minimum weight on the stages, in order to avoid sagging due to a high torque. Figure 3.5 depicts the measurement setup, showing the three linear stages.

A LTM 120-400-HSM positioner was used for the x direction, which is the long edge of the magnet, with an operational length of 395 mm enabling line scans over the whole length of the magnet (200 mm) and extending into the fringe field. In the same manner, a stage type LTM 80-300 HSM (operational length 195 mm) was chosen for the y direction. For the z direction, the smallest available motor stage

Brass Stem Transverse Probes (Long Stem)

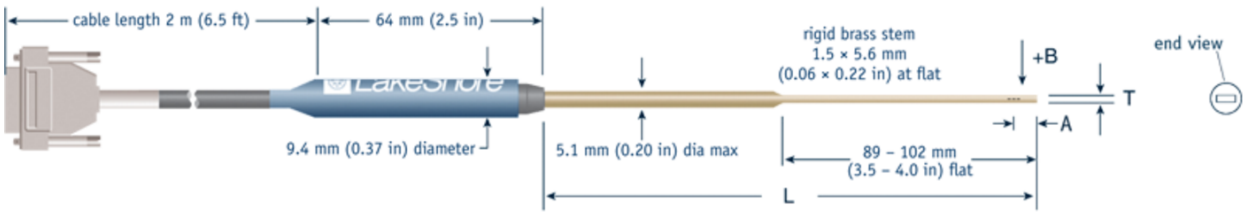

	L mm (in)	T mm (in)	Width mm (in)	A mm (in)	Active area mm (in)	Stem material	Frequency range	Usable full scale ranges	Corrected accuracy (% rdg at 25 °C)	Operating temp range	Temp coefficient (max) zero	Temp coefficient (max) of sensitivity	Contains temp sensor
for Models 460, 450, and 421													
MMTB-6J04-VG	101.6 ±3.2 (4 ±0.125)	1.78 (0.070) max	5.58 (0.22)	3.81 ±1.27 (0.150 ±0.050)	Approx 1.02 dia (0.040 dia)	Brass	DC	**HST-2** 300 G, 3 kG, 30 kG	±0.15% to 30 kG	0 °C to +75 °C	±0.13 G/°C	-0.005%/°C	No

Figure 3.4: Transverse Hall probe sketch (top) and specifications (bottom) provided by Lake Shore. Figure reprinted from [43].

(LTM 60-75 HSM, operational length 70 mm) was chosen as the magnet's air gap only measures 40 mm in vertical direction. The positioning error of all motors is specified by the manufacturer to be smaller than 25 µm per 100 mm travel [44].
The motors were mounted on top of each other in the named order and set onto two 24 cm mounts positioned on top of an optical plate, which is large enough to support both the magnet and the robotic system. This assures axes alignment of the measurement system with the magnet's system. A manually rotatable probe holder has been used for precise angle adjustment of the probe, to minimize any angular uncertainties and resulting field component bias (as described in section 4.2.2).

The OWIS linear stages feature a step motor [44] that is controlled by the universal modularly designed position control unit PS 90 [45]. The motor control unit was connected to a laptop via USB connection, enabling the system to be controlled by a LabVIEW based program using NI-VISA (National Instruments, Virtual Instrument Software Architecture, Austin, USA) as the programming interface between the control unit and the LabVIEW development environment.

3.3.3 LabVIEW measurement routine

Combining automated operation of the Hall-probe measurement and the motor movement, an existing LabVIEW program developed by O. Zarini, (HZDR, Laser Particle Acceleration Division) for quadrupole magnetic field scanning was adapted for this experiment.
In a first step, the program controls the Lake Shore Gaussmeter, using the VISA I/O Interface Software, thus being able to read out data from the Gaussmeter and send commands (such as changing measurement range) at the same time. Adjusting the measurement range is done automatically depending on the field reading. Furthermore, the tool stores field reading and used range into a text file at any point defined by the scan procedure routine.
The main LabVIEW routine controls the three linear motors and moves them on a rectangular grid with user-defined pitches and end points. The user defines the x_0, y_0 and z_0 range in a symmetrical

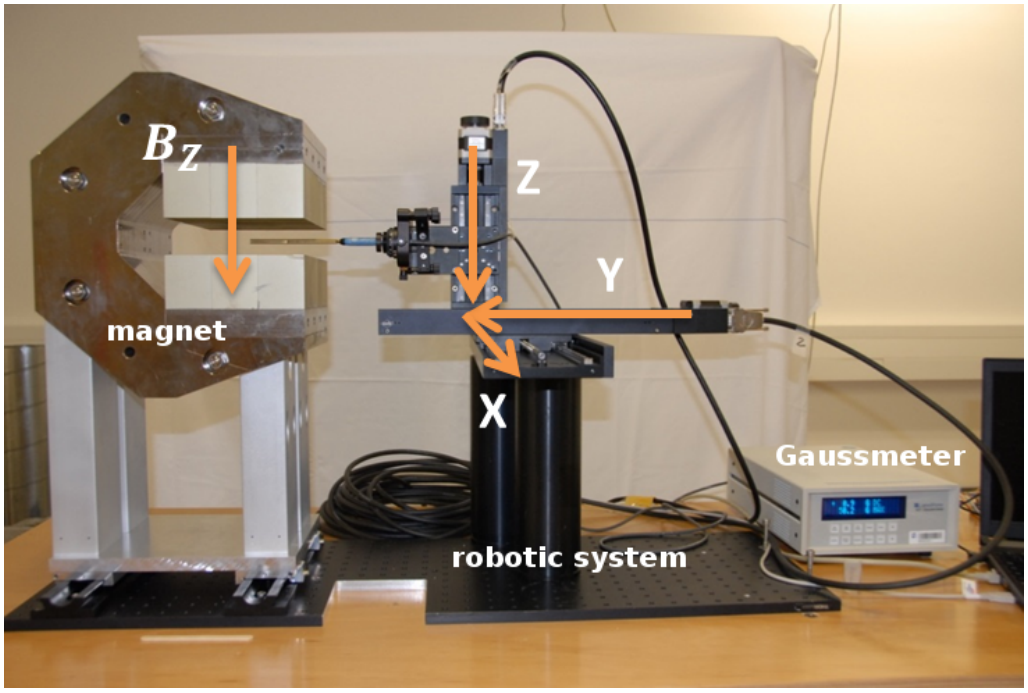

Figure 3.5: Magnetometry setup with coordinate system (x,y,z) and main magnetic field component B_z.

way around a centre point, and specifies the pitches $\Delta x, \Delta y, \Delta z$. The direction of motion is then given by forming a meander in the x-y plane, starting at $(x_0, y_0, -z_0)$, where x is the slowly increasing parameter (see Figure 3.6). After scanning over a whole plane, the height (z) is increased by the pitch Δz and the meander starts again at $(x_0, y_0, -z_0 + \Delta z)$ until the whole specified range $z \in \{-z_0, z_0\}$ is covered.

To prevent positioning and reading uncertainties of the Hall probe, a delay time of 200 ms is added at each grid point, before storing the gaussmeter reading, which assures that the reading is not influenced by the field in the vicinity, but equilibrated at the specified grid point. The maximum motor speed is user-adjustable, but was kept constant at $v_{\text{motor}} = 3\,\text{mm/s}$ over all measurements. This slow speed was chosen to avoid any vibrations of the probe and thereby prevent potential positioning uncertainties. At the same time the overall scanning time is kept below 24h for the largest volume scanned.

3.3.4 Definition of scan protocol and scanning setups

The main reason for scanning the magnetic field is to validate the FEM calculations performed using COMSOL Multiphysics. For this comparison, scanning all three field components (B_x,B_y,B_z) over the whole air gap and fringe field of the magnet would be ideal. However, the measurement setup sets certain limitations to the scanning procedure. Firstly, the probe holder does not allow to fully reach into the air gap of the magnet. Secondly, the 1D Hall probe with a rotatable holder allows for measuring two field dimensions using the same setup, but not the third.

Therefore, in a first setup (setup 1) the main field component B_z as well as the minor component B_x was measured. By rotating the magnet by 90° counter-clockwise around the z-axis, a second setup (setup 2) is defined. Setup 2 allows to measure the remaining B_y field component, as well as to remeasure the B_z component, in order to verify axis alignment between the two setups.

Due to the limitations in maximal possible measurement size, the scanning protocol for B_z is

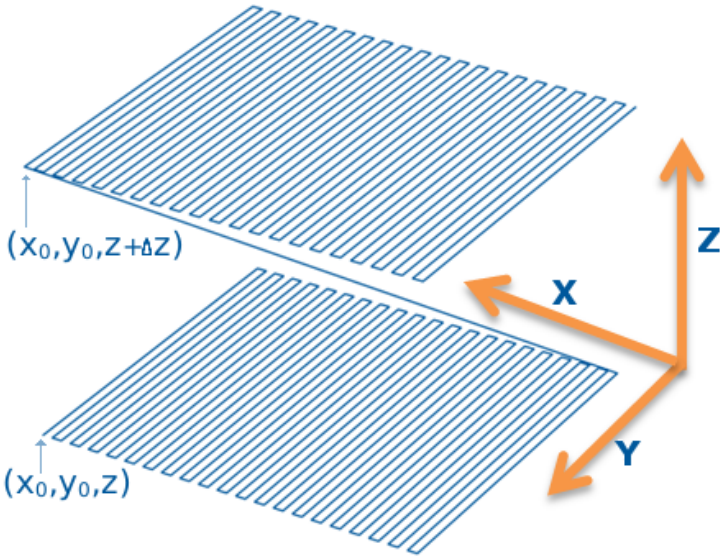

Figure 3.6: Measurement trajectory in 2 axial planes. Scanning the magnetic field in a meander in the x-y plane, starting at (x_0,y_0)*, with x being the slow parameter, while z is constant. Followed by an increase in* $z' = z + \Delta z$*, restarting the meander at the same* (x_0,y_0) *as in the previous plane.*

defined as a three step procedure. Firstly, central line scans are performed along the x- and y-axis, at $y = z = 0$ and $x = z = 0$, respectively. Here, the line scan range was chosen such that the magnets extent is completely covered and extends into the fringe field in both directions, limited only by the length of motor stages in x-direction and the maximal possible penetration of the probe and holder into the magnet's air gap for the y-direction. Secondly, a scan of the central x-y-plane is performed, again with $z = 0$. The exact parameters used for each of the scans ares given in Table 3.2.
By these two steps, the magnetic field's symmetry is verified on its main field component. Using the expected symmetry, it is reasonable to restrict the 3D scanning of the magnet to a quadrant sector, i.e. a quarter of the air gap and fringe area. Figure 3.7 shows a top view of the magnet defining the extent of the sector in both x- and y-direction. The z-range for the sector scan is maximized under the condition that the probe holder may not touch the magnet blocks, and is therefore limited to $z_0 = 15.0\,\text{mm}$.

Using the same setup as for the above defined measurements (setup 1), the probe is rotated by 90°(see section 3.3.5) to measure the B_x field component. This is done analogously by performing line scans along the x and y axes and a complete 3D scan of the sector.
For assessing the third field component B_y, setup 2 was used, which means that the magnet was rotated by 90° counter-clockwise by lifting the magnet up using a crane and positioning it back onto the optical plate. Note that for setup 2, the magnet's coordinate system was rotated against the motor system. In the following only the magnet's coordinate system will be used.
Using the 25 mm M6 screw grid of the optical plate in both setups, any potential alignment error was minimized. Nevertheless, line scans of the main field component B_z were repeated in this setup, as a means to compare against the previously performed scans in setup 1 in order to analyse the remaining axis alignment deviations between the two setups.
In a next step, the remaining third field component B_y was measured by performing a line scan over the y-axis of the magnet's coordinate system. This line scan yields information about the general

performed scan	B field component	ranges [mm]	pitch [mm]	setup
x line scan	z, x	$x = \pm 150$	$\Delta x = 2$	1
	z	x = (-25,235)	$\Delta x = 5$	2
y line scan	z, x	$y = \pm 80$	$\Delta y = 5$	1,2
	z	y = (-185,75)	$\Delta y = 5$	2
	y	$y = \pm 80$	$\Delta y = 5$	2
x-y plane scan	z	$x = \pm 150$	$\Delta x = 5$	1
		$y = \pm 80$	$\Delta y = 5$	
sector scan	x, z	$x = \pm 150$	$\Delta x = 5$	1
	y	$y = \pm 80$	$\Delta y = 5$	2
		$z = \pm 15$	$\Delta y = 2.5$	

Table 3.2: Performed scans, listing measured B field component (x, y or z), spatial x, y, z ranges , corresponding pitch and used setup (1 or 2). z is the direction of the main field component.

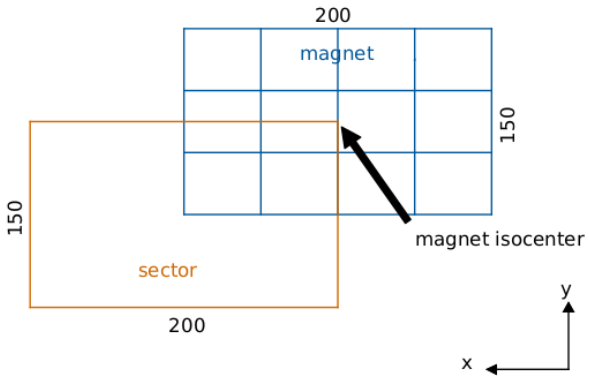

Figure 3.7: Top view sketch of the magnet, showing the magnet blocks in blue and the defined scan sector in orange, covering a quarter of the in-gap and fringe area of the magnetic field. All measures are in mm.

symmetry of the B_y-field component. As a last step, the sector scan was performed for the B_y component as well.

3.3.5 Probe adjustments and positioning uncertainty estimation

Spatial positioning uncertainty It is important to make sure that the measured reading of the Hall probe is assigned to the right spatial position. To guarantee this, two factors had to be assessed to the smallest possible uncertainty ($\Delta < 1\,\text{mm}$): the position of the Hall probes active area and the alignment of the probe movement with the coordinate system of the magnet.
To determine the actual position of the Hall probe's active area, the manufacturer's information (see Figure 3.4) was used along with an X-ray image of the probes stem (see Figure 3.3). The X-ray image enabled visualizing the interior of the probe and marking the centre of the active area ($A = 1.02\,\text{mm}^2$) on the brass stem.

The so-defined mark was used to align the Hall probe for B_z scanning (i.e. upright position of the probe) with the corner of the magnet. Adjustment in x- and y-direction was done visually by verifying that the marker was positioned exactly below the upper magnet-blocks corner, as looking form top-view, and adjusting the motor positions accordingly. z-positional adjustment required measuring the height distances between the probe and the magnet. The distance $z_u(z_d)$ between the upper (lower) end of the probe and the lower (upper) edge the magnet, was adjusted such that $z_u - z_d = 2\,d$. It was assumed here that the active area of the probe is at a position $d = 0.4\,\text{mm}$ above half thickness of the probe closer to the side of the probe being labelled with the Lake Shore logo, which is pointing upwards in all B_z measurements.
The measures regarding the active area were derived from information provided by the manufacturer, but an uncertainty of up to $\pm 0.5\,\text{mm}$ in x and y direction and $\pm 0.1\,\text{mm}$ in z have to be assumed. To validate this positioning error at the reference point an indirect reproducibility test was performed, where in a first step the local field gradient was determined in the vicinity of the reference point by scanning a $(5 \times 5 \times 5)\ \text{mm}^3$ area determining the maximum gradient in this region, followed by reproducing the reference position and measuring the field reading, from which a spatial deviation can be estimated through the field gradient. This procedure assesses uncertainties in the choice of the reference point. However, for the positioning error at any point in the measurement grid, a potential misalignment o the axes has to be taken into account in addition to the reference point uncertainty. This was quantified by driving the probe along the magnet edges and thereby measuring the axes angle error in both x and y direction. Due to the shorter extent in z direction and the magnets geometry, making such axis alignment checks intricate along the z-axis, this error was omitted, which seems justified by the fact that the magnetic field gradient in z direction is orders of magnitude smaller than in the x-y plane and therefore this uncertainty has a minor effect on the measurement data.

Probe adjustment for minor field components While the main field component reading B_z is comparably robust against both positional and angular adjustment uncertainties, special attention needed to be paid on the angular adjustment when measuring the minor components B_x and B_y. As described in section 2.3.3, the field reading depends on angular orientation of the probe, such that even a subdegree of angular misalignment leads to readings in the same order of magnitude as the expected field components for B_x and B_y. This is why special attention was paid to the angular fine-adjustment. The adjustment was performed at the isocenter of the magnet, assuming highest field symmetry here, therefore B_x and B_y are expected to be zero. The Hall probe was rotated by 90° relative to the B_z measurement and positional adjustment was verified at the reference point in the same manner as described above. The probe was then rotated in subdegree steps minimizing the field reading at the magnet's isocenter. This probe rotation re-adjustment procedure was also tested for reproducibility.

3.4 Potential radiation damage & quality assurance of the magnetic field

Magnetic field measurements provide an effigy of the magnetic field at the time of measurement. As the magnet will be exposed to radiation (see Part II) it is an open question whether the magnetic field will remain unchanged or is going to suffer from radiation damage.
A number of investigations show a relatively high radiation sensitivity for $Nd_2Fe_{14}B$ magnets as compared to SmCo [46, 47]. A theoretical study suggests domain reversal due to thermal spikes to be

the main reason for demagnetization [48]. Ito et al. [49] expressed flux loss $\Delta\Phi$ to be a logarithmic function of absorbed dose (under direct irradiation), i.e. $\Delta\Phi \propto \log(D)$, in a very high dose range between 100 Gy to several 100 kGy. Losses $\Delta\Phi$ of about 20% at 10^3 Gy were found for the most sensitive magnets studied, whereas a large diversity within different $Nd_2Fe_{14}B$ magnets was found. However, to our knowledge no such studies exist in the expected dose range for the experiments to be performed within this work and all existing literature investigated direct magnet irradiation only. Monte Carlo simulations of the planned experiment have shown that the maximum dose experienced by the magnet is about 1cGy per Gray deposited at the Bragg peak in the phantom [50]. The overall dose applied in the planned experiments is expected to be below 100 Gy. From these data, no measurable flux loss is expected during the irradiation experiments.

However, as this data does not allow a definite conclusion, the magnetic field was monitored for

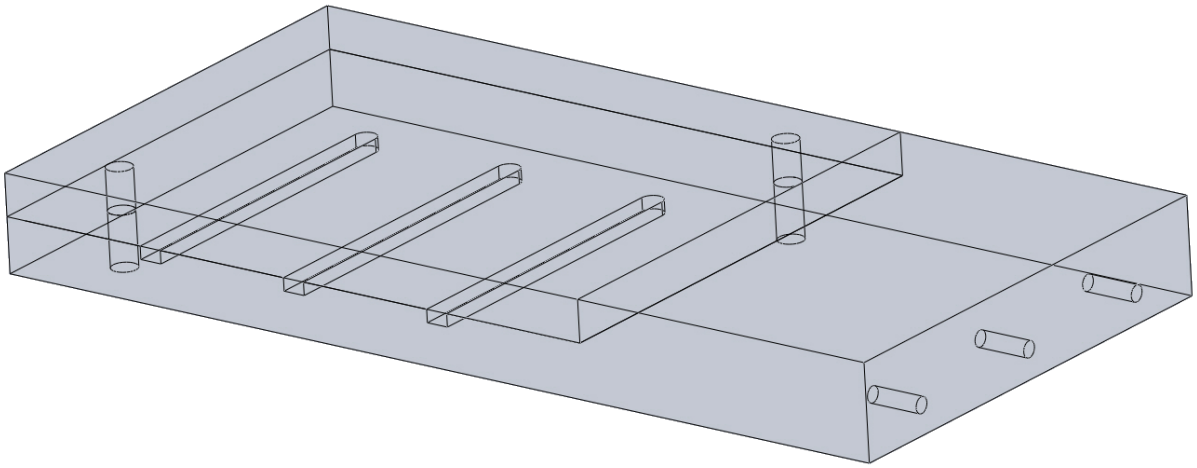

Figure 3.8: CAD iso-view of the QA phantom used for routine quality control of the magnetic field. The three voids in the phantom enable field measurements on the central beam axis, at 50, 100 and 150 mm depth, respectively.

any potential changes between the irradiation experiments. For this purpose, a dedicated quality assurance (QA) phantom was developed allowing to measure the magnetic field reproducibility in a setup resembling the irradiation experiments (see Part II).

The phantom is called QA phantom in the following. It consists of PMMA and has outer measures of $(300 \times 150 \times 30)\text{mm}^3$ (see Figure 3.8.) The magnetic field QA phantom has 3 voids at (x_v,0,0) with $x_v \in \{-50,0,50\}$ mm, which enable magnetic field measurement at the respective positions along the planned beam axis.

The magnetic field was measured with the procedure described in section 3.3.4 at the 3 spots to acquire reference values for the QA measurements. Furthermore measurements were preformed in a $(2 \times 2 \times 2)\text{mm}^3$ region around them, providing an uncertainty margin, enabling a discrimination of deviations caused by potential demagnetisation from those caused by positional misalignment.

Note that these measurements were performed both with the phantom in place as well as without the phantom to exclude a potential change in magnetic field due to the presence of the phantom. PMMA has a magnetic volume susceptibility χ_m of about -9 ppm [51] and hence no measurable change in magnetic field is expected.

4 Magnetometry Results

This chapter provides an overview of the most relevant magnetometry results from both the FEM calculations and the Hall-probe measurements. A validation of the FEM calculations against the measurements is performed and measurement uncertainties are evaluated.

4.1 Magnetic field map calculated by finite element modelling

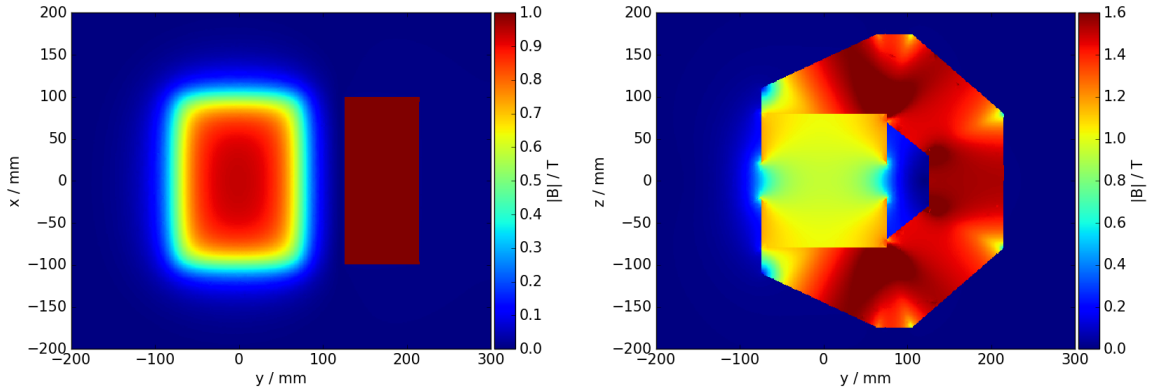

Figure 4.1: Calculation result of magnetic flux distribution norm $|B|$ in two planes over the whole geometry implemented in COMSOL. Left is the central air gap plane (z=0) and right is the x=0 plane.

Calculating the magnetic field of the magnet assembly using the FEM software COMSOL as described in chapter 3.2 yields a complete solution of the magnetic field in the whole simulation box, see Figure 4.1. However, for further analysis and comparison to the measurement results, the air gap of the magnet and the near fringe fields are investigated in more detail.
Figure 4.2 gives a vector field representation of the magnetic field in a central volume of $(400 \times 300 \times 30)$ mm^3. The magnet's yoke is visible as a dark red area of strong magnetic field, pointing in the opposite direction than in the air gap. This matches the expectation of closed magnetic field lines over the whole magnet assembly.
As expected, the magnetic field between the magnet poles shows a plateau region, with the field pointing into the z-direction (downwards) and being relatively constant over a large volume. In the vicinity of the magnet's edges, the field strength decreases rapidly and develops a small component perpendicular to the z axis. This component points away from the isocenter of the magnet for $z<0$ and towards the isocenter for $z>0$. Keeping in mind that the z axis is defined to point from the North (N) towards the South (S) pole of the magnet, this matches the expectations of field lines from N to S pole. For magnetic safety reasons the maximum distance from the magnet's isocenter to the 5 Gauss line, was measured. It amounts to less than 30 cm, which gives a minimum distance to be kept from the magnet while operation with ferromagnetic materials and during magnet storage.

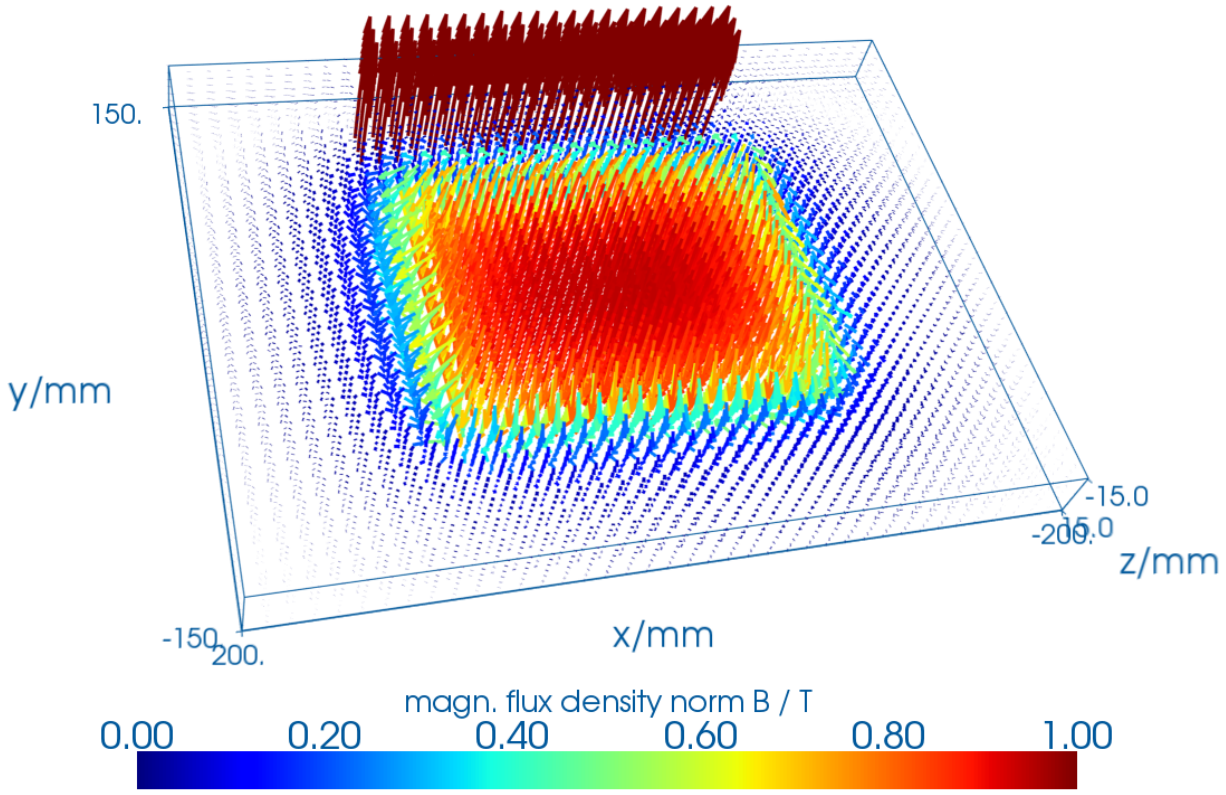

Figure 4.2: Vector field representation of the magnetic flux density as calculated by COMSOL, extending over the whole magnet area and surrounding fringe field. The dark red area in the background is the magnet's yoke, in which the field is strongest (≈ 1.6 T).

4.2 Field measurements in 3D & Comparison to FEM data

Positioning accuracy and inter-setup alignment

As described in chapter 3.3.5, for each measurement the Hall probe is adjusted at a reference point with an uncertainty in x- and y-direction of $\Delta x \leq \Delta y \leq 0.5\,\text{mm}$. The maximum local B_z field gradient in a $(5 \times 5 \times 5)\text{mm}^3$ grid around the reference point was calculated to be $16.9\,\text{mT/mm}$. In a reproducibility test, adjusting the probe three times onto the reference point, maximum field reading differences were $\Delta B = 5\,\text{mT}$, which corresponds to a positioning uncertainty of less than $5/16.9 < 0.3\,\text{mm}$. This lies within the above mentioned criteria. To obtain positioning uncertainty for each measurement spot, two aspects were verified: firstly, axis angular misalignments between the magnet and motor system were found to be $\Delta\alpha_x \approx 1\,\text{mm}\,/100\,\text{mm}$ and $\Delta\alpha_y \approx 0.5\,\text{mm}\,/100\,\text{mm}$. Secondly, absolute positioning uncertainty by the motor system was measured and found to be less than 0.1 mm.
Figure 4.3 shows line scans along the x- and y-axis comparing the B_z component measured using setup 1 and 2. The setups axes agree within the above mentioned uncertainties. Thus no additional setup uncertainties have to be introduced. This result confirms that the measurement results from the two different setups can be combined in the following.

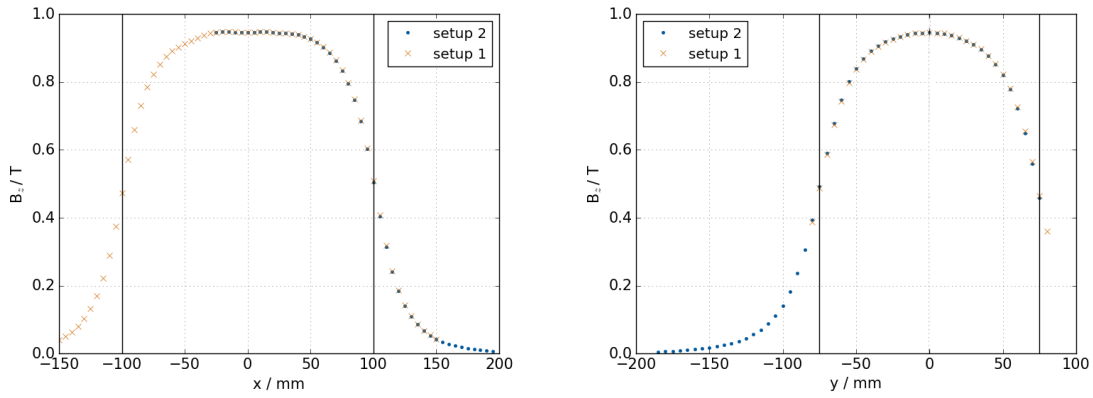

Figure 4.3: Scans of the main magnetic field component B_z along the x (a) and y (b) axis of the magnet, as performed in both setups 1 and 2 to compare the axis alignment of the setups. Vertical black lines represent the rims of the magnet.

4.2.1 B_z - Main component measurements

As presented in Figure 4.3, both the central x- and y-axis scans of the main field component B_z show a plateau region within the magnet's air gap, with a field maximum of 0.95 T at the magnet's isocenter. The high gradient area shows a sigmoidal drop-off with the inflection point at the magnet's edge, which is $\pm 100\,\text{mm}$ and $\pm 75\,\text{mm}$ for the x and y direction, respectively.
A comparison of FEM calculations and measured line scans is displayed in Figure 4.4. The upper plots show symmetric x and y scans of B_z, both measured using setup 1, plotted against the FEM calculation results. Black lines represent the edges of the magnet. For the x-axis scan, additionally a reference scan from the magnet's manufacturer, which was performed before shipping of the magnet in 2008, is added to the graph, showing agreement with measurement within 5 mT and 0.5 mm.

region	mean ΔB_z/ mT	maximum ΔB_z/ mT
plateau	+10.9	+23.3
gradient	+13.4	+32.1

Table 4.1: Differences between measured and FEM calculated B_z field for plateau and gradient area. Extend of the regions are defined in the text.

The lower plots in Figure 4.4 represent field differences $\Delta B = B_{\text{measure}} - B_{\text{simulate}}$ between measured and calculated magnetic field strength. The calculation underestimates the measured field strength by a mean ΔB of 12.4 mT in the x-scan and 7.3 mT in the y-scan. Largest deviations were seen near the rims of the magnet.

The measured field in the central x-y-plane of the air gap, corresponding to $z = 0$, is shown in

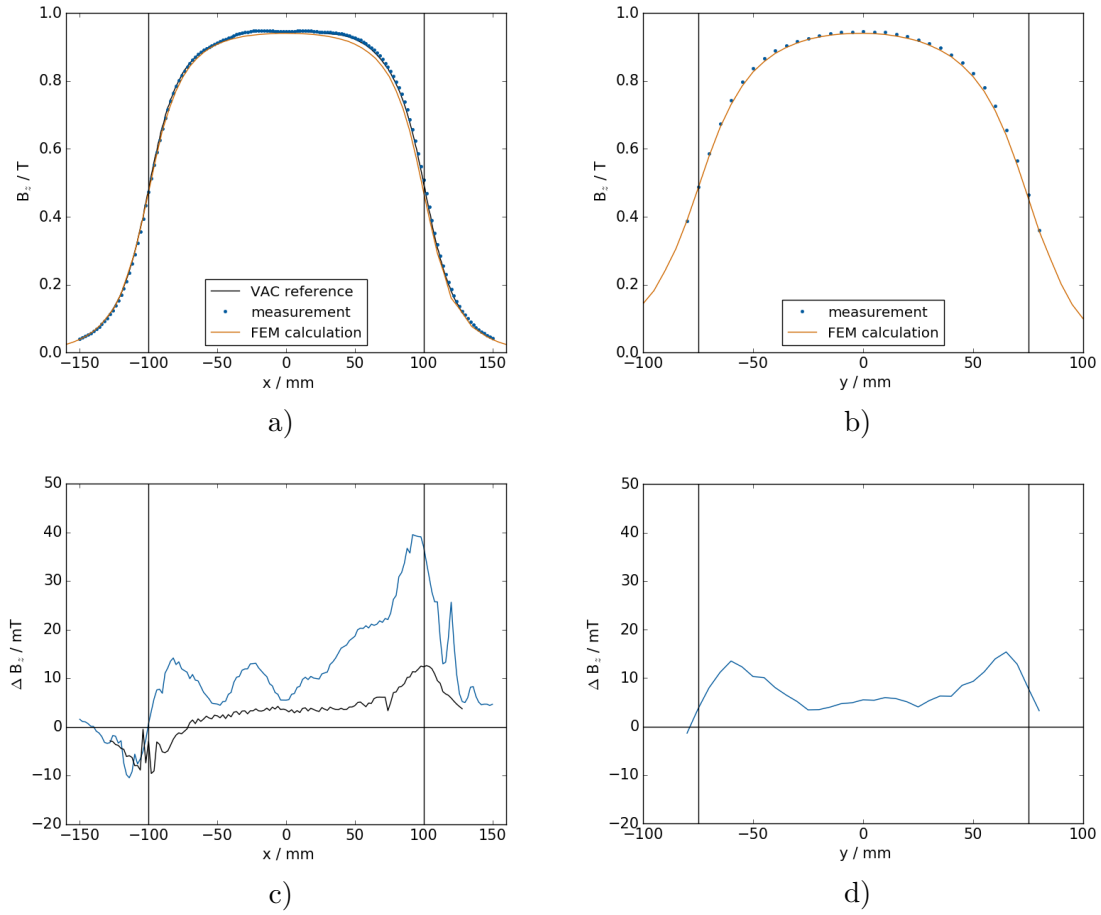

Figure 4.4: Comparison of the main magnetic field component B_z obtained by measurement and simulation, along the x- (a) and y-axis (b). Corresponing differences ΔB (blue) are given in c and d. For the x-scan a reference scan (black) and its difference to the measurement is added in a and c. Black lines mark the magnet's rims.

Figure 4.5a. The black dotted line marks the physical edge of the magnet. The strong gradient field fall-off, along the magnet's rims is clearly visible. In Figure 4.5b the calculated difference map $\Delta B = B_{measure} - B_{simulate}$ is shown in units of mT, with the dotted lines defining two separate regions. First, the plateau region is defined for all $x \in [-75{,}75]$ mm and $y \in [-45{,}45]$ mm. Second, extending around the plateau the gradient region is defined to be within ± 115 mm for x and ± 75 mm

for y, without the inner plateau area.

For both regions, mean and maximum differences in ΔB_z are summarized in Table 4.1. As observed in the x- and y-line scans, the FEM calculations show an underestimation in the B_z field in the order of ten mT in the plateau region. Within the gradient area, deviations are larger and show an underestimation of the field within the FEM calculation, with maximum $\Delta B = 32.1\,\mathrm{mT}$. Moreover, largest deviations are seen at the magnet's corner being the furthest away from the reference point (x_r,y_r) = (-100, -75) mm). This agrees with the tendency already observed in the x line scan, where deviations in the gradient area away from the reference (positive x values) are stronger than the one close to the reference (negative x values) point at $x = -100\,\mathrm{mm}$, see Figure 4.4.

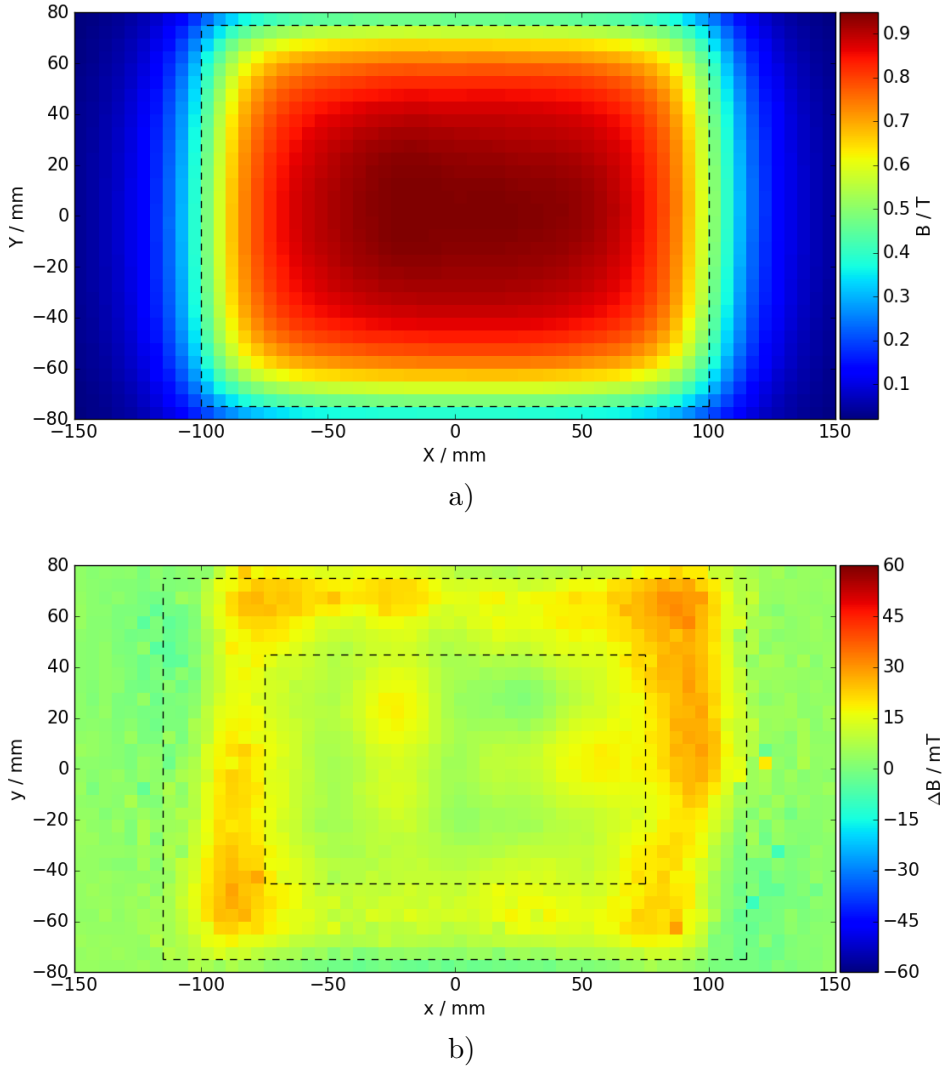

a)

b)

Figure 4.5: a) Scan of B_z field component over the central x-y-plane. The black dashed line represents the physical edges of the magnet. b) Calculated difference map of ΔB. Gradient (outer) and plateau (inner) region are marked by black dashed lines.

4.2.2 B_x and B_y - Minor component measurements

In contrast to the main B_z field component, which could be measured to a high precision and accuracy as presented above, the minor components B_x and B_y were expected to be very small. Therefore the measurement suffers from a very strong dependency on angular adjustment of the Hall-probe, as can

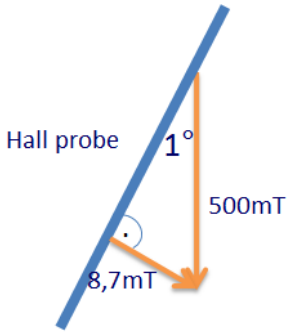

Figure 4.6: Angular dependency of Hall probe measurement, perpendicular to the main field component. Here the Hall probe is depicted by the blue line, being misaligned by 1° relative to the B_z field of 0.5 T leads to 8.7 mT additional field reading.

be seen in Figure 4.6. A possible misalignment of only 1° away from the intended x- or y-axis results in a significant influence of B_z on the field reading in the same order of magnitude as the B_x or B_y field component.
This can be observed in the B_x line scans along both central x and y axis, see Figure 4.7. Both line scans illustrate the effect and importance of probe readjustment at the magnets isocenter, as described in chapter 3.3.5. The offset between pre- and post-readjustment scans agrees within 10 mT, which corresponds to the 1° misalignment example shown in Figure 4.6. These measurements, including probe readjustments have been performed several (two and three times for x and y scan, respectively) times, to assure field measurement reproducibility. The result can be seen in Figure 4.7: All curves after adjustment (orange) agree within a few mT, which proves the chosen method to be applicable. Nevertheless, due to the uncertainties mentioned above, only qualitative results are taken from these scans. Most importantly, the symmetry behaviour of the field along the main axes is studied. The central x line scan of B_x, i.e. the scan along the measured field axis shows a clear antisymmetry relative to the magnet's isocenter ($x = 0$), whereas the scan along the orthogonal axis to the field, does not show such a behaviour and almost no signal at all. This can be understood from the magnet's geometry, as line scans along the central y axis keep constant x at the centre, where B_x is expected to be minimal, e.g. zero. Analogous considerations apply to the B_y line scans, which are therefore omitted.

4.2.3 $\vec{B}$ - Measurement vector results

In the previous sections, only line and planar scans of the magnetic field have been investigated, which were capable of providing an estimate of the general field properties, such as symmetry and shape. Nevertheless, to go into more detail and exploit the whole capacity of the measurement setup, the three dimensional sector results are presented and compared to the COMSOL $\vec{B}$ field grid presented in section 4.1.
Figure 4.8 shows the results of the sector field scans, as described in chapter 3.3.4. The magnet extends over the upper right quarter of the plot, showing the plateau region between the magnet arrays with a relatively homogeneous field and the sharp gradient area, where the field bends out of the strict B_z orientation of the plateau.
The presented sector vector data are compared to the FEM results acquired for the same region, by generating a difference map, where each grid point represents the vector difference between

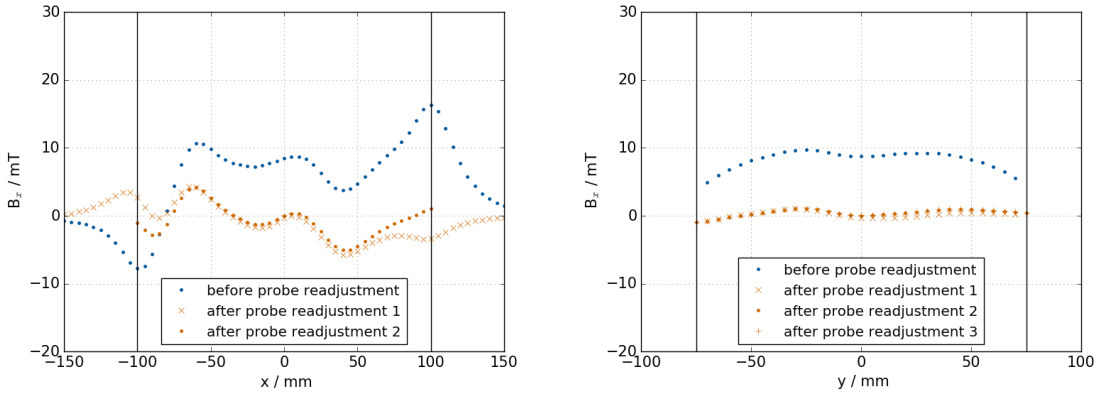

a) b)

Figure 4.7: Scans of the minor magnetic field component B_x along the x (a) and y (b) axis of the magnet, both before and after probe readjustment. Black vertical lines mark the rims of the magnet.

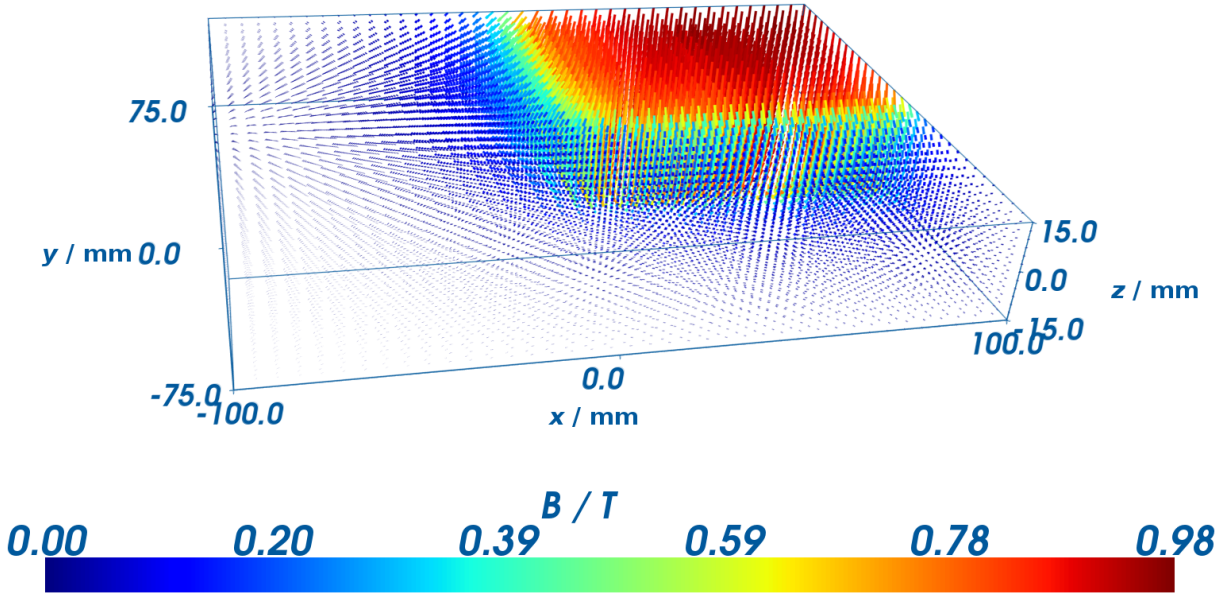

Figure 4.8: 3D Vector plot of the magnet's sector, obtained by scanning all the field components on an identical grid.

measured and simulated field. The difference map is shown in Figure 4.9. Differences are largest in the gradient-, i.e. near fringe field-area, with difference vectors mainly orientated along the z axis, pointing upwards along the magnet's longer rim and downwards along the shorter rim. One observes a tendency of stronger deviations further away from the corner, which was the reference point during the measurement (defined as $(x_r,y_r,z_r) = (0,0,0)$ in Figure 4.9). This indicates a very minor tilt in magnet to motor coordinate system alignment, as already seen in section 4.2.1.
In the far fringe fields, meaning all grid points further than 30 mm away from the magnet rims, field differences are negligible. Within the plateau region, defined by $x_p = (15,100)$ mm, $y_p = (15,75)$ mm and $z_p = (-15;15)$ mm the mean vector field difference measures 21.5 mT. A second region of interest was defined as the central beam axis, represented by an orange arrow in Figure 4.9 and given by: $y = (70,75)$, $z = (-5,5)$ and $x = (-100,100)$, to estimate the field difference experienced by the proton beam during irradiation experiments. Mean and maximum differences are 16.4 mT and 51.5 mT respectively.

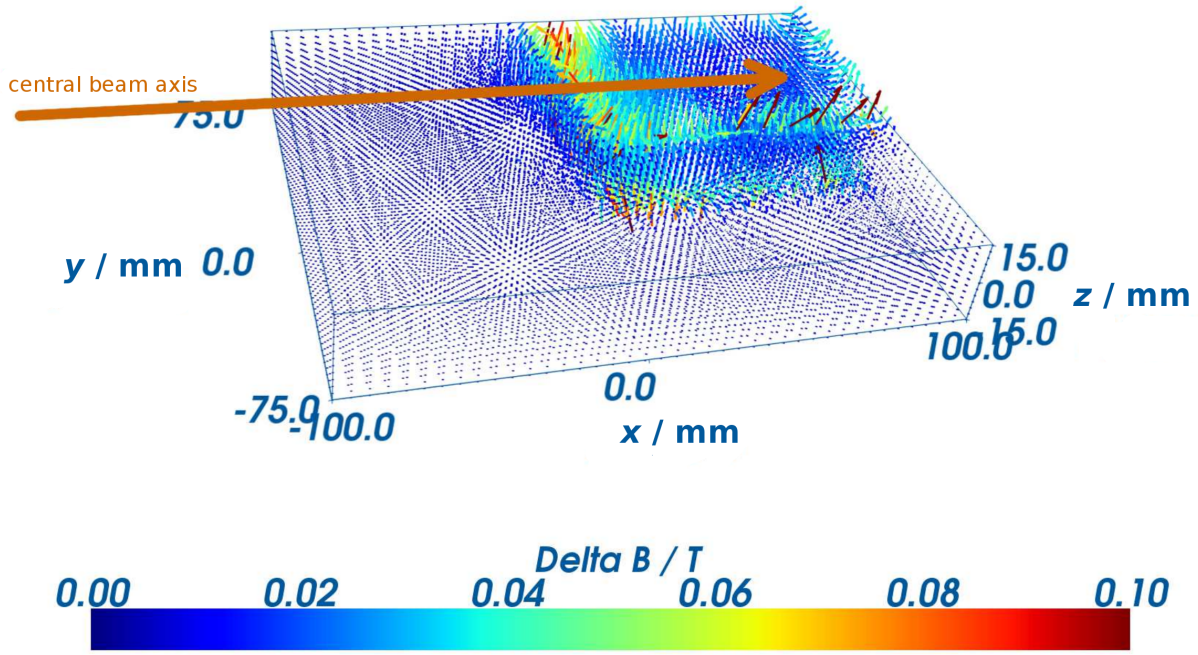

Figure 4.9: 3D Vector plot of the magnet's sector showing the difference between magnetic field obtained by Hall probe measurement and simulation by COMSOL. The magnets quarter is visible in the upper right corner, showing a small (20 mT) underestimation of the magnetic field in the plateau area and stronger deviations in the gradient region. The central beam axis is indicated by an orange arrow.

4.3 QA measurement results

The reference field values at the three defined QA spots along the central x-axis, together with deviations within 2 mm spatial surrounding are presented in Table 4.2. No differences were found between measurements performed in air and those with the PMMA phantom in place. Following, the quality control over a course of almost 6 month are presented in Table 4.3, with repeated irradiation measurements having been performed in this time window. All spot measurements of the magnetic

QA-1 / T	QA-2 / T	QA-3 / T
0.913 ± 0.05	0.945 ± 0.01	0.926 ± 0.04

Table 4.2: Reference field values measured for quality control spots 1,2 and 3, together with maximum deviation within a $2 \times 2 \times 2\,mm^3$ *surrounding.*

field are within the tolerances given in Table 4.2, thus suggesting no effect of demagnetisation caused by repeated irradiation experiments performed with the magnet.

Date	QA-1 / T	QA-2 / T	QA-3 / T
08.08.16	0.913	0.946	0.926
11.08.16	0.915	0.946	0.926
16.09.16	0.914	0.945	0.926
19.09.16	0.913	0.945	0.923
04.10.16	0.913	0.944	0.925
05.10.16	0.912	0.945	0.924
08.10.16	0.915	0.944	0.924
08.10.16	0.915	0.944	0.926
21.11.16	0.915	0.944	0.925
24.11.16	0.914	0.944	0.925
21.12.16	0.914	0.945	0.926
24.01.17	0.915	0.945	0.927
25.01.17	0.914	0.944	0.926

Table 4.3: Summary of all quality control spot measurements performed. Field variation is within the uncertainties of the references (compare Table 4.2).

4.4 Discussion

The magnetic field of the dipole magnet was characterized by magnetic field mapping. Field maps were created by the means of both numerical calculations and 3D Hall-probe field measurement.
Line scans showed the symmetry and shape of the magnetic field in all three field components. The main field component B_z was described by two areas, a plateau area between the magnet blocks, with a maximum field reading of 0.946 T and a gradient area in the vicinity of the magnets rims, with field gradients up to 40 mT/mm.
The minor field components B_x and B_y are two orders of magnitude smaller then the B_z component and show an asymmetric behaviour along scanned lines parallel to the main axes. Their magnitude is largest within the gradient area, as field lines bend away from parallel orientation to the magnets z axis.
The main field component measurements show small uncertainties, about 0.5 % of field reading due to the precision of the Hall-probe and agree to a reference curve within this uncertainty in the plateau

region. Larger deviations in the gradient can be attributed to positioning uncertainties.
On the other hand the minor field components suffer from a strong dependency on the probe orientation angle, where only slight misorientation leads to uncertainties of the same or even higher magnitude as the flux density to be measured.
Vector field information by measurement could only be acquired within a defined magnet's quadrant (sector), due to limitations in the experimental setup and the thin air gap of the magnet, restricting the motor movement and Hall probe penetration depth between the magnet arrays. However, as the line scans described above proof the symmetry of the magnetic field, obtained results within the sector are expected to represent the whole flux distribution of the dipole magnet.
Vector field maps of measured and calculated data show differences, with an almost constant underestimation of the magnetic field norm by the calculation in the order of 20 mT within the plateau region of the magnet. The underestimation amount to about 2% of the field reading and is therefore higher then the Hall-probe measurement uncertainties (0.5%). Even stronger deviations were seen in a small band around the rims of the magnet, where the field rapidly drops. Differences in this region can be attributed to two main reasons: first a slight positioning and axis alignment uncertainty of the motor system relative to the magnet coordinate system, that has its main effect in the regions of high gradient, and second, boundary artifacts from the numerical calculation. Although, the latter have already been reduced by adopted calculation meshing in the magnet's air gap, they still play a role at material boundaries.
Determination of uncertainties for the FEM simulation is difficult, as the input parameters, mainly the remanent field strenght of the $Nd_2Fe_{14}B$ material is not specified with an uncertainty by the manufacturer as well as the exact material compositon of the iron yoke being unknown. Thus, the $B(H)$ response could only be estimated by the choice of picking a likely curve implemented in the COMSOL material library for the material 'soft iron'.
However, usability of the resulting field map should be decided according to the desired use. The difference between measurement and simulation has to be kept in mind and used as uncertainty for the field information.
The main aim to perform such a field analysis was the desire to use magnetic field information for future Monte-Carlo simulations of the experimental setup presented in part II. Thus the difference in magnetic field should be investigated in relation to resulting beam deflection changes from field uncertainties. Wolf et al. [52] presented an analytic model to calculate the total Bragg peak deflection in a transverse uniform magnetic field. The lateral deflection was found to be linearly dependent on the transverse magnetic flux density. This result suggests that an underestimation of the B_z field in the simulation which amounts to 10 mT and thus 1 % would result in a 1 % deflection underestimation. This hypothesis was validated using the RAMDIM (Raytracing Algorithm for Magnetic Deflection of Ions in Media) iterative model suggested by Schellhammer and Hoffmann [53]. Lateral beam deflections in water were calculated for both field strength of 0.95 and 0.94 T, resulting in lateral deflections of 12.71 and 12.58 mm at the Bragg peak, respectively. Thus, the deflection difference could be determined to be 0.13 mm or 1 %, as predicted above. This deflection difference is smaller then the uncertainties within the setup developed in part II and also looking into future clinical application, a tolerance on deflection of 0.5 mm would seem tolerable.
Nevertheless, regarding future investigations, it could prove worthwhile to further adapt the FEM model of the magnet, to try to match measurement results.

Part II

Development of a proton pencil beam setup for in-magnet measurements

Having characterized the magnetic field of the dipole magnet in part I, the rest of this work focusses on the development and optimization of an experimental setup to perform proton irradiation experiments in the presence of the magnetic field, within a tissue-equivalent material. The developed setup is then used for the experimental investigation on proton pencil beam deflection within this context.
Within the material and methods chapter 5 each setup component is presented and irradiation experiments performed are explained in detail. Corresponding result will be shown and discussed in chapter 6.

5 Material and Methods

5.1 Definition of requirements

Starting the development of an experimental setup for irradiation experiments, a number of requirements had to be defined, which together with existing limitations formed as basis for the construction of the setup presented here. The main aim of this study was to measure the proton pencil beam deflection in a magnetic field, while being slowed down in a tissue-equivalent phantom. The first requirement is therefore a proton beam, collimated down to a pencil beam. The pencil beam technique was chosen for two main reasons: firstly, a number of simulation studies regarding potential future MRiPT [7, 9, 10, 52] all consider pencil beam scanning to be the preferred technique over passive scattering and secondly, due to the thin (4 cm) air gap of the magnet, the beam has to be collimated to minimize radiation dose on the magnet, as the permanent magnet's field is sensitive to irradiation [46](see chapter 3.4).
The next requirement is a suitable detector for dosimetry, which fits into the air gap of the magnet while being large enough to detect the whole dose distribution in 2 dimensions. The detector should consist of non-magnetic material, offer a high spatial resolution and have minimal and known magnetic field effect with a dose response level in the order of therapeutic fraction size, i.e. 2 Gray [54].
Moreover, this detector needs to be placed in a phantom designed to also consist of non-magnetic material which is at the same time comparable to water regarding its proton stopping power. The phantom has to meet the physical extent of the magnet and should be held in place by a holding device, which is important, as it enables acquisition of reference data without the magnet in place. As a last requirement the setup needs to assure reproducibility of all performed measurements.

5.2 Development of the experimental setup

During the development of the experimental setup, for almost each component, different options have been tested. This section aims to present not only the final choices for all beam setup components, but present some approaches studied, while focussing on the reasoning behind the final decision.

5.2.1 UPTD proton facility

All proton measurements within this thesis were performed at the UPTD (University Proton Therapy Dresden) facility(see Figure 5.1). The protons were accelerated by a *Proteus-235 Isochronous Cyclotron* (IBA International, Louvain-La-Neuve, Belgium), which accelerates protons to a constant energy of about 235 MeV. Additional to the clinical beamline, the proton facility offers a separate static beamline for experimental purpose which was used for all measurements. Beam energies between 70 MeV and 230 MeV can be requested in the experimental room, with protons being slowed down from the initial 235 MeV in the Degrader, by insertion of a graphite wedge, and selection of the requested energy within an Energy Selection System (ESS), that decreases the energy width to about 1.5 MeV [50].

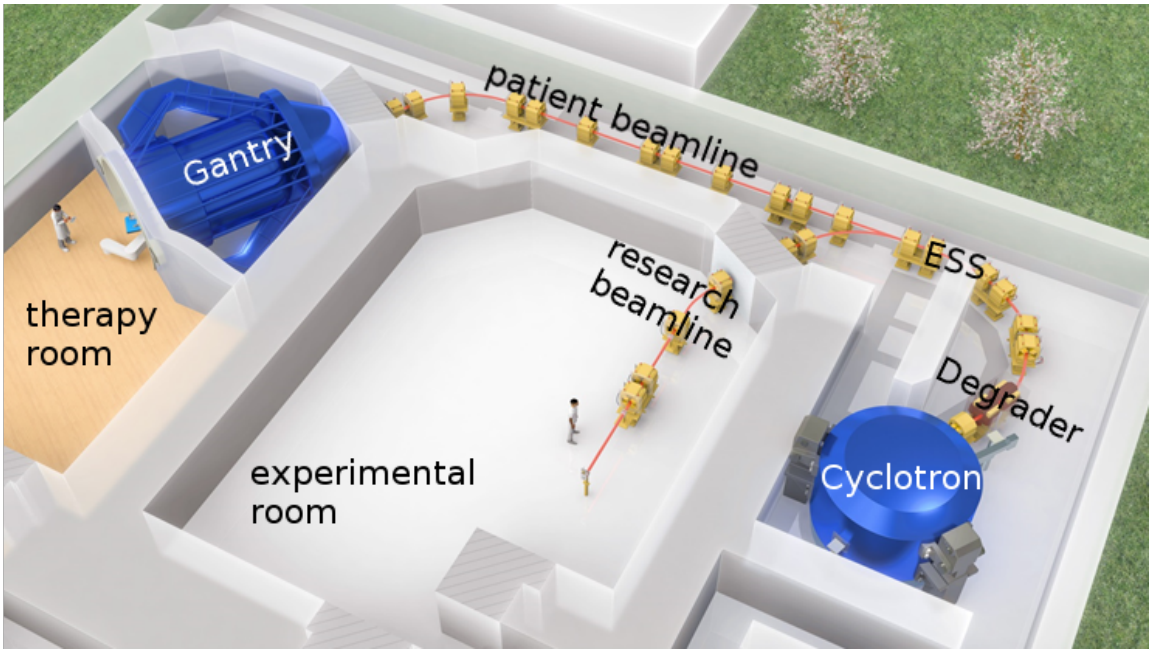

Figure 5.1: Schematic overview of the UPTD facility: protons are accelerated to 235 MeV in the cyclotron, slowed down in the Degrader, energy is selected in the ESS and a dipole magnet splits the beamline into the patient beamline leading to the gantry in the therapy room and the research beamline into the experimental room.

5.2.2 Beam collimators

As explained in section 5.1 the beam needs to be collimated, to both mimic a therapeutic pencil beam and to spare the magnet from being exposed to incident radiation. Two cylindrical brass collimators with a diameter of 9 cm and a thickness of 3.3 cm each were placed at a distance of 168 cm away from the beam snout, measured from snout to first collimator surface, with a separation of 1.7 cm between the collimators (see Figure 5.3). Using two collimators was necessary as a single 3.3 cm brass (63 % Copper, 37 % Zinc) collimator only stops protons with a range up to $R = 17.4\,\mathrm{g\,cm^{-2}}$, which is equivalent to an initial energy of approximately 159 MeV. However, higher energies should be used within the experiments, demanding the use of a second collimator.
Two sets of collimators with central circular aperture of 5 mm and 10 mm were tested. Using the 10 mm diameter set of collimators was chosen over the smaller diameter ones, as the Bragg-Peak on the 2D detector plane is less pronounced using a smaller beam. This can be understand by the fact that for small beams, the fluence on the central axis decreases with depth, due to scattering, which cancels the tendency of the stopping power to increase with depths [55].
Lateral positioning of the collimators was adjusted to get the most possible symmetric beam profile behind the collimator. This was necessary, as the beam profile leaving the snout, i.e. before the collimators was found to be asymmetrical and the beam axis having an angle of about 0.1 ° relative to the room laser system. Both those effects have a slight dependency on beam energy, which is most likely caused by the bending and quadrupole magnets of the beamline.
However, changing collimator positions depending on used beam energy during experiments was infeasible. Therefore, an average optimal position was chosen, offering a compromise in beam profile symmetry over the range of beam energies between 80 MeV and 180 MeV. For the final lateral collimator offset from the central beam axis, which amounts to 2,5 mm, beam profiles are presented in Figure

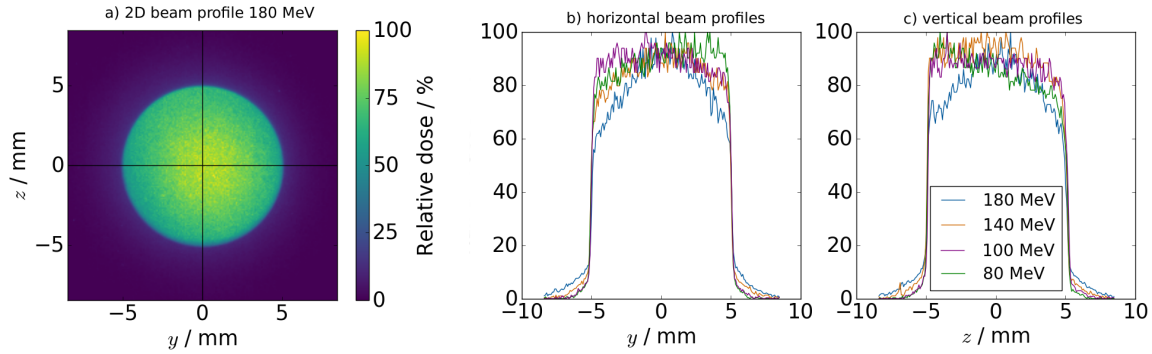

Figure 5.2: Proton beam profiles behind the 10 mm collimators. a) 2D beam profile for a 180 MeV beam, b) horizontal and c) vertical 1D profiled for the four studied energies (80,100,140,180 MeV).

5.2. A relative 2D beam profile behind the collimators for a 180 MeV 10 mm pencil beam is shown in Figure 5.2a, while a comparison of relative vertical and horizontal 1D profiles are given for the four studied energies of 80, 100, 140 and 180 MeV in Figure 5.2b and 5.2c, respectively.

5.2.3 Choice of detector: Gafchromic films

Choosing an appropriate detector for the irradiation measurements was mainly guided by the size limitations in the magnet's air gap and the need for a detector operating in a strong magnetic field of almost 1 T. High resolution silicon detectors are in the development process and an experimental 2D cross-hair detector [56] has even been tested within the setup described here, but no such system was available to use for this work. A further alternative would have been an ionisation chamber on a motorized positioner inside a water phantom to scan a 2D plane. However such an option would be technically quite challenging on the small volume available and a recent study [57] has shown ionization chambers to have a significant magnetic field dependency.
Therefore, radiochromic films were considered. They are a standard dosimetry tool in radiation therapy, have a well-studied dose response and offer a number of properties that are well suited for the task to be performed. EBT3 Gafchromic films (Ashland, Covington, USA) are only 270 µm thick and have a high 2D resolution, mainly limited by the used scanner, typically 300 dpi [30]. Their sensitive dose response is best in the range between 1 Gy and 10 Gy. For more detail, see section 2.4.1.

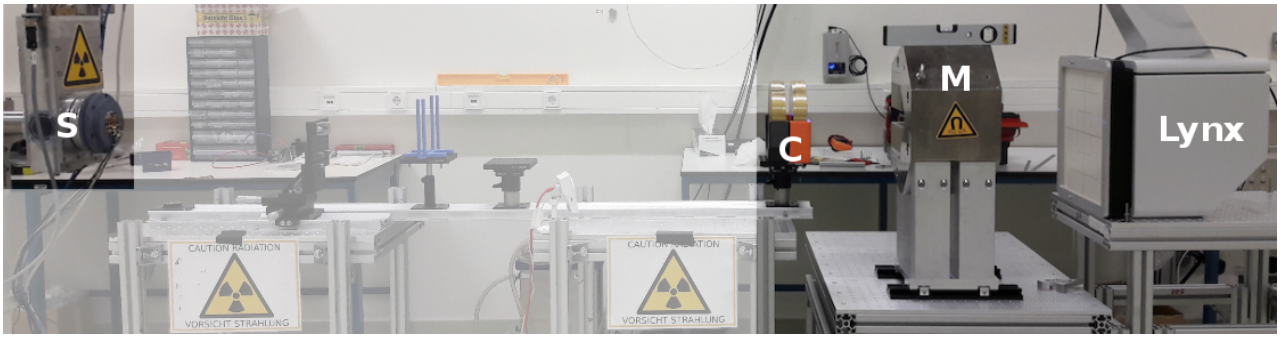

Figure 5.3: The two cylindrical brass collimators (C) are positioned at 168 cm from the beam snout (S). The magnet (M) to Snout distance amounts 202 cm. For the transmission experiment additionally the Lynx detector is placed 26 cm behind the magnet.

Magnetic field influence of dose response on EBT3 films was only studied by a few investigations, suggesting either no effect within their measurement uncertainties [58, 59] or only a minor, 4 % underresponse [60] on absolute dose. However, radiochromic films are an offline dosimetry tool, which require post-irradiation scanning and evaluation, using a calibration curve to convert changes in optical density into dose, see chapter 2.4.1.

5.2.4 Phantom design

Designing a phantom for irradiation measurements, a number of properties have to be set. First of all, several options for the material to use were investigated. The ideal tissue equivalent material would have been water, as the human body mainly consists of it. However, having a liquid as phantom material would require a container, thereby introducing material inhomogeneities and also handling would be difficult, as the film detector needs to be changed after each irradiation. Polymethylmethacrylat

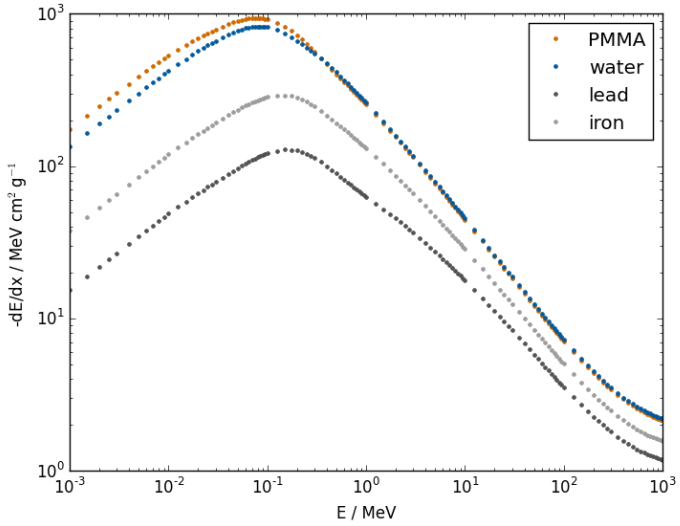

Figure 5.4: Stopping power of various materials as a function of residual energy, data from ICRU49 [61].

(PMMA) is widely used as a phantom material in radiation oncology [62], featuring an electronic stopping power very similar to water over a wide range of proton energies, see Figure 5.4, which results in a water equivalent ratio (WER) of 1.158 [18]. Constructing a phantom from PMMA is easy as it can be manufactured into any desired geometry. A slab phantom geometry was chosen, holding the EBT3 film detector between two slabs of PMMA, with the middle plane having an inclination angle of 1° in beam direction. This angled plane reduces, firstly, the dependence of the dose distribution on the film material, as it leads to less protons travelling a long distance through the film. Secondly, the inclination angle also reduces the effect of a potential air gap between phantom slabs and film [32].

To assure reproducible positioning of the film detector within the phantom, two pins were added, with corresponding holes in the films. The pin positions were chosen such that misorientation due to film flipping or rotation was avoided and the holes have an angle of 45° relative to the phantom's longer edge. Figure 5.5 shows a CAD isoview of the phantom, which is 300 mm long, 150 mm wide and 30 mm high. In addition to the two registration pins 6 screw holes were drilled into the phantom, 4 in the front area, from top to bottom and two in the middle, from bottom to top of the phantom. Screwing the phantom plates together was necessary to further reduce air gaps between the plates

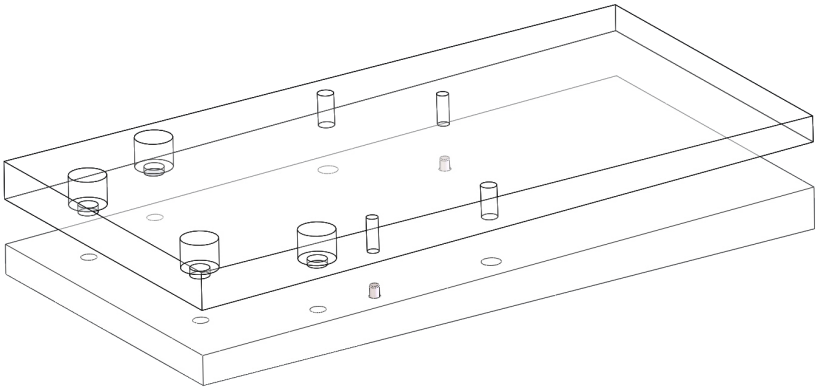

Figure 5.5: CAD isoview of the PMMA slab phantom.

and film. It was found that using 4 screws, the two very first and the two rear screws, dose artifacts, which could be attributed to air gaps, could be minimized. Therefore this 4 screw configuration was used in all final phantom experiments.
For positioning the phantom both within the magnet, as without the magnet (for reference measurements) an aluminium phantom holder was constructed, that connects to the phantom using three PMMA screws at the rear end of the phantom. Figure 5.6 depicts the phantom, in the air gap of the magnet, being held by the phantom holder.

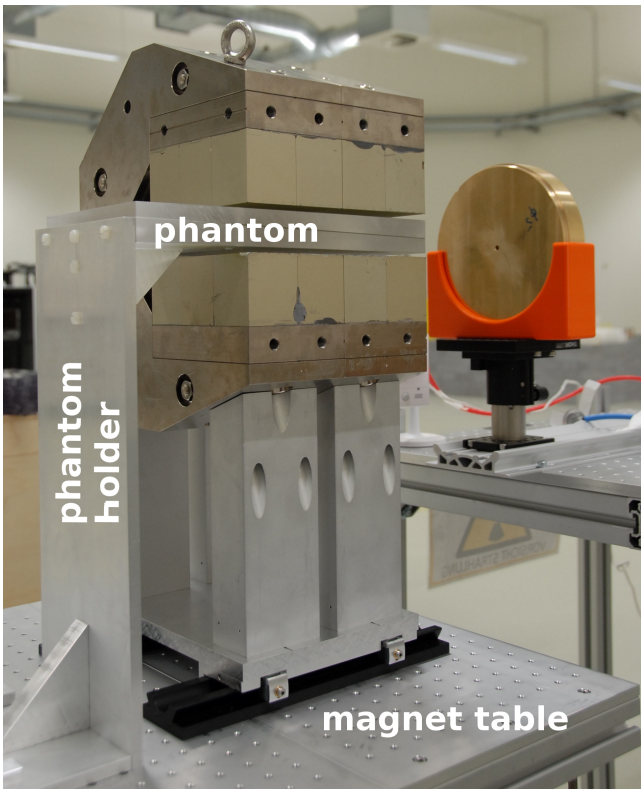

Figure 5.6: Setup of the slab phantom being held in the magnet's air-gap. The phantom holder position is clamped onto the magnet table.

5.2.5 Magnet table

For irradiation experiments the magnet was positioned at the room laser isocenter of the experimental room, to assure reproducible alignment relative to the collimators and thereby the proton beam. This requires a height and balance adjustable table large and stable enough to support the magnet and perform reference measurements without the magnet. The tabletop is equipped with an optical plate with a screw grid identical to the one used for the magnetometry experiments described of part I. The proton beam in the experimental room has a height over ground level of 127.0 cm, the magnets support setting the center of the air gap 38.0 cm above table level, resulting in about 89 cm required table height. The magnets tabletop is levelled using three pins, which enable separate height and horizontal level adjustment.

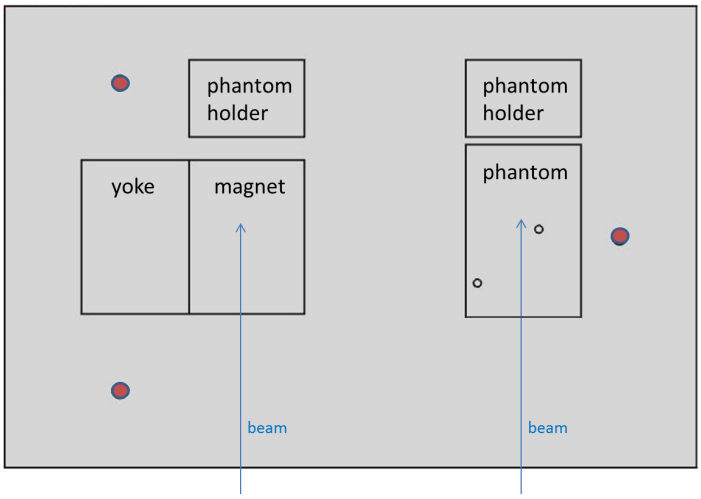

Figure 5.7: Top view on the magnets table, red dots are the three pins used to level the tabletop. Setup for both in-magnet (left) and reference (right) measurements are shown. For reasons of visibility the phantom is not shown in the magnet.

5.2.6 Film preparation

The EBT3 films were all taken from batches of initially 8" × 10" (inch^2) and then cut to match the size of the phantom (150 × 200 mm^2). Pin-holes were created using an A4 hole puncher to assure reproducible positioning of the holes on all films. Furthermore, for the 4 screws used, inserts were cut into the film. Care was taken to label and track the orientation of the films, as there is a known orientation dependency while scanning for all EBT films [63], requiring them to be scanned in landscape orientation only. As film dosimetry is very sensitive to dust and any other contamination, the films were only manually touched on the sides and by using gloves. Any exposure to light was minimized by storing the films in a black box and cutting them under dimmed light conditions, with having a set of three additional films, treated in the same manner as all others, which were not irradiated but used as reference for background determination.

5.3 Irradiation experiment protocol

5.3.1 Transmission experiment using the Lynx-detector

Before performing irradiation experiments with the phantom and the film detector in the magnet, a transmission experiment was done to measure the deflection of the proton beam while traversing through the magnetic field. The main aim of this experiment is to validate that deflection will only be present in the x-y-plane, further called in-plane deflection, as expected for a magnetic field parallel to the z-axis. Out-of-plane deflection, i.e. beam deflection along the z-axis would only be expected for large field components non-parallel to the z-axis.

This experiment used the same setup as the main experiment, having the collimators and the magnet in place (see Figure 5.3). The proton beam transmitting through the magnet's air-gap is measured using a Lynx detector (IBA Dosimetry, Schwarzenbruck, Germany)(see section 2.4.2). The Lynx detector acquires 2D beam profiles at a distance of 26 cm distally from the magnet. It offers a resolution of 0.5 mm in both y and z direction.
The whole energy range available at the experimental room was used, to acquire beam profiles for 70, 90, 110, 120, 140, 160, 180, 200, 210 and 225 MeV proton beams. To obtain beam deflections, the experiment was performed in a reference vs. in-magnet protocol, first acquiring the beam profiles being deflected by the magnet, followed by a second set of experiments, where only the magnet was moved out of the beam line, with the collimators and Lynx detector at the same position, enabling absolute difference determination.

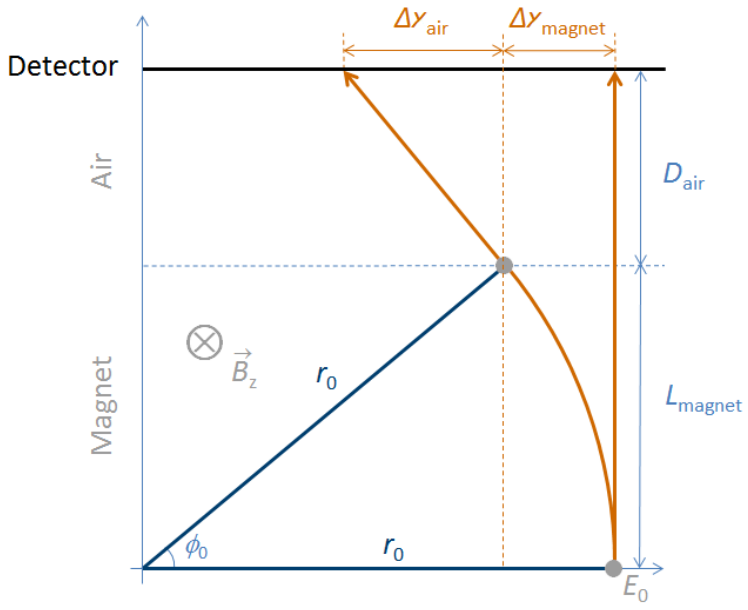

Figure 5.8: In-plane beam trajectory prediction: Beam deflection (orange line) on the Detector (black line) consists of two parts, Δx_{magnet} from the circular deflection due to the magnetic field of length L_{magnet} and Δx_{air} due to the distance D_{air} travelled under a constant angle ϕ_0.

From all measured beam profiles, the maximum beam profile intensity pixel was determined and used as y and z beam position. Absolute differences Δy and Δz were extracted. For the in-plane deflection, a simple analytical model was used to predict beam deflection at the Lynx detector. The model used the following assumptions: firstly, no energy loss in air is considered, thus having a constant proton energy. Secondly, relativistic effects were ignored. Thirdly, the magnetic field was

approximated by a rectangular shape matching the magnet's air gap dimensions, only featuring a transverse, i.e. B_z component uniform over the whole volume. The field value is chosen such that its integral matches the integral over both central B_z scans along the x- and y-axis, performed in Part I (rectangular field approximation). Fourthly, the gyroradius r_0 was approximated by the following formula [8]

$$r_0 \approx 14.4 \frac{\sqrt{E_0}}{B_z} \tag{5.1}$$

with r_0 in units of cm, B_z in Tesla and E_0 in MeV.

The total beam deflection Δy can be expressed as a sum of Δy_{magnet} and Δy_{air} (Figure 5.8). Firstly, Δy_{magnet} results from the angular deflection, with constant gyroradius r_0, within the magnetic field of length L_{magnet} of the magnet. Secondly, Δy_{air} is introduced by the beam leaving the magnetic field under an angle ϕ_0 relative to the initial beam axis, travelling a distance D_{air}, which is the distance from the distal end of the magnet to the Detector plane. The sum of the deflections can be expressed as follows

$$\begin{aligned} \Delta y &= \Delta y_{\text{magnet}} + \Delta y_{\text{air}} \\ &= r_0 - \sqrt{r_0^2 - L_{\text{magnet}}^2} + \frac{D_{\text{air}} \cdot L_{\text{magnet}}}{\sqrt{r_0^2 - L_{\text{magnet}}^2}} \\ &= r_0 - \frac{r_0^2 - L_{\text{magnet}}^2 + D_{\text{air}} \cdot L_{\text{magnet}}}{\sqrt{r_0^2 - L_{\text{magnet}}^2}}. \end{aligned} \tag{5.2}$$

Note that again r_0 is expressed as in equation (5.1) and therefore Δy becomes a function of proton energy.

5.3.2 Dose response experiment

For the main film irradiation experiment, the dose range applied to the film had to be estimated, choosing an optimum between high doses, providing a better signal-to-noise ratio (SNR), and staying within the linear film response range. The calibration of net optical density (netOD) to Dose is optimized for a dose range of $0.1-10\,\text{Gy}$ [64]. However, as the used calibration was performed for a different batch of EBT3 films, it can only be used for relative dosimetry, as batch-to-batch variations range up to 15 % in dose [63]. For relative dosimetry however, it is most important, that dose response is linear to fluence at constant stopping power, i.e. same experiment conditions and depth. Therefore a dose response experiment was performed, to investigate dose response as a function of fluence.
Film profile measurements were performed in a small phantom (3×3 cm^2 area) consisting of two blocks of PMMA of 1.6 cm thickness each. The small phantom was positioned at the laser isocenter. The set of 10 mm diameter collimators was used identical as in the main experiment. Small film pieces were inserted between the slabs, such that the film plane was normal to the beam axis. This enabled beam profile measurements. For a constant energy of 180 MeV and a beam current $I_C = 0.185\,\text{nA}$, film samples were irradiated with varying Monitor Units (MU), i.e. ionisation chamber current integrated over time, to acquire a dose response curve, in the range of 1 to 30 Gy. Note, that here MU is used as a measure of fluence integrated over the ionization chamber area, as the current in the ionisation chamber at the nozzle is, in a statistical sense, proportional to the number of protons traversing the chamber i.e. fluence rate, which integrated over time, gives the MUs, thus being proportional to a total proton number traversing the ionization chamber. MU is therefore a measure of units nAs,

which is charge, however it is often reported unitless.
As the films are at a depth of 1.6 cm of PMMA only, for a 180 MeV proton beam, the dose measured will be in the entrance, i.e. plateau of the depth-dose curve before the Bragg peak (BP), thus no LET effect had to be considered for this experiment.
Films were handled and evaluated as described in section 5.4. Dose on the film was then extracted using the two different methods. Firstly, as the pencil beam had a circular shape, the first method segmented the scanned image into two regions, the circular beam and the environment and automatically detected the outer circle (using the Hough-transform, see section 5.4). A region of interest (ROI) was defined by 10×10 pixels around the circle's centre. The mean dose within this ROI is used. This method is called 'circle method' in the following.
A second method was developed, as beam profiles were a bit asymmetrical and thus the circle methods was suspected to underestimate the dose on the film, as the maximum might not be in the centre. The method, in the following called the 'filtered max method' therefore aims to detect the maximum of the profile. Maximum detection was performed by filtering the dose image with a median filter of (5×5) pixels first, to reduce noise, and a Gaussian 5×5 filter second, reducing individual features and thereby increasing the robustness of detecting a single maxima. Again, a 10×10 pixel ROI was defined around the maxima position and the mean dose within this ROI on the raw unfiltered dose data was used.

5.3.3 Main experiment protocol

Figure 5.3 already presented the complete experimental setup used for the irradiation experiments. Here all measures are given. The two 10 mm diameter collimators are positioned at 168 cm downstream of the beam snout, while their lateral positions were first set to match the room laser and then shifted 2.5 mm towards the right, as looking beams-eye-view (BEV), compare section 5.2.2. This was done, to account for the known beam-angle relative to the laser system of $\approx 0.1^{\circ}$ laterally, thus collimating the most symmetrical, central part of the beam profile.
In the next step the magnet's table was positioned such that the magnet's axes were aligned with the laser system, and the isocenters of both the magnet's air gap and the room lasers overlap, resulting in the magnet being 202 cm downstream form the beam snout. The phantom was then mounted onto the phantom holder and adjusted to match the magnets extent, i.e. the edges of the phantom were positioned to match the magnet's edges. The height is given by the phantom holder and therefore reproducible and fixed. Using a bracket which is clamped onto the tabletop, the holder's position is also reproducibly set and fixed by another clamp. For reference measurements the magnets table was moved to get the magnet out of the beam line (see Figure 5.7). The phantom and holder were positioned in the same manner as before, with the difference that the laser alignment was done directly on the phantom and not indirect by the magnet.

Definition of irradiation parameters For each irradiation experiment the phantom had to be moved out of the magnet's air gap, opened and unscrewed to insert a new film between the slabs. As was already pointed out, film handling was always performed while wearing gloves, to prevent the films from any contamination.
The beam in the experimental room at UPTD is controlled from a separate room, the research control room (RCR). Beam parameters to be set are the requested energy, ionisation chamber current I_C at the nozzle (snout) and the Monitor Units (MU) requested. For phantom irradiation experiments a set

Energy [MeV]	80	100	120	140	160	180
applied MU [nAs]	4.27	3.96	3.68	3.10	2.95	2.43

Table 5.1: Monitor Units for Experiment 1 for each beam energy.

of 6 beam energies was chosen, covering a range from 80 MeV to 180 MeV by steps of 20 MeV.
The main experiment, measuring 2D dose distributions, both within the magnetic field as well as without, was performed twice with two different sets of dose levels on the films. In **Experiment 1**, the dose in the entrance (first few cm of depth) was adjusted to about 5 Gy for each energy. MU to dose estimation was gained from profile measurements at 1 cm depth in PMMA, for each of the specified energies. MU applied in Experiment 1 are reported in Table 5.1. For **Experiment 2**, care was taken to adjust the MU levels, such that no doses above 10 Gy were delivered to the films, to assure staying in the optimized dose range of of 0.1−10 Gy of the netOD to dose calibration [64]. Expecting highest doses in the BP, the energy dependent entrance to BP dose ratio was determined from Experiment 1. Thus having a translation from BP to entrance dose and entrance dose to MU, Monitor Units were adjusted. At the same time care was taken to avoid dose levels below 1 Gy, as those would result in a low SNR and therefore complicate later data processing. Table 5.2 lists BP and entrance Dose per MU, resulting ratio: BP dose over entrance dose and applied MU. Derived from the first two lines and the applied MU, also expected doses at the entrance and BP are listed.

Energy [MeV]	80	100	120	140	160	180
Bragg-Peak (BP) dose per MU [Gy/nAs]	4.47	4.55	5.59	4.62	4.15	2.96
entrance dose per MU [Gy/nAs]	0.95	1.02	1.14	1.35	1.41	1.73
entrance over BP dose ratio	4.7	4.4	4.9	3.4	2.9	1.7
applied MU [nAs]	2.25	2.15	1.78	1.45	1.40	1.18
expected entrance dose [Gy]	2.14	2.20	2.02	1.95	1.96	2.04
expected BP dose [Gy]	10.0	9.77	9.92	6.68	5.79	3.49

Table 5.2: Setup parameters for Experiment 2.

5.4 Film handeling and evaluation

After irradiation, films were again stored in a black box to minimize light expose. According to e.g. [65] there is a significant post-irradiation darkening in EBT3 films, which require at least 24 h between irradiation and scanning. All films were therefore scanned at least 48 h post-irradiation using an EPSON Expression 10000XL (Epson America, Long Beach, CA) flatbed scanner. Scanning was done using a template to assure a reproducible positioning of the film on the scanner surface, minimizing scanner inhomogeneity effects and lateral scan artefacts [66–69]. All films were scanned in landscape orientation, using transmission mode of the scanner, 24-bit RGB colour mode and a resolution of 300 dpi and stored to .tiff files. Scanned images were analysed using the Python programming language (Python Software Foundation). A number of steps, described in detail in the following sections were then performed: firstly, pin-holes were automatically detected on the scanned images and rotational

and translational position correction was applied. Secondly, pixel values of the red channel were transformed to netOD which is converted to dose. Thirdly, both percentage integrated depth dose curves (PDD) and beam trajectories were obtained from the 2D dose distributions, enabling calculation of lateral beam deflection and longitudinal retraction for each beam energy.

Orientation correction by pin-detection Having scanned images of the EBT3 films, pixels were in a coordinate system representing the scanner rather then the phantom. However, for further data analysis spatial information was required in the phantom's coordinate system. Therefore scanned images were corrected in both rotation and absolute position to match the phantom axis. As a means to co-register images to the phantom system the two registration pins were used as their absolute position on the phantom and relative angle is well defined. The Python OpenCV (cv2) package lends itself for most of the required operations. Greyscale images were generated from the scanned images, on which using the HoughCircles function based on the Hough-Transformation [70, 71], circles were detected on the scan images. Parameters of the HoughCircles function: minimum circle distance, as well as minimum and maximum radius were adapted to identify exactly two circles on the images, the two registration pin-holes. The relative angle between the two holes was calculated and the image was subsequently rotated around one of the hole's centre, such that this angle was optimized to match the 45° angle defined by the design of the phantom. The image was then shifted to align the film with the phantom edges. These two operations, rotation and translation define a coordinate system transformation which is applied to the initial 24-bit RGB images. Further, due to the 1° tilt angle of the film plane, 2D dose distributions are obtained by defining a coordinate system (x',y') along the film plane, scaling pixels with the image resolution of 300 dpi. This coordinate system is then rotated by $\alpha = 1^\circ$ into the magnet's (x,y) system via $x = \cos(\alpha)x'$ and $y = y'$.

Conversion to dose The orientation-corrected images were used for further evaluation, transforming the image intensity to dose. As described in chapter 2.4.1 for the dose range of 0.1 to 10 Gy the RGB's red image channel has the strongest dose-dependent signal and was therefore used for the signal to dose conversion. Background intensity was determined from the reference films. Three unexposed films were scanned along with the films that had been irradiated. A central region of (100×400) pixels was chosen from the reference images and the mean intensity value was determined and used as I_0. Using equation (2.19) pixel intensity was transferred into netOD, which was then converted to dose using equation (2.20) where the values $k_1 = 8.36$, $k_2 = 10.71$ and $k_3 = 1.84$ were taken from a calibration performed by E. Beyreuther in 2015 at Oncoray, using EBT3 films of a different batch.

Calculation of integrated depth dose curves and beam trajectories From the orientation correction and conversion to dose, 2D dose distributions of the proton beams in the phantom were obtained. From these, a number of properties were extracted. Firstly, PDD were calculated together with central beam trajectories. Secondly, using the PDD and trajectories, lateral beam deflections and longitudinal retractions were calculated. For the extraction of beam trajectories, for each depth $x = x'$ the lateral beam profile $D_{\mathrm{lat}}(x = x',y)$ was fitted using a Gaussian function. This yielded the maximum's position y_T as a function of depth x, which was defined as the trajectory $y_T(x)$. To obtain a PDD comparable to measurements performed with a large ionisation chamber, which integrates dose deposited in the whole chamber volume, from the 2D dose distribution, a radial dose integration has to be performed.

The PDD(x) is therefore defined as:

$$PDD(x) = \int_0^{2\pi} \int_0^{r} D'_{\mathrm{lat}}(x,y') \cdot y' dy' d\phi \tag{5.3}$$

where $D'_{\mathrm{lat}}(x,y') = D_{\mathrm{lat}}(x,y-y_{\mathrm{T}}(x))$ is the lateral beam profile, with a y-axis shift, such that $y'(y_{\mathrm{T}}) = 0$ and r is the integration radius. Note that exact radial integration only uses the positive branch of $D'_{\mathrm{lat}}(x,y')$. However, to account for potential asymmetry in beam profiles, the integral was changed such that the integration is performed form $-r$ to r over half the angle ϕ, which is mathematically identical to taking the mean over the positive and negative branch of $D'_{\mathrm{lat}}(x,y')$.
Choosing the right value of integration radius r was subject to optimization and found to be sufficiently larger at $r = 150\,\mathrm{px} = 12.7\,\mathrm{mm}$. It thus extends over more then 3σ over the fitted Gauss function. At the same time increasing r further would have led to increased noise in the PDD, as due to the radial integation, a low noise signal far away from the integration centre leads to significant change in the integral, as it is weighted with the distance. The resulting PDD(x) was then used both for comparison between reference and in-magnet beams and further to extract the proton beam range, which was defined by the R_{80} parameter. R_{80} is the distal depth at which 80% of the maximum dose is deposited (see chapter 2.1.1). For the comparison of reference and in-magnet beams, the range difference, i.e. longitudinal retraction, ΔR_{80} was determined. The lateral BP deflection y_{def} was obtained from the deflected trajectory as $y_{\mathrm{def}} = y_{\mathrm{T}}(R_{80})$.

6 Results and Discussion

6.1 Lynx transmission experiment

From the transmission experiment using the Lynx detector, both the in-plane and out-of-plane deflections for all energies are presented in Figure 6.1. The left plot presents the in-plane deflection along the y-axis. Additionally, the expected deflection according to equation (5.2), using a distance $D_{air} = 26.0\,\text{cm}$ between magnet and detector, $B_z = 0.95\,\text{T}$ and $L_{\text{magnet}} = 20.0\,\text{cm}$, is plotted for comparison. The accordance between measured data points and analytical curve is better than the resolution of the Lynx detector (0.5mm). For the out-of-plane direction, i.e. the z-axis, no deflection was observed for all energies above 120 MeV. The deviations for 70, 90 and 110 MeV are 0.5 mm each. It is important to realise here that only the maximum position of the beam profiles was determined and used as approximation for the beam profiles centre. However, especially for lower energies, having a broadened beam profile by air-scattering, an uncertainty in central beam spot position to dose maximum of 1.0 mm has to be expected, as the profiles are not perfectly symmetric. It is therefore assumed that the deviations are within the uncertainties of the evaluation and no net deflection effect out-of-plane is found.

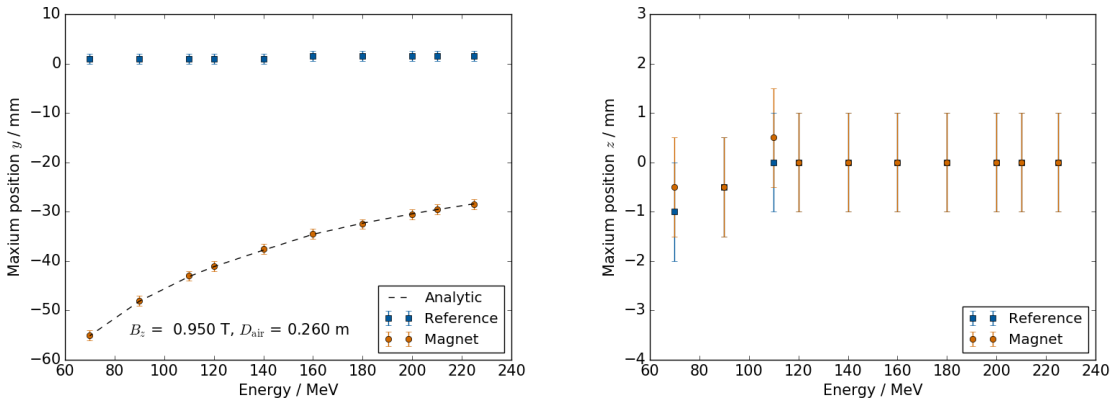

a) b)

Figure 6.1: Maximum positions of beam profiles on the Lynx detector for both y (a) and z (b) direction as a function of beam energy.

These results presented here allow for two main conclusions. Firstly, the magnetic field only leads to in-plane deflection. This justifies the decision to do 2D in-plane dosimetry for beam deflection determination, as was done in the main experiment. Secondly, the deflection is predictable by a simple model presented above, which among others (see chapter 5.3.1) assumes the dominant magnetic field component to be parallel to the z-axis only, thus suggesting no measurable effect introduced by the minor field components.

6.2 Dose response curve of EBT3 film

The dose response curve, presenting mean doses on EBT3 film in the 10×10 pixel ROI as determined by the 'circle method' and filtered max method' (see chapter 5.3.2) are presented in Figure 6.2. A linear response of dose on film with MU can be seen in the range between 0.5 to about 8 MU. This corresponds to a measured dose on film of 2 to 16 Gy. For higher MU applied, the curve saturates at a dose on film of about 19 Gy. For better visualization of this effect, a linear regression is plotted over the first 10 data points of the 'filtered max method'. Note that the noise, visible by the standard deviation in the ROI, plotted as dose error, increases with increasing MU applied for both methods. Further, a systematically lower response is detected with the 'circle method' as compared to the 'filtered max method', which is caused by the fact that beam profiles are not perfectly symmetrical and thus the circle method underestimates the maximum dose. However this effect is small and does not change the conclusion that can be drawn from the plot.
This leads to the conclusion that relative dosimetry, which requires a linear dose response to not distort the relative dose distribution can be performed up to 16 Gy. For higher doses however a strong saturation leads to under-response in the dose measured on film. This has to be considered especially for Experiment 1, featuring high dose levels.

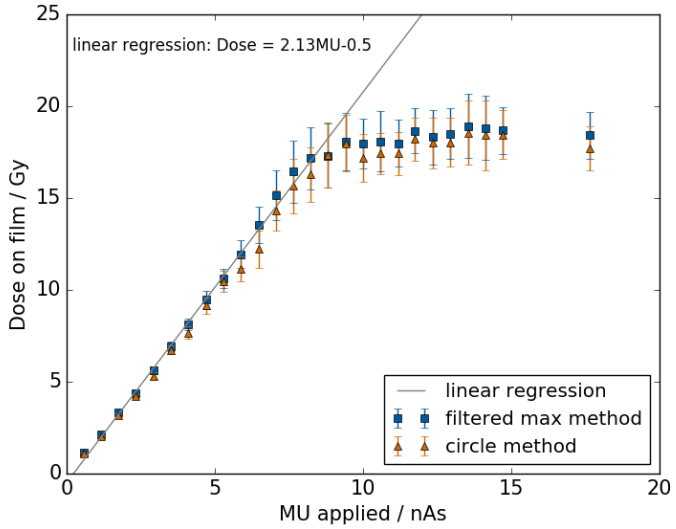

Figure 6.2: Dose response measured on EBT3 film as a function of applied MU, for a 180 MeV proton beam, at 16 mm depth in PMMA. Errorbars are the standard deviation within the defined ROIs.

6.3 EBT3 film scans

The film-phantom irradiation experiments result in EBT3 film-scans yielding the 2D distribution of the proton beam being stopped in the phantom. As an example, Figure 6.3 depicts the scanned image of a 140 MeV proton beam, with no magnetic field, taken from Experiment 2. It is clearly visible that the proton beam has a finite range with an area of increased film darkening directly at the end of range, while before, film darkening on the pencil-beam is nearly constant. The registration pin-holes are also clearly visible. Note that the cut-outs represent the positions of the screws used to press phantom plates together. Black lines at the lower and right edge of the image, are from

the template used during the scanning procedure. On the lower left corner, a slight misalignment of the film to the scanner template is visible, indicating the necessity of the used rotation correcting, described in chapter 5.4. For all films, correction angles were between -0.4° and 0.8°, with a mean absolute correction angle of 0.4°. Resulting angle uncertainty by angle calculation after rotation was determined to be smaller than 0.1°.

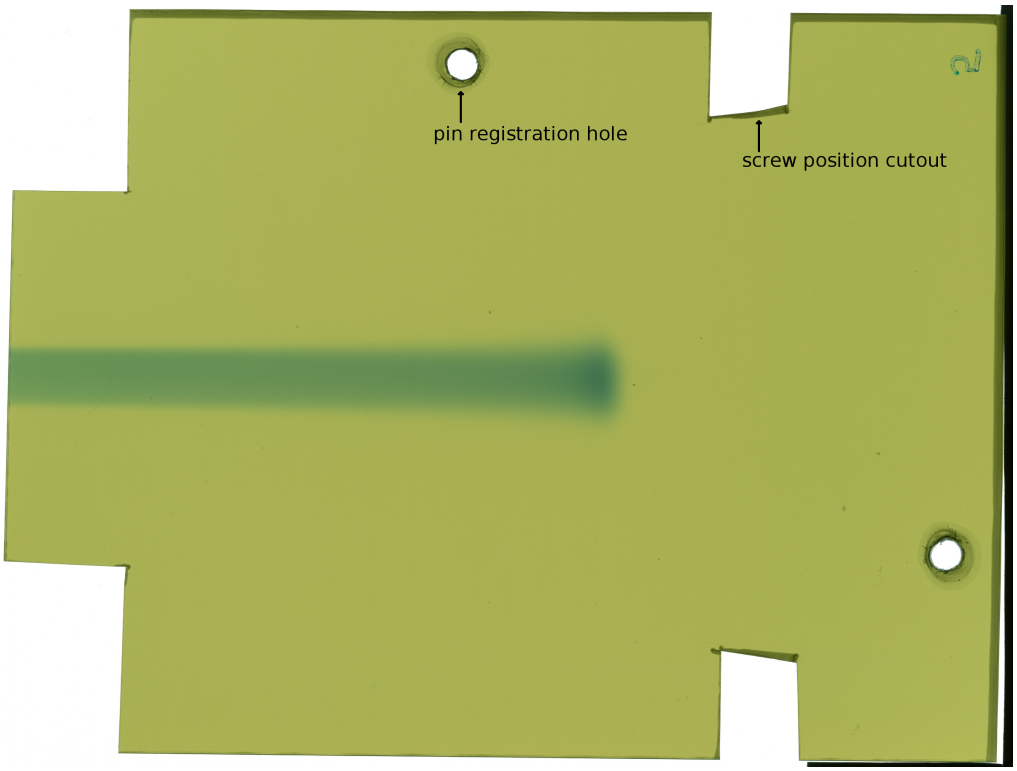

Figure 6.3: Scan of an EBT3 film cut to match phantom design, after irradiation with a 140 MeV proton beam without magnetic field, from Experiment 2.

6.4 2D dose distributions

Figures 6.4 and 6.5 present the 2D dose distributions calculated from the film scans of Experiment 1 and 2, respectively. For comparison, both reference and in-magnet measurements are depicted in one plot. All data are rotation corrected, filtered using a (5×5) pixel median filter and normalized to the maximum. The first (left most) 30 pixel were cut out, as along the film edges dose overestimation due to separation of the film layers (caused by film cutting) and therefore increased optical density corrupt the dose data in those pixels, compare Figure 6.7. From top to bottom, beam energies increase from 80 MeV to 180 MeV. References, without magnetic field, are presented as filled contours in grey-scale, whereas in-magnet dose distributions are shown by contour lines of 10 % separation using a multicoloured representation. Note that the two colorbars in Figures 6.4 and 6.5 apply for all 6 sub-images.

The beams show an increasing range with increasing initial energy. The Bragg peak is clearly visible at the end-of-range, showing highest doses for all energies. Further, all beams in Experiment 2 show a slight asymmetry, indicating higher fluence on the right, as looking BEV, visible by contour lines being asymmetrical in respect to the central beam axis. This indicates a less optimal lateral collimator position in Experiment 2 as compared to Experiment 1.

As for the comparison of references to in-magnet beams, beam deflection towards the left, as looking BEV, for in-magnet beams is visible for all energies and both experiments, while the amount increases with initial energy. For the lowest energy beam of 80 MeV deflection is very minor (and difficult to see in the images), whereas for the highest energy, 180 MeV, the Bragg peak of the in-magnet beam is about one centimetre deflected compared to the reference beam. It is further visible that with higher initial energy and therefore increasing range, the maximum dose in the Bragg peak relative to the entrance dose gets smaller. This can be understood by scattering, as the fluence distribution gets broader for longer beam ranges, and therefore the dose per pixel in the Bragg peak decreases. In the plots, as they are normalized to the maximum, this is only notable indirectly, by extension of the contour lines further to the entrance region.
Maximum absolute doses on film D_{Max} are listed for both experiments, all energies and both reference (ref) and in-magnet (mag) beams in Table 6.1. Using the result from section 6.2 this indicates that for Experiment 1, for 80, 100 and 120 MeV proton beams, the maximum dose on film was above the 16 Gy limit and therefore film response in all pixels of higher dose is no longer linear, thus indicating a potential distortion in relative dose distributions for those cases.

Energy [MeV] Experiment	D_{Max} [Gy] 1 ref	D_{Max} [Gy] 1 mag	D_{Max} [Gy] 2 ref	D_{Max} [Gy] 2 mag
80	22.7	23.6	8.0	8.3
100	20.2	20.4	8.6	8.5
120	17.2	17.4	7.5	7.1
140	12.5	12.7	5.6	5.3
160	11.2	10.9	5.3	4.7
180	7.8	7.2	3.9	3.3

Table 6.1: Maximum Bragg peak doses in both Experiment 1 and 2, for beams under the influence of the magnetic field (mag) and references (ref).

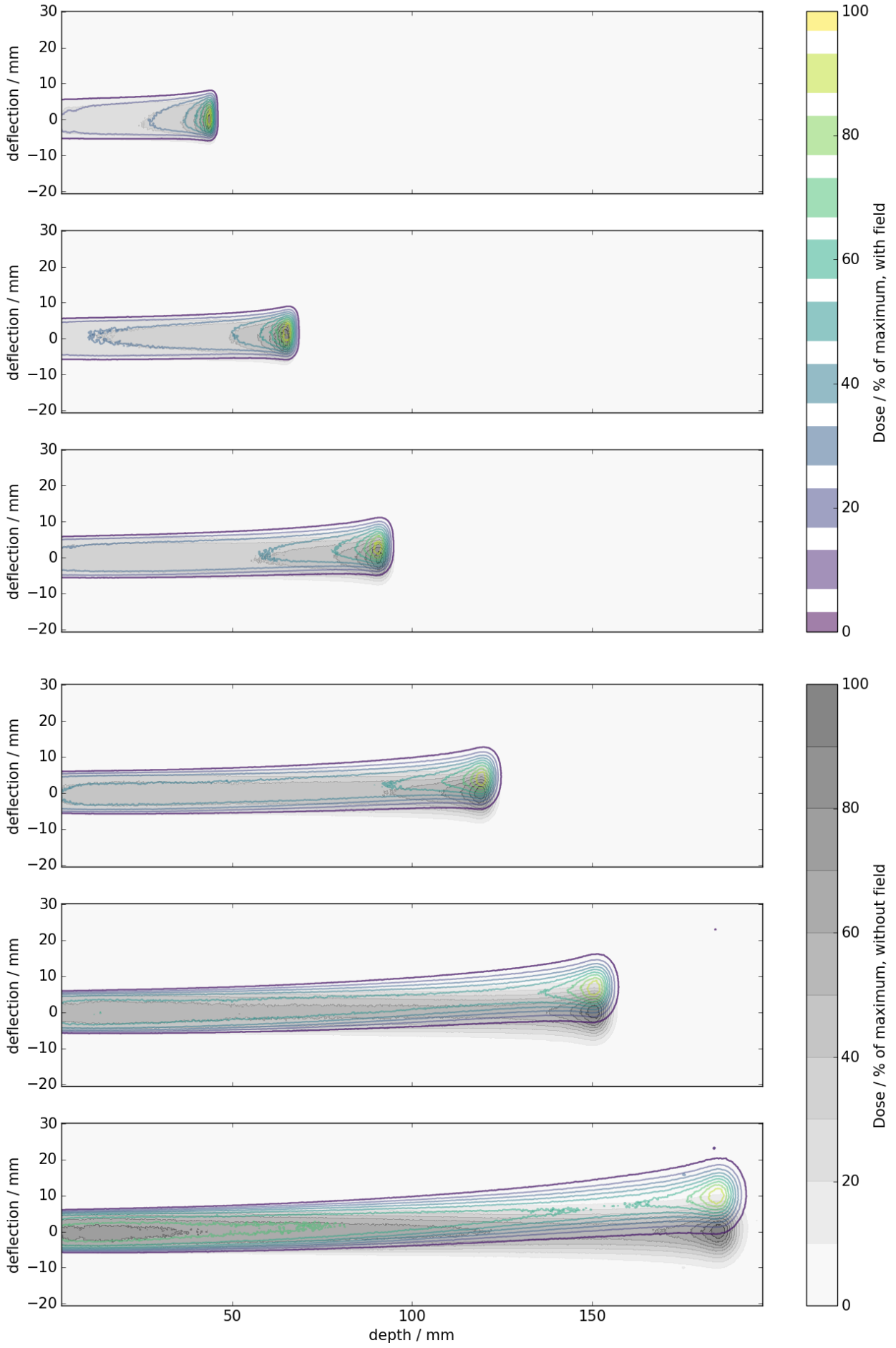

Figure 6.4: Experiment 1, from top to bottom: 2D relative dose distributions, of 80, 100, 120, 140, 160 and 180 MeV proton beams on the film dosimeter, with (coloured) and without (grey) magnetic field. Both colorbars apply for all 6 images.

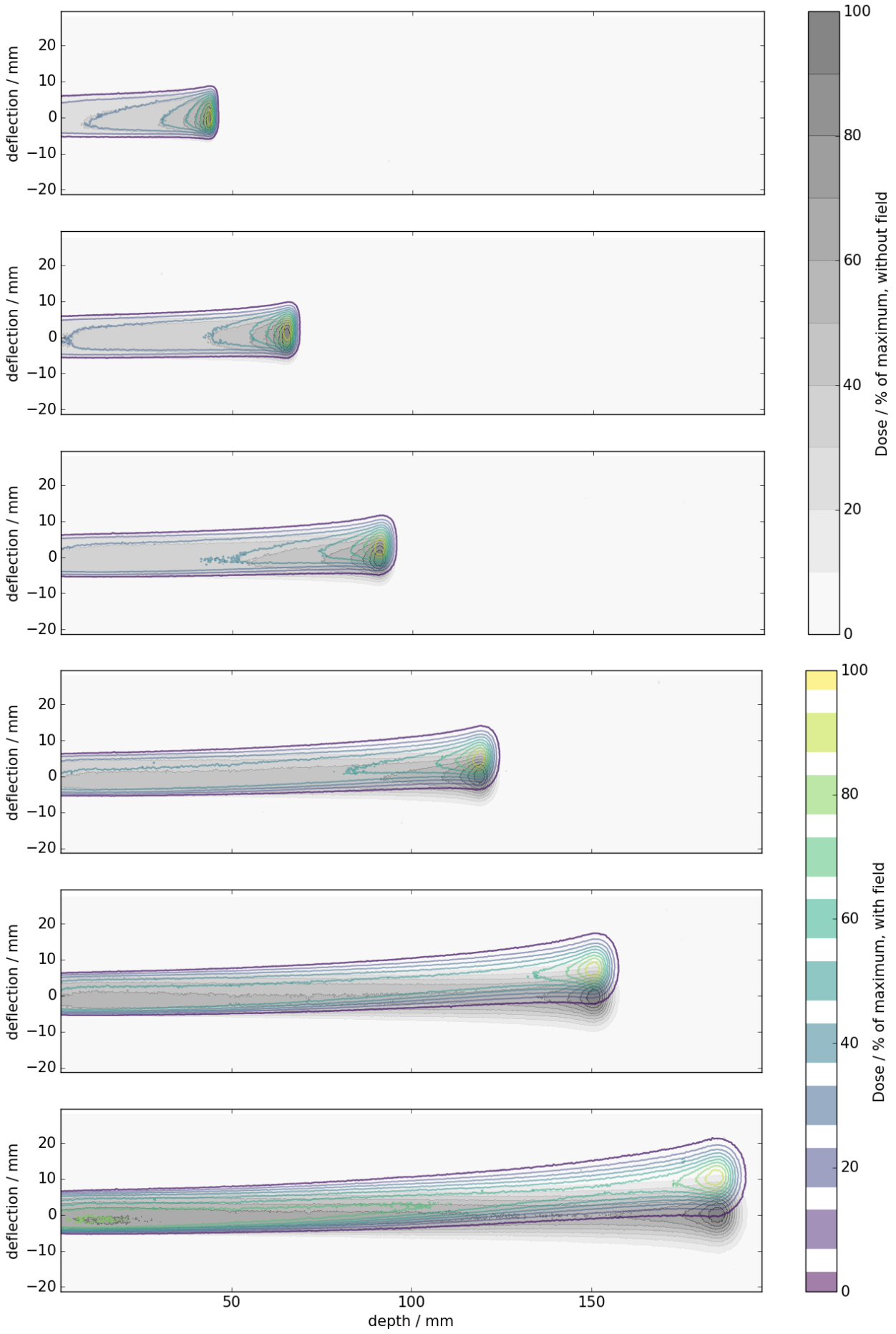

Figure 6.5: Experiment 2, from top to bottom: 2D relative dose distributions, of 80, 100, 120, 140, 160 and 180 MeV proton beams on the film dosimeter, with (coloured) and without (grey) magnetic field. Both colorbars apply for all 6 images.

6.5 Depth dose curves

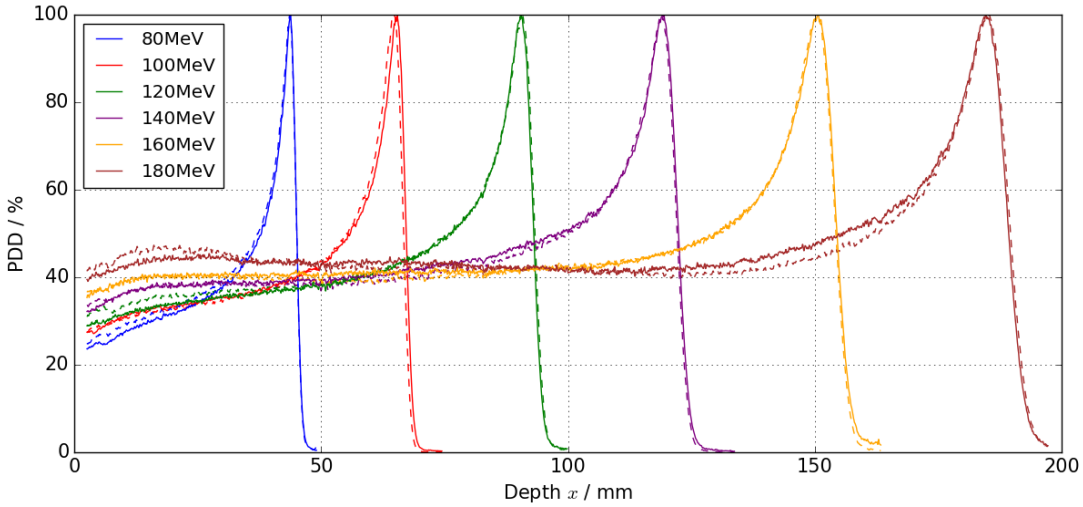

a) Experiment 1

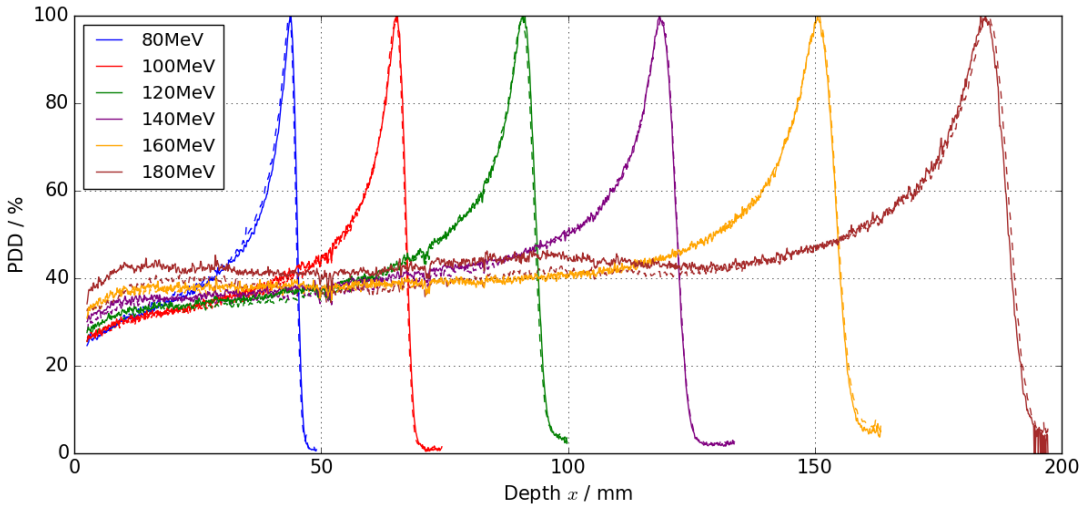

b) Experiment 2

Figure 6.6: Percentage depth dose curves for proton beams of all performed energies for Experiment 1 and 2, with (solid) and without (dashed) magnetic field.

From the 2D dose distributions both percentage depth dose curves (PDD) and beam trajectories are calculated, as described in section 5.4. Figure 6.6a presents all calculated PDD(x) of Experiment 1 and 2 (Figure 6.6b), where x is denoted as penetration depth. Reference PDD's are marked with dashed lines, whereas in-magnet PDD's are solid. Different colours represent initial beam energies, as given in the legend. All percentage depth dose curves show a characteristic behaviour, with a low, initial energy dependent, sloped plateau at about 40% of the maximum and a peak at the end of range, with a sharp distal drop-off. Note that with increasing energy and therefore range, due to range straggling the peak becomes both wider and the distal fall-off gets less steep. A further feature visible in all curves is a weak build-up in the first one or two centimetres of depth.

Comparing reference to in-magnet depth dose curves the slopes are very similar, with no difference in range visible in the plots and deviations in the plateau of only a few percent. For both experiments,

deviations for the 180 MeV beams are largest. In Experiment 1 there is a higher PDD at a depth of about 150 mm for the in-magnet PDD, while the reference PDD is higher in the entrance, at around 20 mm depth. For Experiment 2 also the 180 MeV PDDs show the largest deviation with the in-magnet PDD being about 5 % higher from the entrance till about 120 mm depth.
Further it is visible that due to the lower dose levels in Experiment 2, there is a larger noise on all PDD. This has its largest effect behind the distal fall-off, where PDDs are expected to be zero, but especially all PDDs from Experiment 2 remain at about 5 %. This effect is less pronounced in all PDDs of Experiment 1, while they are still non-zero behind the Bragg peak. Two effects are considered as potential sources of this. First, remaining air gaps in the phantom design would lead to individual protons having a larger range and thus depositing their dose behind the Bragg peak. Secondly, due to film and scanner inhomogeneities, the films all have a position dependent background, which is not completely removed by the background estimation. This leads to unexposed films having a 2D dose distribution that is non-zero, but in the order of 0.1 to 0.2 Gy, see Figure 6.7. This also varies from film to film.

Figure 6.8 compares reference (without magnetic field) PDDs obtained from the two different

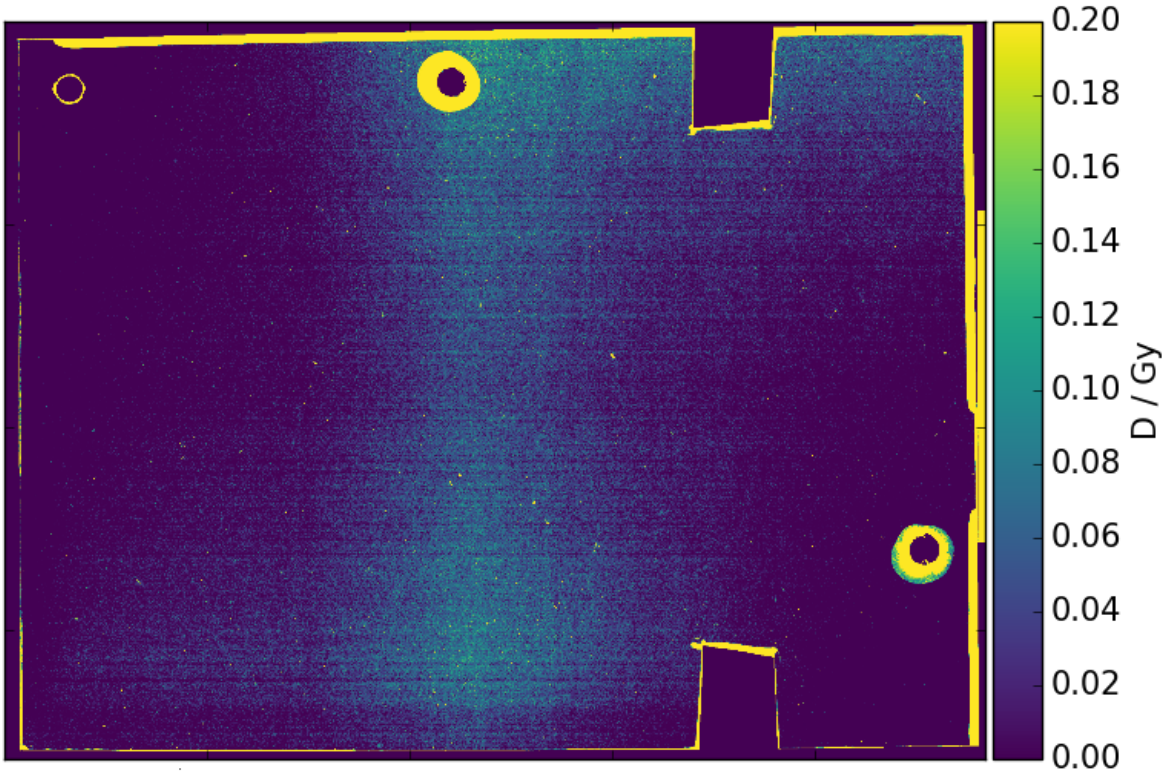

Figure 6.7: 2D dose distribution from an unexposed film, illustrating background to be position dependent. Along film cuts, due to film-layer separation, the dose is biased.

experiments. For better comparability all curves are normalized to the PDD at a depth of 20 mm. Ranges R_{80} are almost identical with deviations not visible in the images and again for Experiment 2 the larger non-zero offset behind the Bragg peak is visible for most energies. However there is no clear trend over all energies, regarding the shape of the PDD. The 80 MeV PDD for Experiment 1 features a lower Bragg peak. For 100 MeV the best agreement is found, whereas for all higher energies,

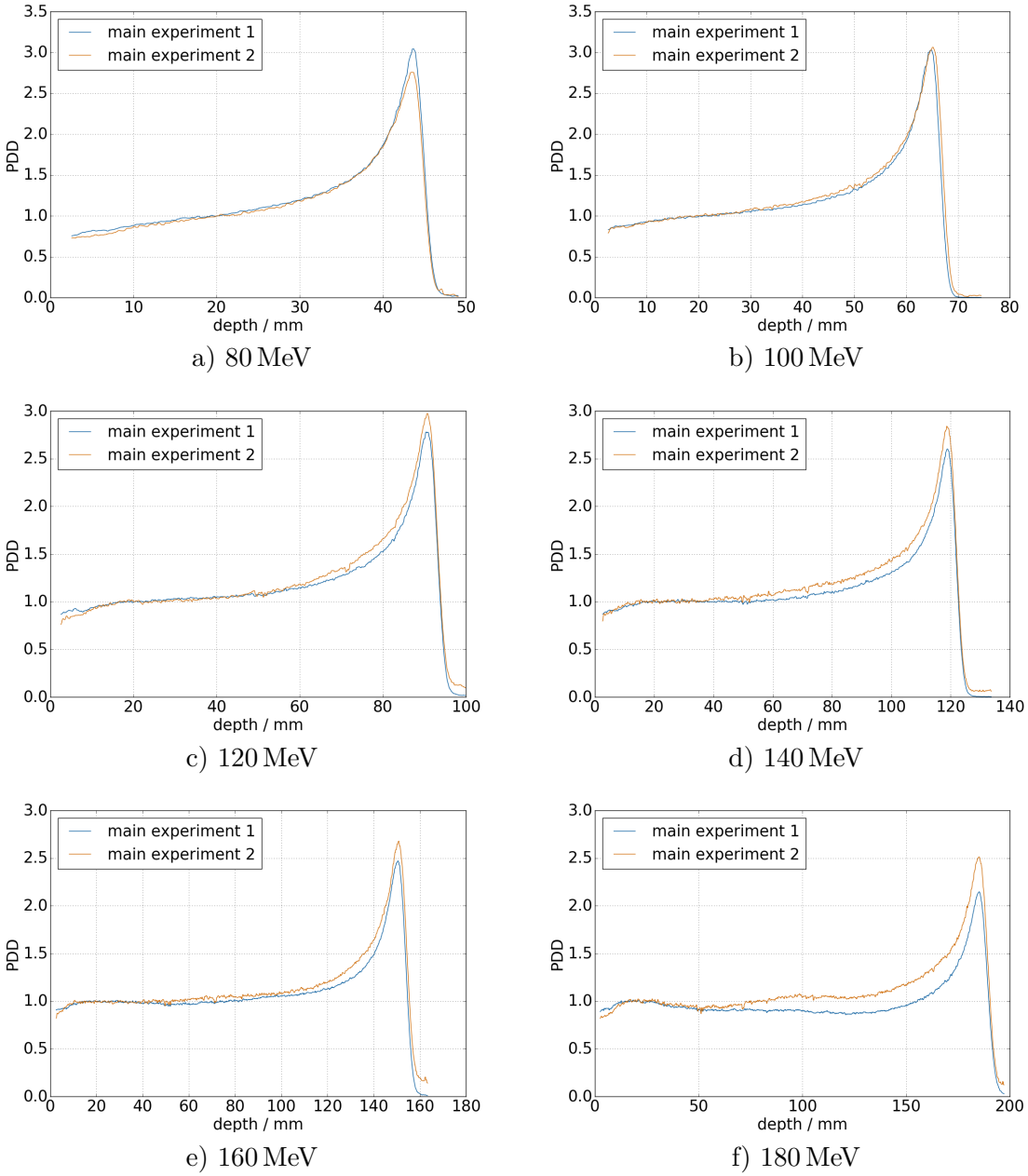

Figure 6.8: Comparison of reference (without field) PDD's for the two performed main experiments. All curves are normalized to PDD at 20 mm depth.

Experiment 2 PDDs are lower in the BP and before as compared to Experiment 1. This suggests a statistical variation, which might be caused by the films being slightly corrugated between the pins, due to minimal variations in hole positions. Furthermore film-to-film variations especially regarding the background doses are another likely source of deviations here.

Note that all data presented here are raw data, neither corrected for LET-dependence of EBT3 film response nor for the error in cylindrical integration due to the 1° tilt angle in the film plane. However, both effects would only be of interest in comparing the depth dose to curves acquired by e.g. ionization chamber measurements. The LET-effect is known to underestimate the PDD on EBT3 films in areas of increased LET, i.e. the Bragg peak, by 10 % to 25 % [29, 32] depending strongly on the LET value and thus on the used setup and the beam parameters. A number of publications [29, 32, 34] propose different correction approaches, which all present empirical corrections to depth dose by comparison

to either measured ionization chamber depth doses or simulated curves. However, none of these approaches can be generalized for different setups and beam parameters than the ones used within their respective studies. Also, within this work, neither a reference measurement was done nor precise LET values were extractable, debarring the application of a similar LET correction. Nevertheless, this should not distort the results obtained from 2D distribution or qualitative comparison of depth dose curves.

The cylindrical integration error can be estimated by assuming the beam of cylindrical shape with a diameter of 10 mm. The 1° tilt angle then leads to a shorter radius for all depth except the 100 mm depth (which is the tilt point of the film plane). The effect is a relative underestimation which is strongest in the entrance area and for the highest energy, 180 MeV also in the Bragg peak, of maximal 10 %. However, applying this correction does not change the comparative nature of the results and is therefore omitted. For reasons of completeness and to estimate the magnitude of this effect, a detailed derivation of the formulas and the resulting correction factor as a function of depth are given in Appendix A.

Extracted ranges R_{80} from the reference PDDs were plotted as a function of energy for both Experiment 1 and 2, see Figure 6.9. For comparison, continuous slowing down approximation (CSDA) range data from the PSTAR database [72] for PMMA, assuming a density $\rho_{\mathrm{PMMA}} = 1.19\,\mathrm{g\,cm^{-3}}$, is presented for the same energies. No differences are visible between any of the data set in the plot as all range differences were below 1.5 mm. For Experiment 2 a range-energy relation was fitted to the R_{80} data. The resulting power-law fit is added to Figure 6.9, with $\alpha = 0.0187$ and $p = 1.775$ ($r^2 > 0.999$).

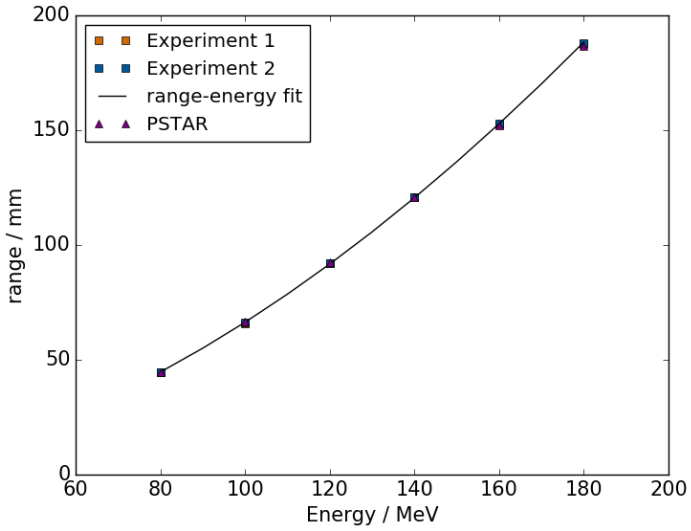

Figure 6.9: Proton beam ranges R_{80} from both Experiment 1 and 2 plotted as a function of initial energy. PSTAR CSDA range data for PMMA is presented for comparison as well as a range-energy fit on Experiment 2 data.

6.6 Beam trajectories and deflection

Central beam trajectories extracted from line-wise Gauss-fits from the 2D dose distributions are presented in Figure 6.10. Different beam energies are represented by various colours as given in the legend. Reference trajectories, depicted by dashed lines, show almost parallel alignment with

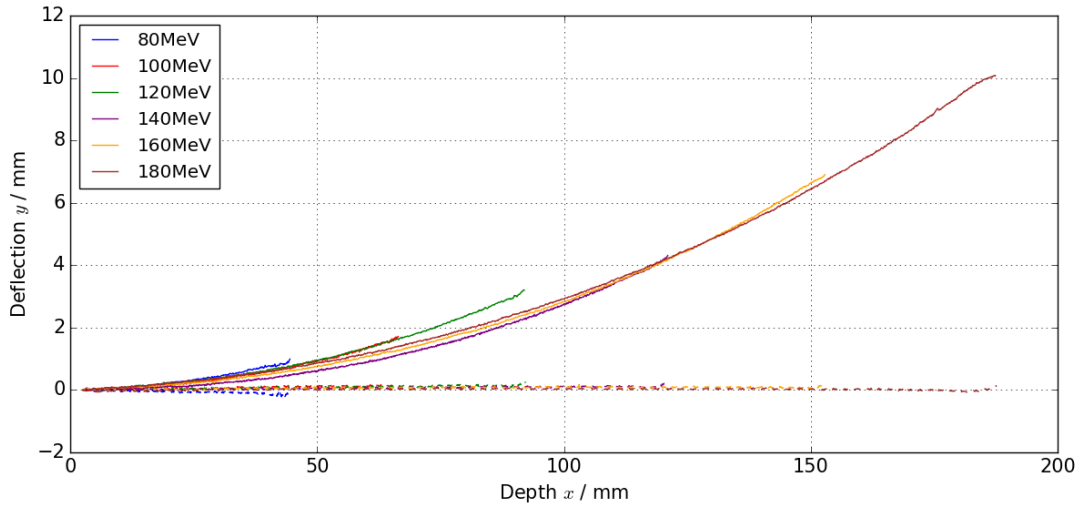

a) Experiment 1

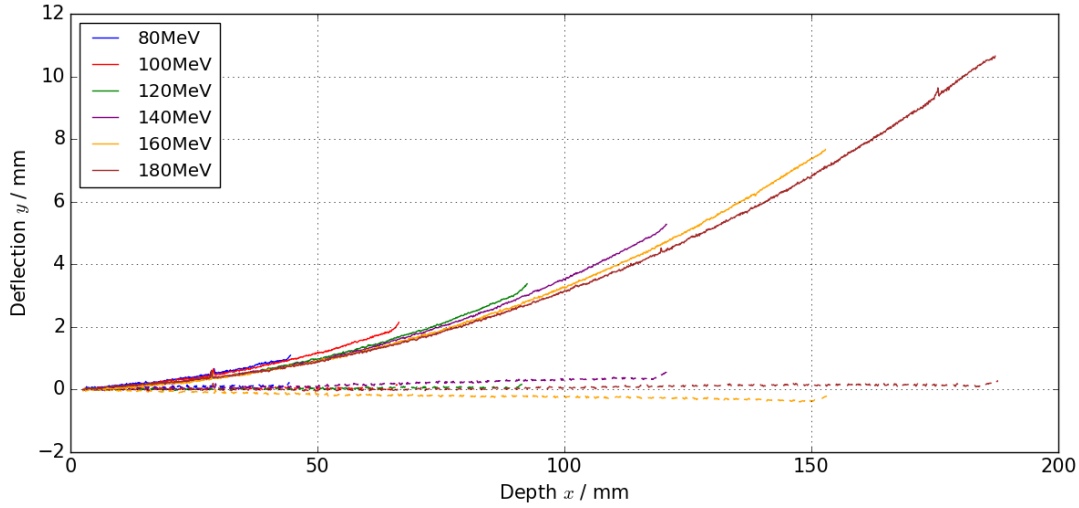

b) Experiment 2

Figure 6.10: Beam trajectories, with (solid) and without (dashed) magnetic field for all studied energies, for Experiment 1 and 2.

the depth axis, with lateral deflections in the range from -0.4 mm to 0.5 mm for Experiment 2 and -0.2 mm to 0.2 mm in Experiment 1. Reference trajectories for Experiment 1 appear to be parallel, whereas reference trajectories in Experiment 2 are divergent. This indicates a potential collimator misalignment in the second experiment, which was already observed in the 2D dose distributions. They were asymmetrical in the entrance, thus suggesting that collimators were slightly mispostioned towards positive y, i.e. the left as looking beams eye view, which results in the beam profiles maximum being on the opposite side, i.e. negative y, compare Figure 6.5.

No trend is visible in reference trajectory deflection over both experiments, suggesting deflections to be statistical, giving an estimate for the positioning uncertainty of the phantom and resulting deflecting uncertainty for the in-magnet trajectories. The latter are depicted in solid lines and show a deflection depending on initial proton energy. While initially the slopes are very similar, with increased slowing down of the protons and therefore lower remaining particle energy, the radius of gyration in the magnetic field decreases and therefore the trajectories bend stronger. This is visible

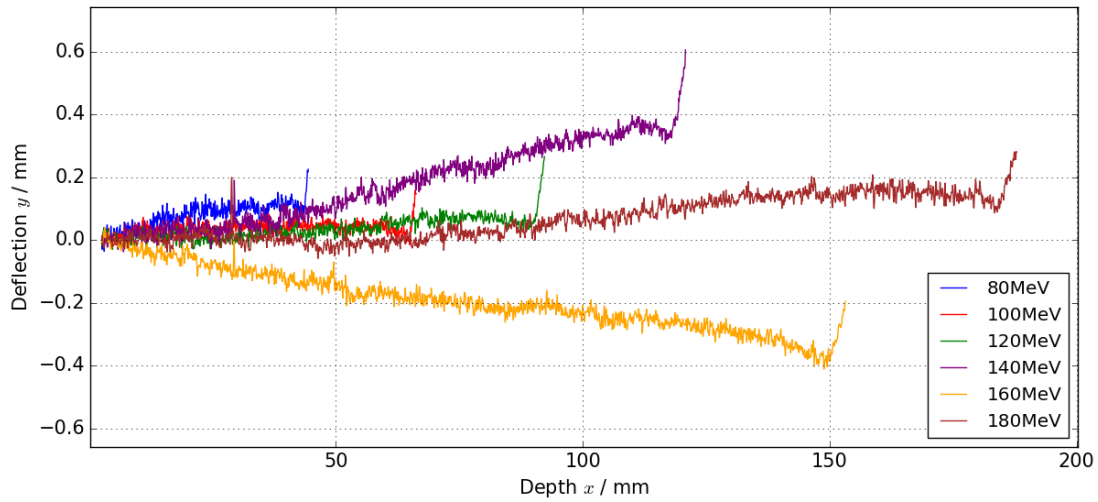

Figure 6.11: Reference trajectories from main experiment 2, featuring a 'hook' at the end of range.

especially for Experiment 2, where for all in-magnet deflected trajectories, deflection at a fixed depth is larger with lower initial energy as compared to higher initial energy. For Experiment 1 however this is not as clearly visible. Potentially phantom alignment within the magnet was less optimal, and therefore the trajectories have a slightly varying starting angle.

Trajectory 'hooks' A characteristic feature detected for all reference trajectories in both experiments is presented in Figure 6.11, showing Experiment 2 reference curves. At the end-of-range, all reference trajectories present a 'hook', i.e. a sudden increase in y_T, which extends about 3 mm in x- and 0.2 mm in y-direction. This effect is found over all energies used. Trajectories in Figure 6.11 are cut-off at R_{80}, the last 3 mm thus being exactly the Bragg peak, indicating that this 'hook' lies in the region of highest doses. For the in-magnet trajectories however, this 'hook' is less visible. While still being observable for the lower energy beams, it reduces gradually for higher energies.
The reason for this effect is unknown, however a few hypotheses should be discussed here. First, the visibility of the 'hook' in the in-magnet curves is biased by the curvature of the trajectories, which bend in the same direction as the 'hook'. Thus it is unclear whether the hook is not visible any longer or physically not present.
Reasons for the 'hook' could potentially be found in beam asymmetry. The trajectories are being fitted from lateral beam dose profiles using a Gaussian function. Suppose these profiles show a spatial asymmetry, the fitted y_T value is then biased towards one side. However, the deeper the beam penetrates, by scattering, this asymmetry is gradually reduces, while still being visible in the BP. However due to the sudden increase in dose level in the BP, the asymmetry could play a minor role and the fit thus being closer to the beams center. This would agree with the fact that beam profiles are asymmetric, with higher fluence towards negative y. However the 'hooks' are almost identical in Experiments 1 and 2 despite having much less asymmetric beam profiles in Experiment 1.
A different reason for the 'hooks' could be a potential spatial beam achromaticity. Suppose the y-axis energy spectrum is asymmetric showing higher energies for positive y and lower for negative y. Note that the energy width of the beams is only about 1.5 MeV, thus during the whole depth,

E_0 / MeV	$y_T(R_{80})$ / mm		ΔR_{80} / mm	
Experiment nr.	1	2	1	2
80	1.0 ± 0.4	1.1 ± 0.4	-0.1 ± 0.6	-0.2 ± 0.6
100	1.7 ± 0.4	2.1 ± 0.4	-0.5 ± 0.6	-0.3 ± 0.6
120	3.2 ± 0.5	3.4 ± 0.5	0.3 ± 0.6	-0.3 ± 0.6
140	4.3 ± 0.5	5.3 ± 0.5	-0.3 ± 0.6	0.1 ± 0.6
160	6.9 ± 0.6	7.7 ± 0.6	-0.2 ± 0.6	0.3 ± 0.6
180	10.1 ± 0.6	10.6 ± 0.6	0.3 ± 0.6	0.6 ± 0.6

Table 6.2: Lateral beam deflections $y_T(R_{80})$ and longitudinal retractions ΔR_{80} for all performed beam energies. Note that positive retraction values indicate higher range for the reference then deflected beams.

this achromaticity would not be visible. However, in the Bragg peak lower energy protons would stop fractions of mm earlier and thus shifting the dose profile at and behind the peak towards the side of higher energy protons. This hypothesis would also explain why the 'hook' is less visible for the in-magnet curves, as in a magnetic field, an energy separation inside the beam takes place, as described by [73]. This energy separation results from the fact that the gyroradius for protons of higher energy is larger, thus they are less deflected than lower energetic protons. This effect would therefore reduce the initial beam achromaticity with increasing range and could explain the absence of the 'hooks' for the in-magnet beams.
Therefore, the latter hypotheses seems more probable, as it is able to explain both reference and in-magnet trajectories. Nevertheless, none of these hypotheses could be verified so far and future experiments will be necessary to fully understand this effect.

Lateral deflection and longitudinal retraction Lateral beam deflection together with longitudinal retraction, as extracted from the trajectories and PDD's, are summarized for all proton energies in Table 6.2. The lateral deflection ranges from 1 mm to 10 mm for 80 MeV and 180 MeV beams, respectively. Longitudinal retraction, however, remains within the uncertainty limits of the measurement and therefore no effect can be reported.
The experimental uncertainties presented in Table 6.2 for both lateral deflection (y_T) and longitudinal retraction ΔR_{80} are a composition af various sources. Their determination is presented in detail in the next paragraph.

Uncertainty budget estimation A number of effects introduce uncertainties on the extracted values of both $y_T(R_{80})$ and ΔR_{80}. The following were considered and added up as presented in Table 6.3. The experimental setup is subject to systematic, both rotational and translational uncertainties in magnet and phantom positioning, as well as beam-to-laser axis alignment. The angle between beam and laser system axis is uncertain to 0.1°. The effect of this rotational uncertainty has been investigated by purposely rotating the scanned images and extracting resulting changes in range and deflection, which are energy dependent due to the different lengths of the trajectories.
Translational uncertainties in x direction, i.e. along the beam axis, are negligible as they do mainly change the distance the beam travels through air and the position of the registration pins on the

Sources of uncertainty	ΔR_{80} [mm]	$y_{\mathrm{T}}(R_{80})$ [mm]
statistical		
reproducibility analysis	0.5	0.3
systematic		
axis rotation	0.2	0.1 ... 0.4
R_{80} determination	0.2	< 0.05
trajectory 'hook'	< 0.01	0.2
Total	0.6	0.4 ... 0.6

Table 6.3: Sources of uncertainties in determination of range R_{80} and deflection $y_T(R_{80})$.

phantom is known to a precision of about 10 µm. Note that the dependency on precision in pin-holes on film, is minimized by rotation and translation of the films into the phantom's coordinate system and remaining deviations are covered in a repetition study that adds to the statistical uncertainties, see below.

Furthermore, uncertainties in y-direction, i.e. the deflection axis, are suppressed by setting the mean over the first 5 pixels of the trajectory y_{T} to be equal to 0, thus reducing deviations caused by signal noise. Another potential source for uncertainties in the y-direction is a potential fringe field, pre-phantom, beam deflection. However, as assessed in part I of this work the magnetic field is very low in the outside of the magnet's air-gap and by estimation using the analytic model presented for the transmission experiment in 5.3.1 the fringe field deflection was found negligible.

The remaining degree of translational freedom, z-axis alignment, mainly introduces uncertainties in the absolute height of the phantom within the magnet, which was reproducible to less than 0.5 mm as the phantom holder accurately defines the phantom- and thus film-height. The effect of a potential height difference of 0.5 mm on a 10 mm diameter beam is thus considered negligible.

The beam profiles were found to be not only spatially asymmetric in fluence, which has to be covered by optimizing collimator positions, but also a spatially dependent beam achromaticity is hypothesized to be a reason of the trajectory 'hook', as described above (compare Figure 6.11). The dimensions of this 'hook are about 3 mm in x and 0.2 mm in y direction for the reference trajectories and energy dependent for the in-magnet trajectories. The 'hook' effects the deflection determination with an uncertainty of its dimension in y direction, whereas its effect on range is considered negligible

In a next step, detector dependent uncertainties are investigated. Film and scanner non-uniformity, as well as film-to-film variability both lead to uncertainties in the PDDs. As relative dosimetry was performed, this should not change the trajectory. However for the range, and therefore also deflection, the R_{80} parameter from the PDD is used, which is affected. As visible in the PDDs, uncertainties introduced by the background were in the range of 5 % of the PDD. Therefore, uncertainties on R_{80} are investigated by detection of R_{75} and R_{85}. The effect on the range was found to be ± 0.2 mm, whereas this uncertainty only causes very minor change on deflection (below 0.05 mm). The film calibration, being performed for a different batch of EBT3 films, is subject to percentage absolute dose uncertainty in the order of 5 % [64].

The LET dependence of film response, which leads to a significant underestimation of the PDD in the BP could not yet be quantified, as the correction strategies proposed by different authors [32, 34] would

require a reference depth-dose measurement in PMMA using an ionisation chamber. However the LET dependent under-response in the Bragg peak is expected to lead to an underestimation in range and therefore also in beam deflection. Another unquantified source of uncertainty for Experiment 1 is the extension of doses in the BP over the linear range of the dose response curve (compare section 6.2).
To assess statistical uncertainties, for the highest energy (180 MeV) within Experiment 2 a repetition study was performed, irradiating three films with the identical dose. Detected differences in range and deflection lend for the determination of a statistical error.
Total uncertainties were determined by quadratic summation over all individual sources of uncertainties.

Part III

Summary and Conclusion

7 Summary and Conclusion

7.1 Summary

Part I - Magnetometry of a permanent dipole magnet The magnetic field of the C-shaped permanent dipole magnet was characterized by the means of both Hall-probe measurements and finite-element-modelling (FEM) simulations. The magnetic field of the magnet is symmetric with respect to the magnets main axis. The field in the air-gap can be described by two regions. Firstly, the plateau region in the inner of the gap, showing a relatively homogeneous B_z field, with a maximum field reading of 0.95 T. Secondly, the gradient area extending around the plateau region along the magnets rims, featuring a sharp fall-off, with field gradients of up to 40 mT/mm.
Hall-probe measurements of the main magnetic field component are very precise, with an uncertainty of below 5 mT. A line scan along the magnets longer axis (x-axis) could reproduce a reference measurement form the manufacturer. The FEM simulation results underestimate the main magnetic field component B_z in the gap by a mean of 10 mT in the plateau region, which is above measurement uncertainties (5mT). In the gradient region larger deviations are found, which are caused by axis misalignments of the measurement system relative to the magnet. Measurement of the small components is strongly affected by rotational uncertainties, leading to deviations in the same range as the field readings. However, it was shown that probe readjustment can reduce this effect. Vector field deviations between measurement and simulations amount to a mean of 20 mT in the plateau. The underestimation of the FEM simulation could be caused by the simulation input values, mainly the remanent field strength of the $Nd_2Fe_{14}B$ magnets which is given by the manufacturer at $B_R = 1.37$ T, but no uncertainty is known. Further, the exact material composition of the iron yoke is unknown. Thus, the B(H) response curve can only be guessed, using is a typical curve for soft iron, taken from the COMSOL material library, again without any means to assess uncertainties. However, the result known to best precision is the B_z field. Its difference between measurement and simulation amonts to 10 mT or 1 %, which is considered negligible for the desired use of the results, as input parameter for a future Monte-Carlo simulation of the beam deflection in the setup developed in part II. The effect on deflection is linear with the magnetic field, thus relative uncertainties will propagate. This was verified by a deflection difference estimation using the RAMDIM model, and resulted in a maximal 0.1 mm or 1 % difference in lateral deflection of 12.7 mm for a 180 MeV beam in water. This difference is considered negligible. However if better precision would be required for a future experiment, the FEM simulation parameters named above could be further adapted, to match the Hall-probe measurements.

Part II - experimental setup and irradiation experiments An experimental setup for performing proton pencil beam irradiation experiments under the influence of a magnetic field within a tissue-equivalent phantom has been realised. The setup consists of a number of components which were adapted to the given purpose. Despite the need for several rounds of optimization, the final setup is capable of performing the desired experiments, to investigate magnetic field caused dose effects of proton pencil beams with variing energy in a clinically relevant range.

A series of experiments was performed. Firstly, transmission experiments proofed that only in-plane deflection is measurable for proton beams traversing the magnetic field of the used permanent dipole magnet. Also, these deflections are predictable by a simple analytic model, despite its assumptions. Out-of-plane deflections remain within measurement uncertainty, suggesting no such effect. This result justifies the decision to perform high resolution 2D dose distribution experiments in the plane of deflection.
The dose response range of the EBT3 film detector was tested and a linear dose response was found for doses between 1 Gy and 16 Gy with a saturation behaviour for higher doses, thus distorting relative dosimetry results in higher dose ranges. Future experiments should thus be planned within this range.
In two main experiments, proton beam deflection by the magnetic field has been quantified. Lateral beam deflection increases with initial proton energy and ranges between 1 mm and 10 mm for 80 MeV and 180 MeV. A systematic difference in deflections over the two experiments was found, which is suspected to be caused by a non-optimal magnet to laser alignment in the second experiment, which could be corrected for by a global rotation of all Experiment 2 deflected trajectories. Longitudinal retraction however remained within the measurement uncertainties, thus no effect can be reported.
2D dose distributions show the Bragg peak area of deflected beams to be symmetrical. The Bragg peak tilt effect observed by P.Moser [73] in a Monte-Carlo simulation of proton pencil beams in water, could not be verified. Moser found the Bragg peak to be tilted against die direction of deflection due to energy separation within the beam, for initial proton energies of 250 MeV and a uniform magnetic field of 3 T. Thus, the main reason that this effect could not be reproduced is a lower magnetic field (1 T) and lower proton beam energies within this investigation, as well as the use of PMMA as the phantom material, which further reduces proton range and therefore also lateral deflection.
No effect of the magnetic field was found on the depth-dose distribution of the pencil beams in comparison to performed reference measurements without magnetic field. Both the shape of the curve and range do not differ significantly. However, differences in percentage depth-dose curves (PDD) were found between the experiments which remain to be studied. A potential reason for uncertainties in PDD determination is presented by non-uniformity of the background on ETB3 films, suggesting a position dependent background subtraction for future experiments, to reduce noise on the PDD.
An unexpected 'hook' feature was detected on all reference trajectories at the end-of-range for both experiments performed and over all studied energies. For in-magnet trajectories the 'hook' is less pronounced, being visible for the lowest energies, it disappears with increasing energy. Two potential reasons for this 'hook' were introduced, while for a conclusion, further investigations are necessary.

7.2 Conclusion

Magnetometry results presented FEM calculations to underestimate the magnetic field by about 2%. The effect of this underestimation on beam deflection is considered negligible and thus it seems justified to use the calculated field map for Monte-Carlo simulations on potential future magnetic resonance integrated proton therapy systems (MRiPT). For the same purpose, a realistic in-magnet measurement setup for first MRiPT proof-of-principle experiments has been realized. Measurements of the proton beam trajectory proofed to be feasible and facilitate the development of commissioning for future MRiPT. The data obtained is instrumental for building and validating beam models for MRiPT. Thus, the first important step towards an MRiPT system was realized.

7.3 Outlook

The developed irradiation setup is not only capable of performing experiments as presented in this work but allows for further more complex investigations as well. First, a deeper analysis of the obtained results, concentrating on the variations detected on PDDs and the observed 'hook' would be desirable, to distinguish between setup-dependent effects and those introduced by the magnetic field. Moreover, an inhomogeneous phantom, offering air-gaps and inserts for bone or lung tissue surrogates, was already constructed and is ready to be used for experiments in a next step. Both the existing and future experimental data should then be compared to both predicted beam deflections (using the RAMDIM model) and MC simulations.
Furthermore, as this work proofed beam deflections in an hybrid MRiPT system to be measurable, the next step, turning from a permanent magnet to an MR imaging device would allow to tackle a whole new dimension of investigations.

Bibliography

[1] M Jermann. “Particle Therapy Statistics in 2014”, *International Journal of Particle Therapy* **2**, no. 1 (2015), pp. 50–54.

[2] O Jakel. “Medical physics aspects of particle therapy”, *Radiation Protection Dosimetry* **137**, no. 1-2 (2009), pp. 156–166.

[3] H Paganetti. “Range uncertainties in proton therapy and the role of Monte Carlo simulations”, *Physics in Medicine and Biology* **57**, no. 11 (2012), R99–R117.

[4] A-C Knopf and A Lomax. “In vivo proton range verification: a review”, *Physics in Medicine and Biology* **58**, no. 15 (2013), R131–R160.

[5] F H Gonzalez. “Nuclear methods for real-time range verification in proton therapy based on prompt gamma-ray imaging.” PhD thesis. TU Dresden, 2016.

[6] L A Dawson and M B Sharpe. “Image-guided radiotherapy: rationale, benefits, and limitations”, *The Lancet Oncology* **7**, no. 10 (2006), pp. 848–858.

[7] B W Raaymakers, A J E Raaijmakers, and J J W Lagendijk. “Feasibility of MRI guided proton therapy: magnetic field dose effects”, *Physics in Medicine and Biology* **53**, no. 20 (2008), pp. 5615–5622.

[8] J Hartman, C Kontaxis, et al. “Dosimetric feasibility of intensity modulated proton therapy in a transverse magnetic field of 1.5 T”, *Physics in Medicine and Biology* **60**, no. 15 (2015), pp. 5955–5969.

[9] B M Oborn, S Dowdell, et al. “Proton beam deflection in MRI fields: Implications for MRI-guided proton therapy”, *Medical Physics* **42**, no. 5 (2015), pp. 2113–2124.

[10] M Moteabbed, J Schuemann, and H Paganetti. “Dosimetric feasibility of real-time MRI-guided proton therapy”, *Medical Physics* **41**, no. 11 (2014).

[11] H Paganetti. *Proton Therapy Physics*. Ed. by Harald Paganetti. Taylor & Francis Inc, 2011. 704 pp.

[12] E Bezak, L Marcu, and B J Allen. *Biomedical Physics in Radiotherapy for Cancer*. Ed. by Barry Allen. Springer London Ltd, 2012. 430 pp.

[13] ICRU. “Report 16”, *Journal of the International Commission on Radiation Units and Measurements* **9**, no. 1 (1970).

[14] F Bloch. “Zur Bremsung rasch bewegter Teilchen beim Durchgang durch Materie”, *Annalen der Physik* **408**, no. 3 (1933), pp. 285–320.

[15] J Eulitz. “Commissioning of a Model of the IBA Universal Nozzle in Double Scattering Mode in the Monte-Carlo Tool TOPAS at the University Proton Therapy Dresden”. Master’s thesis. TU Dresden, 2017.

[16] T Bortfeld. “An analytical approximation of the Bragg curve for therapeutic proton beams”, *Medical Physics* **24**, no. 12 (1997), pp. 2024–2033.

[17] P de Vera, I Abril, and R Garcia-Molina. “Water equivalent properties of materials commonly used in proton dosimetry”, *Applied Radiation and Isotopes* **83** (2014), pp. 122–127.

[18] R Zhang and W D Newhauser. “Calculation of water equivalent thickness of materials of arbitrary density, elemental composition and thickness in proton beam irradiation”, *Physics in Medicine and Biology* **54**, no. 6 (2009), pp. 1383–1395.

[19] S S Hidalgo-Tobon. “Theory of gradient coil design methods for magnetic resonance imaging”, *Concepts in Magnetic Resonance Part A* **36A**, no. 4 (2010), pp. 223–242.

[20] Y Saad. *Iterative methods for sparse linear systems*. 2. ed. SIAM, Society for Industrial and Applied Mathematics, 2003.

[21] Y Kanai, T Abe, et al. “Further discussion on magnetic vector potential finite-element formulation for three-dimensional magnetostatic field analysis”, *IEEE Transactions on Magnetics* **26**, no. 2 (1990), pp. 411–414.

[22] L Li and J Luomi. “Three-Dimensional Magnetostatic Field Analysis Using Vector Variables”, *Electromagnetic Applications*. Ed. by Carlos A. Brebbia. Berlin, Heidelberg: Springer Berlin Heidelberg, 1989, pp. 25–46.

[23] Y Saad and M H Schultz. “GMRES: A Generalized Minimal Residual Algorithm for Solving Nonsymmetric Linear Systems”, *SIAM Journal on Scientific and Statistical Computing* **7**, no. 3 (1986), pp. 856–869.

[24] P Keller. *Technologies for Precision Magnetic Field Mapping*. Metrolab Instruments, Geneva Switzerland.

[25] A Jain. “Overview of Magnetic Measurement Techniques”, *US Particle Accelerator School on Superconducting Accelerator Magnets*. Brookhaven National Laboratory. Upton, New York 11973-5000, USA, 2003.

[26] Lake Shore Cryotronics, Inc. *User’s Manual Model 421 Gaussmeter*. 2004.

[27] D F Lewis. “A Processless Film For Recording Electron Beam Radiation”, *Hard Copy Output*. Ed. by Leo Beiser, Stephen L. Corsover, et al. SPIE International Society for Optics and Photonics, 1989.

[28] M Callens, W Crijns, et al. “A spectroscopic study of the chromatic properties of GafChromic^{TM}EBT3 films”, *Medical Physics* **43**, no. 3 (2016), pp. 1156–1166.

[29] G Gambarini, V Regazzoni, et al. “Measurements of 2D distributions of absorbed dose in protontherapy with Gafchromic EBT3 films”, *Applied Radiation and Isotopes* **104** (2015), pp. 192–196.

[30] Gafchromic. *Gafchromic EBT3 Scan Handling Guide*. Ashland, Inc. 2012.

[31] S Reinhardt, M Würl, et al. “Investigation of EBT2 and EBT3 films for proton dosimetry in the 4–20 MeV energy range”, *Radiation and Environmental Biophysics* **54**, no. 1 (2015), pp. 71–79.

[32] L Zhao and I J Das. “Gafchromic EBT film dosimetry in proton beams”, *Physics in Medicine and Biology* **55**, no. 10 (2010), N291–N301.

[33] D Kirby, S Green, et al. "LET dependence of GafChromic films and an ion chamber in low-energy proton dosimetry", *Physics in Medicine and Biology* **55**, no. 2 (2009), pp. 417–433.

[34] B Arjomandy, R Tailor, et al. "EBT2 film as a depth-dose measurement tool for radiotherapy beams over a wide range of energies and modalities", *Medical Physics* **39**, no. 2 (2012), pp. 912–921.

[35] L A Perles, D Mirkovic, et al. "LET dependence of the response of EBT2 films in proton dosimetry modeled as a bimolecular chemical reaction", *Physics in Medicine and Biology* **58**, no. 23 (2013), pp. 8477–8491.

[36] L Lin, T D Solberg, et al. "Pencil beam scanning dosimetry for large animal irradiation", *Journal of Radiation Research* **55**, no. 5 (2014), pp. 855–861.

[37] F-E Brack. "Charakterisierung von Ionen aus Laserinduziertem Plasma". Master's thesis. TU Dresden, 2016.

[38] Vacuumschmelze GmbH & Co. KG Hanau. *Selten - Erd - Dauermagnete*. 2014.

[39] B D Cullity and C D Graham. "Definitions and Units", *Introduction to Magnetic Materials*. John Wiley & Sons, Inc., 2008, pp. 1–21.

[40] Y Saad. "A Flexible Inner-Outer Preconditioned GMRES Algorithm", *SIAM Journal on Scientific Computing* **14**, no. 2 (1993), pp. 461–469.

[41] X W Ping, R S Chen, et al. "The SSOR-preconditioned inner outer flexible GMRES method for the FEM analysis of EM problems", *Microwave and Optical Technology Letters* **48**, no. 9 (2006), pp. 1708–1712.

[42] Omid Zarini. personal communication. 2016.

[43] Lake Shore Cryotronics, Inc. *Magnetic Field Technology - Hall Probes*. 2016.

[44] OWIS. *Product Information: Precision Linear Stages*. 2016.

[45] OWIS. *Product Information: Universal Position Control PS90*. 2016.

[46] Y Ito, K Yasuda, et al. "Radiation effects of 200 MeV proton beams on NdFeB magnets", *Nuclear Instruments and Methods in Physics Research Section B: Beam Interactions with Materials and Atoms* **209** (2003), pp. 362–366.

[47] F Hellberg and A Hedqvist. "Neutron radiation damage study and cost estimate of a hybrid magnet for the XFEL", Stockholms universitet. 2008.

[48] A Samin, M Kurth, and L R. Cao. "An analysis of radiation effects on NdFeB permanent magnets", *Nuclear Instruments and Methods in Physics Research Section B: Beam Interactions with Materials and Atoms* **342** (2015), pp. 200–205.

[49] Y Ito, K Yasuda, et al. "Magnetic flux loss in rare-earth magnets irradiated with 200 MeV protons", *Nuclear Instruments and Methods in Physics Research Section B: Beam Interactions with Materials and Atoms* **183**, no. 3–4 (2001), pp. 323–328.

[50] S Schellhammer, B Oborn, et al. "Experimental setup to measure magnetic field effects of proton dose distributions: simulation study", *ESTRO 36*. Conference Abstract. 2017.

[51] Å Carlsson, G Starck, et al. "Accurate and sensitive measurements of magnetic susceptibility using echo planar imaging", *Magnetic Resonance Imaging* **24**, no. 9 (2006), pp. 1179–1185.

[52] R Wolf and T Bortfeld. “An analytical solution to proton Bragg peak deflection in a magnetic field”, *Physics in Medicine and Biology* **57**, no. 17 (2012), N329–N337.

[53] S M Schellhammer and A L Hoffmann. “Prediction and compensation of magnetic beam deflection in MR-integrated proton therapy: a method optimized regarding accuracy, versatility and speed”, *Physics in Medicine and Biology* **62**, no. 4 (2017), p. 1548.

[54] H Paganetti. “Proton Beam Therapy”, *Proton Beam Therapy*. IOP Publishing, 2016.

[55] W M Preston and A M Koehler. “The effects of scattering on small proton beams.” unpublished manuscript. 1968.

[56] B Oborn, T Causer, et al. “High resolution silicon detector performance in proton beams at 1 T magnetic field: first experimental results”, *PTCOG 56*. Conference Abstract. 2017.

[57] D J O’Brien and G O Sawakuchi. “TH-CD-BRA-07: MRI-Linac Dosimetry: Parameters That Change in a Magnetic Field”, *Medical Physics* **43**, no. 6 (2016), pp. 3874–3874.

[58] G W Choi. “Measurement of the electron return effect using presage® dosimeters”. Master’s thesis. MD Anderson Cancer Center Graduate School of Biomedical Sciences, 2016.

[59] M. Mathis, G. Sawakuchi, et al. “Effects of a strong magnetic field on selected radiation dosimeters (TLD, OSLD, EBT3 film, PRESAGE)”, *CSM 2014*. Conference Abstract. 2014.

[60] M L Reyhan, T Chen, and M Zhang. “Characterization of the effect of MRI on Gafchromic film dosimetry”, *Journal of Applied Clinical Medical Physics* **16**, no. 6 (2015), pp. 325–332.

[61] ICRU. “Stopping powers and ranges for protons and alpha particles”, *ICRU Report 49* (1993).

[62] C-M Ma, S B Jiang, et al. “A quality assurance phantom for IMRT dose verification”, *Physics in Medicine and Biology* **48**, no. 5 (2003), pp. 561–572.

[63] S Reinhardt, M Hillbrand, et al. “Comparison of Gafchromic EBT2 and EBT3 films for clinical photon and proton beams”, *Medical Physics* **39**, no. 8 (2012), pp. 5257–5262.

[64] K Zeil, E Beyreuther, et al. “Cell irradiation setup and dosimetry for radiobiological studies at ELBE”, *Nuclear Instruments and Methods in Physics Research Section B: Beam Interactions with Materials and Atoms* **267**, no. 14 (2009), pp. 2403–2410.

[65] V Casanova B, M Pasquino, et al. “Dosimetric characterization and use of GAFCHROMIC EBT3 film for IMRT dose verification”, *Journal of Applied Clinical Medical Physics* **14**, no. 2 (2013), 158–171.

[66] L J van Battum, H Huizenga, et al. “How flatbed scanners upset accurate film dosimetry”, *Physics in Medicine and Biology* **61**, no. 2 (2015), pp. 625–649.

[67] D Lewis and M F Chan. “Correcting lateral response artifacts from flatbed scanners for radiochromic film dosimetry”, *Medical Physics* **42**, no. 1 (2014), pp. 416–429.

[68] A A Schoenfeld, D Poppinga, et al. “The artefacts of radiochromic film dosimetry with flatbed scanners and their causation by light scattering from radiation-induced polymers”, *Physics in Medicine and Biology* **59**, no. 13 (2014), pp. 3575–3597.

[69] M Mathot, S Sobczak, and M-T Hoornaert. “Gafchromic film dosimetry: Four years experience using FilmQA Pro software and Epson flatbed scanners”, *Physica Medica* **30**, no. 8 (2014), pp. 871–877.

[70] P V C Hough. *Method and means for recognizing complex patterns*. US Patent 3,069,654. 1962.

[71] M Nixon and A S Aguado. *Feature Extraction & Image Processing for Computer Vision*. Elsevier Science Publishing Co Inc, 2012. 632 pp.

[72] M J Berger, J S Coursey, et al. "ESTAR, PSTAR, and ASTAR: Computer Programs for Calculating Stopping-Power and Range Tables for Electrons, Protons, and Helium Ions (version 1.2.3)", *National Institute of Standards and Technology, Gaithersburg, MD* (2005).

[73] P Moser. "Effects on particle beams in the presence of a magnetic feld during radiation therapy". Master's thesis. Technische Universität Wien, 2015.

Appendix

A Cylindrical integration error

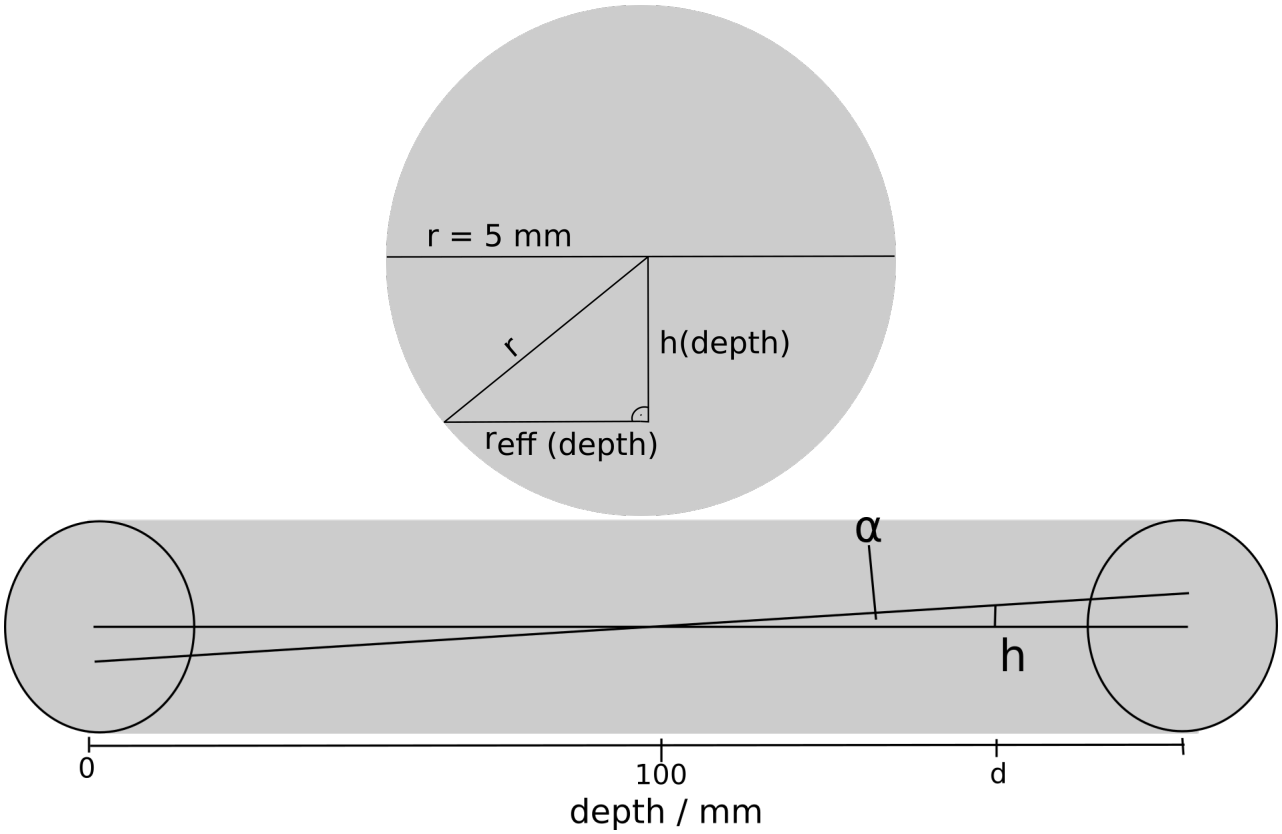

Figure A.1: Representation of the proton pencil beam, along the beam axis (top) and from side view (bottom). The effective radius r_{eff} used in the cylindrical integration depends on h(depth).

Due to the $\alpha = 1^{\circ}$ tilt angle of the film plane, integrating the PDD as described in chapter 5.4 is subject to an error as the method used is correct only for zero tilt angle. Here a correction strategy is presented to compensate for this effect. The beam is assumed to be of cylindrical shape with a diameter of 10 mm, matching the physical size of the collimator's aperture, neglecting beam spread due to scattering. Furthermore it is assumed that within the cylinder a constant dose is deposited. For each position d in depth, due to the tilted film plane, the effective radius r_{eff} of the beam is smaller than $r = 5\,\text{mm}$ except for the $d = 100\,\text{mm}$ depth point, which is the tilt axis of the film plane. The effective radius r_{eff} can be expressed by

$$r_{\text{eff}} = \sqrt{r^2 - h^2}$$

where $h = (d - 100\,\text{mm})\tan(\alpha)$, see Figure A.1. Using the assumption of constant dose within the cylinder the integrated depth dose can be expressed in terms of the area resulting from cylindrical

integration using r_{eff}:

$$A = 2\pi * r_{\text{eff}}^2.$$

Normalizing A to its maximum, a correction factor for the PDD is obtained. Figure A.2 presents A as a function of depth, in the upper plot, and a comparison of a raw and corrected PDD for a 140 MeV proton beam, in the lower plot.
The correction has its largest effect in the entrance area, while still being smaller than 5% change in PDD. The effect on the Bragg peak is negligible and the correction is therefore not applied to all PDDs within this study.

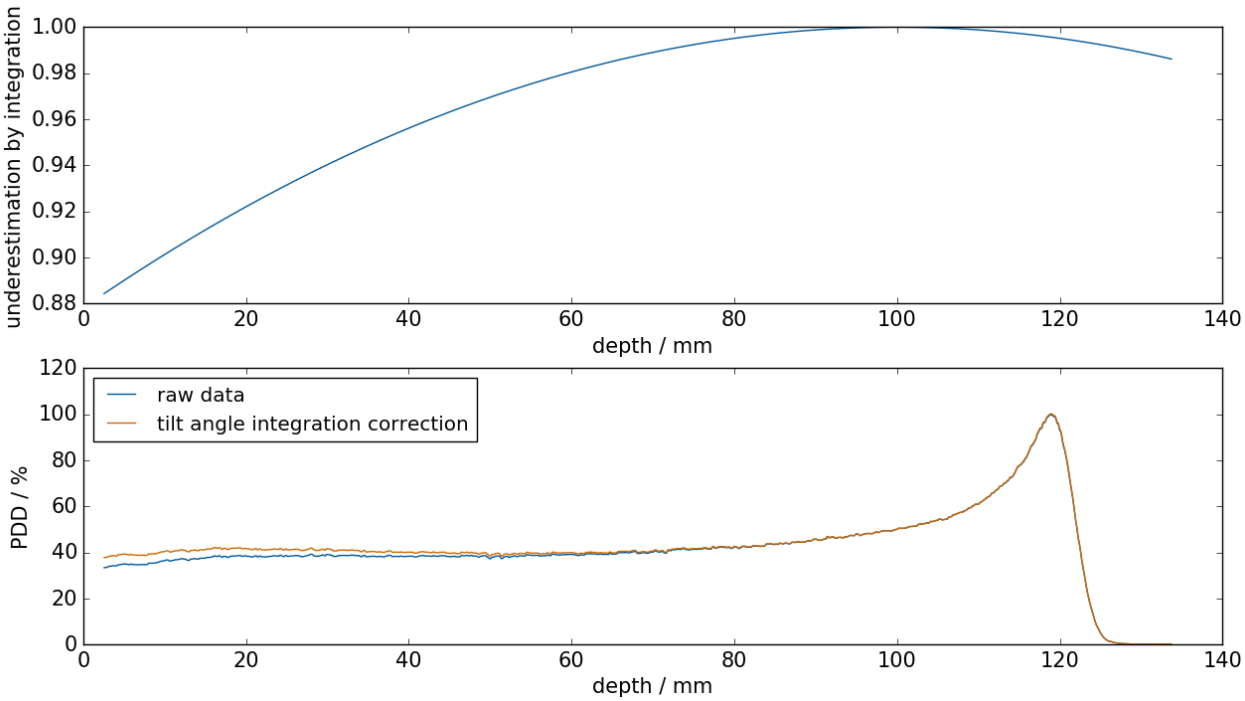

Figure A.2: The top plot presents the underestimation A as a function of depth. In the lower plot both raw PDD and corrected PDD for a 140 MeV proton beam are presented.

Acknowledgements

I would like to thank my referees Prof. Dr. Arno Staessner and Prof. Dr. Wolfgang Enghardt for their encouragement and insightful comments. My gratitude goes to my supervisor Dr. Aswin Hoffmann. He consistently allowed this thesis to be my own work, but steered me in the right direction whenever he thought I needed it. Furthermore I would like to thank Sonja Schellhammer and Dr. Armin Lühr, for their valuable and constructive suggestions during the planning and development of this research work. Your willingness to spend time so generously for all my ideas, however absurd they were, has been very much appreciated. Innumerable hours of lab work together with the two of you have made these very enjoyable.

Furthermore I would like to thank Prof. Dr. Ulrich Schramm and the two groups of Karl Zeil and Michael Bussmann, for the trust they put in us, providing the permanent magnet for all our experiments and fruitful initial discussions. Especially I would like to thank Florian Brack for providing the COMSOL model of the magnet and Omid Zarini for everything he has done to help me put up the magnetometry setup, helping with the LabVIEW routines and special tips regarding the Hall probe adjustment.

In addition, I want to thank Manfred Sobiella and Robert Schönert for building the magnet table and phantoms, helping with some crucial design questions and always shoving time for our project in the busy workshop schedule. I would like to thank Elke Beyreuther for introducing me to the craft of film dosimetry.

Besides all the above mentioned, it would like to thank Sonja Schellhammer and Dr. Aswin Hoffmann again, for the endurance to check this thesis for content, style, spelling and grammar, your help was very much needed. Furthermore I would like to thank Jan Eulitz and Lukas Dünger as well as all the SPACE office crew for a pleasant time and refreshing lunch breaks. Finally, I would like to thank my family and friends for their continuous support during my studies.

Declaration of Authorship

I hereby declare that I have written this Master's thesis independently and have listed all the used sources and means. I understand that attempted fraud will result in the failing grade "not sufficient" (5,0) and in case of recurrence in exclusion from completing of any further examinations and assessments.

Dresden, March 15, 2017